

REPORT DOCUMENTATION PAGE

AFRL-SR-BL-TR-98-

0270

1. AGENCY USE ONLY (Leave blank)		2. REPORT DATE February 1998	3. REPORT TYPE AND PERIOD Final Report (09/30/93-09/29/97)
4. TITLE AND SUBTITLE Nondestructive and Noncontact Evaluation of Corrosion and Fatigue by Laser Speckle Sensor (LSS) and Laser Moire			5. FUNDING NUMBERS 93-1-0618
6. AUTHOR(S) Fu-Pen Chiang Principal Investigator			
7. PERFORMING ORGANIZATION NAME(S) AND ADDRESS(ES) Dept. of Mechanical Engineering State University of New York at Stony Brook Stony Brook, NY 11794-2300			8. PERFORMING ORGANIZATION REPORT NUMBER 19980331 064
9. SPONSORING / MONITORING AGENCY NAME(S) AND ADDRESS(ES) AFOSR/NA Bolling AFB DC 20332-6448			
11. SUPPLEMENTARY NOTES The views, opinions and/or findings contained in this report are those of the author(s) and should not be construed as an official Department of the Army position, policy, or decision, unless so designated by other documentation.			
12a. DISTRIBUTION / AVAILABILITY STATEMENT Approved for public release; distribution unlimited.			12b. DISTRIBUTION CODE
13. ABSTRACT (Maximum 200 words) Five NDE techniques have been exploited for the detection of damage caused by corrosion and fatigue. They are (1) ESPI (Electronic Speckle Pattern Interferometry), (2) Digital Speckle Correlation, (3) TADS (Time Average Digital Specklegraphy), (4) Modified Projection Grating Technique and (5) Fractal Damage Sensor. Except the first one whose basic principle is known, the rest are all new techniques. While different techniques have different advantages and disadvantages, the most versatile is probably TADS and the Modified Projection Grating technique, whereby large areas (such as 5 M x 5 M or larger) can be evaluated simultaneously. We also investigated the corrosion and fatigue processes and their synergism. We find that corrosion in general reduces the fatigue life of a metallic alloy. However, if a modest amount of initial fatigue is followed by a modest amount of corrosion, the total fatigue life is actually enhanced. This is attributed to the blunting of microcrack tips by corrosion.			
14. SUBJECT TERMS			15. NUMBER OF PAGES 123
			16. PRICE CODE
17. SECURITY CLASSIFICATION OF REPORT UNCLASSIFIED	18. SECURITY CLASSIFICATION OF THIS PAGE UNCLASSIFIED	19. SECURITY CLASSIFICATION OF ABSTRACT UNCLASSIFIED	20. LIMITATION OF ABSTRACT UL

**Final Report
to
Air Force Office of Scientific Research**

**110 Duucan Avenue, Bolling AFB
Washington D.C. 20332-6448**

**on
Grant No. F496209310618
(09/30/93 to 09/29/97)**

**“Nondestructive and Noncontact Evaluation
of Corrosion and Fatigue by Laser Speckle
Sensor (LSS) and Laser Moiré”**

by

**Fu-Pen Chiang
Leading Professor and Chair
Dept. of Mechanical Engineering
State University of New York at Stony Brook
Stony Brook, NY 11794**

February 1998

Abstract

The report consists of two parts. Part I presents the various NDE (Nondestructive Evaluation) techniques that have been developed under this project and Part II deals with the study of corrosion and corrosion fatigue. When developing NDE techniques emphasis was on full field noncontact and remote sensing techniques whereby a large area of an aircraft structure can be evaluated simultaneously. Five methods have been proposed. The first method is ESPI (Electronic Speckle Pattern Interferometry). This is a very sensitive technique that can detect minute changes of shape, texture, etc. However its extreme sensitivity is also its drawback in that small environmental vibration will effect the result. It is very useful when a suspected region needs to be investigated in detail. A prototype of a portable system has been developed. The second technique is Digital Speckle correlation. This technique compares two speckle patterns. Correlation calculation is carried out to reveal the differences between the two. In an area of $1 \times 1 \text{ m}^2$ defects (such as pitting corrosion) as small as 0.3 mm (dia) by 0.1mm(depth) can be detected using this system placed at 2 m away. Higher resolution can be achieved when the viewing distance and area are varied. This technique has the potential of documenting and categorizing various corrosion types and severity of corrosion.

The third technique is the most versatile. It is called TADS (Time-Average Digital Specklegraphy). It is most suitable for detecting crevice corrosion. By applying a small vacuum or thermal loading the region that has crevice corrosion will deform differently with respect to the surrounding area. By illuminating the area with a laser beam and recording the speckle pattern several times at a certain distance in front of the surface, the resulting specklegram can be processed to reveal the hidden defect. A small change of the order of 10^{-4} gradient can be detected.

The fourth technique is a modified projection grating technique by taking advantage of the newly developed Texas Instruments digital projection system. This can be used to map the shape of an area several meters square. Minute changes as small as a fraction of a millimeter can be detected.

Last but not least is the newly developed Fractal Damage Sensor technique. We find damage of different kind results in different fractal dimensions. We have applied it to the detection of pitting and corrosion/fatigue damage.

The second part of the report is devoted to the study of corrosion fatigue. We find that the laser speckle sensor technique developed by P.I. under a different program can be effectively applied to monitoring fatigue damage as it progresses. We find that in general corrosion enhances the damage due to fatigue. However, we also find an unexpected result that when an aluminum alloy is first subjected to fatigue, a subsequently modest amount of corrosion actually increases the total fatigue life of the material. This is attributed to the fact that sharp crack fronts produced by the initial fatigue process has been blunt by the corrosion process. Thus, new cracks need to be initiated resulting in a prolonged fatigue life.

Table of Contents

PART I DEVELOPMENT OF NONDESTRUCTIVE EVALUATION TECHNIQUES.	1
1. INTRODUCTION.....	1
2. ELECTRONIC SPECKLE PATTERN INTERFEROMETRY (ESPI) FOR NDE OF CREVICE CORROSION.....	5
2.1 Introduction.....	5
2.2 Theoretical Background.....	7
2.3 NDE of crevice corrosion by ESPI.....	9
2.4 Discussion and Conclusions	10
3. DIGITAL SPECKLE CORRELATION.....	11
3.1 Introduction.....	11
3.2 Principle.....	12
3.3 Application to Detection of Corrosion.....	14
3.3.1 Pitting corrosion.....	14
3.2.2 Stress-corrosion cracking.....	15
3.2.3 Crevice corrosion	15
3.4 Conclusion.....	16
4. TIME-AVERAGE DIGITAL SPECKLEGRAPHY (TADS).....	16
4.1 Introduction.....	17
4.2 Theoretical Background.....	17
4.3 System Configuration.....	18
4.4 Experiments.....	19
4.5 Conclusion.....	20
5. PROJECTION GRATING TECHNIQUE.....	21
5.1 Introduction.....	21
5.2 Digital Phase-shifting for High Resolution Surface Contouring.....	23
5.3 Experimental Results:	25
6. FRACTAL DAMAGE SENSOR.....	26
6.1 Nondestructive Evaluation of Corrosion by Fractal Geometry.....	26
6.1.1 Introduction.....	26
6.1.2 Approaches	27
6.1.3 Experiments and Discussions	28
6.1.4 Conclusions.....	31
6.2 On Fractal Aspect of Corrosion/Fatigue	31
6.2.1 Introduction.....	31
6.2.3 Design of Experiment	33
6.2.4 Experimental results and discussion	34
6.2.5 Conclusions.....	37
REFERENCES	38
FIGURES.....	43

PART II	STUDIES OF CORROSION AND CORROSION FATIGUE.....	71
1. INTRODUCTION.....		71
2. SURFACE ROUGHNESS AND ITS MEASUREMENT TECHNIQUES.....		72
2.1 INTRODUCTION		72
2.2 CONTACT MEASUREMENT TECHNIQUE		73
2.3 LASER SPECKLE SENSOR.....		73
2.3.1 <i>The Relationship between Surface Variation and Speckle Pattern</i>		73
2.3.2 <i>Evaluation of Spectrum</i>		74
3. INFLUENCE OF CORROSION ON THE FATIGUE PROCESS OF ALUMINUM ALLOY		76
3.1 INTRODUCTION		76
3.2 SPECIMEN AND EXPERIMENT		77
3.3 RESULTS AND DISCUSSION.....		78
3.4 CONCLUSIONS		80
4. EFFECT OF THE INITIAL FATIGUE CYCLES ON THE BEHAVIOR OF CORROSION-FATIGUE		81
4.1 INTRODUCTION		81
4.2 EXPERIMENTAL PROCEDURE.....		81
4.3 DAMAGE CAUSED BY FATIGUE AND CORROSION.....		82
4.4 FATIGUE LIFE SPAN AS A RESULT		84
4.5 CONCLUSIONS		85
5. SYNERGISM BETWEEN CORROSION AND FATIGUE.....		86
6. THE INFLUENCE OF ACETONE DEGREASING ON THE CORROSION BEHAVIOR OF AL 2024-T3.....		87
6.1 INTRODUCTION		87
6.2 EXPERIMENTAL METHOD.....		88
6.3 RESULTS AND DISCUSSION.....		90
6.3.1 <i>XPS Results</i>		90
6.3.2 <i>Inductively Coupled Plasma Atomic Emission Spectroscopy</i>		90
6.4 MECHANISM		92
6.4.1 <i>Formation of Copper chloride</i>		92
6.4.2 <i>Timed exposure of the alloy to 0.5M NaCl</i>		93
6.5 CONCLUSIONS		93
REFERENCES.....		94
FIGURES.....		97
APPENDICES		120
APPENDIX 1 LIST OF PUBLICATIONS RESULTING FROM THIS PROJECT		121
APPENDIX 2 LIST OF PERSONNEL PARTICIPATED IN THE PROJECT		123

Part I Development of Nondestructive Evaluation Techniques

1. Introduction

Economic considerations have driven the industry toward the retention of older aircraft. These aging aircraft exhibit various kinds of damage due to fatigue and corrosion. FAA has formed a blue ribbon panel on aging aircraft and an ARPA blue ribbon panel is looking into aging aircraft issues as well. Concurrently, the US Air Force has the requirement to maintain many of the current aircraft into the next century. For example C/KC-135 aircraft are expected to operate until 2040, B-52s until 2030, and E-3s for an indefinite period (as per statement by Don Nieser of OC/ALC/LACRA at the Joint AFOSR-AFMC/EN Aging Aircraft Conference, Atlanta, Georgia, 27-28/4/93). Two of the major factors that would affect the structural integrity of an aging aircraft are corrosion and fatigue, which tend to act synergistically.

Corrosion/fatigue often leads to catastrophic structure failures. The 1973 failure of an F-4 resulted in the establishment of the fail-safe criteria for USAF aircraft, the Boeing 707 accident in 1977 resulted in the damaging tolerance assessment for commercial aircraft and the current FAA aging aircraft research and development program arises from the Aloha Airlines Boeing 737 failure in 1988.

The US Air Force (USAF) established the criteria for damage tolerance assessments (DTAs) in the seventies. In the future, however, the results of these DTAs may not be adequate to protect aircraft safety[Lincoln, 1997]. This could happen when airplanes operate beyond their design service life and open the possibility of introducing new critical areas. Corrosion could affect the inspection intervals through the acceleration of crack growth. Thus, it is paramount that there are effective means to detect and evaluate the early stages of damage due to corrosion and fatigue. Existing techniques such as eddy current can only detect certain

types of damages due to corrosion or fatigue and are only effective when significant damages have occurred. As a result they cannot satisfy the need for overall evaluation and early stage monitoring of damages. Therefore, new approaches are needed to tackle this important problem.

In the following we shall summarize our work on NDE of corrosion/fatigue sponsored under this contract. In an effort to devise a novel and simple method of nondestructive evaluation technique to detect corrosion caused damage, especially hidden ones such as crevice corrosion, we have tested several optical methods including projection grating method (with phase-stepping), ESPI (Electronic Speckle Pattern Interferometry) [Jin and Chiang, 1997a], digital speckle correlation techniques (DSC)[Jin and Chiang, 1997b]. We have finally settled on one novel technique which we believe is superior than any other existing optical NDE methods for hidden damages (e.g., crevice corrosion & composite delamination). This technique is called TADS (Time-averaged Digital Specklegraphy)[Jin and Chiang, 1996a]. Also, we have found a modified Projection Grating Method with Digital Fringe Projector developed by us [Huang et al., 1997] and fractal geometry promising tools for the surface corrosion evaluation. A Fractal Damage Sensor (FDS) based on fractal has been developed and applied to the NDE of corrosion/fatigue [Jin and Chiang, 1996b, 1997c].

There are several common types of corrosion often seen on aircraft [Hagemaiier et al., 1985]: surface corrosion; pitting; intergranular corrosion; exfoliation; crevice corrosion; stress-corrosion cracking; microbial corrosion and filiform. As a hidden defect, crevice corrosion always attracts more attention than the others. Crevice corrosion occurs when two different metals are in direct contact and exposed to an electrolyte such as water or water containing dissolved salts. It is not necessary for both surfaces to be metallic. Crevice corrosion also occurs when one of the surfaces is nonmetallic, a gasket for example. It is dangerous to aircraft structures because it results in the thinning of structure plates and it is undetectable until significant damage has been done.

Electronic Speckle Pattern Interferometry (ESPI) was employed to reveal the existence of crevice corrosion which is usually undetectable from outside by visual inspection. The ESPI is

configured to measure out-of plane displacement. Both thermal loading and vacuum loading are used. The anomaly of fringe patterns reveals the existence of crevice corrosion hidden between two metallic plates. Not only the location of defects, but also the approximate size can be estimated.

In DSC when the speckle pattern (laser or white light) of a corroded specimen surface is compared to that of a virgin surface, the difference can be quickly and clearly revealed by the cross-correlation coefficient of the two speckle patterns. This technique can reveal pitting corrosion areas as small as 5 mm (0.2 in.) \times 5 mm (0.2 in.) wherein exists a cluster of pits of 0.3 mm (0.012 in.) in diameter and 0.1 mm (0.004 in.) in depth. An artificial stress-corrosion crack was used to demonstrate the validation of this method for detection of stress-corrosion cracking. For detection of crevice corrosion, laser illumination must be applied. Digital speckle correlation takes the advantage of laser speckle properties. The speckle decorrelation caused by out-of-plane displacement in the region with a crevice corrosion under the specimen's surface is bigger than that without defects. This difference is calculated by a digital correlation algorithm, which reveals the crevice corrosion.

ESPI possesses high sensitivity in detecting crevice corrosion and composite delamination but is not robust enough for field tests; on the contrary, DSC is robust but has less sensitivity. An ideal technique must come with the advantages of both ESPI and DSC. Such a technique is called Time-average Digital Specklegraphy (TADS), a novel optical system integrates high resolution CCD camera, fiber optics and image processing developed for NDT of crevice corrosion. By recording the laser speckles contained in a plane in front of the surface as a time-average the resulting specklegram will yield a variety of information concerning the displacement of the surface. The motion of the speckle is sensitive to the first order derivative of the out-of-plane displacement of the surface. Upon applying thermal or vacuum loading to the specimen, any local slope changes on the surface will cause drastic varying of the corresponding speckles. Such kind of anomalies usually indicate the weakened regions of the structure. Several crevice corrosion samples were used to demonstrate the validity of the technique. It was shown the resolution of this system is as high as 10^{-4} gradient in slope changes. Meanwhile, its low requirement on environmental conditions makes it a promising NDT tool for field tests.

Surface corrosion and some crevice corrosion results in the modification of surface topographical texture. This can be revealed by the Projection Grating technique. When a grating is projected onto the surface of a specimen, its three-dimensional shape is revealed by the distortion of the (originally straight) grating lines. Classical moire method requires that a undisturbed reference grating be superimposed onto the "deformed" grating to yield moire fringes which are nothing but the elevation contours of the object. Modern CCD camera and computer technique have eliminated this need, for the distortion can be easily calculated and related to the shape or shape change.

A revolutionary digital light processing technology recently developed by Texas Instrument has made the potential of the fully-automated projection grating method more promising than ever. We take advantage of the device called Digital Light Processing (DLP) and turn it into a programmable Digital Fringe Projector. The preliminary investigation shows that it can be used to contour objects ranging from small to very large. The surface height information can be quantitatively and accurately obtained because of potential self-calibration capability. Phase-shifting measurement can be implemented electronically without using additional devices. The fringe pattern and density can be changed and controlled by computer for optimized results.

Fractal geometry is finding its application in Nondestructive Evaluation (NDE) of corrosion by characterizing the corrosion surface with fractal dimensions. It was found that corrosion surfaces can be well described by multifractals. Two algorithms were used to obtain the fractal dimension of a corroded aluminum alloy surface, one being Box-counting another being Coherent Light Scattering. Fractal dimensions were related with the damage caused by corrosion and fatigue.

Corrosion and fatigue are two major factors that contribute to the aging of aircraft. These two factors act synergistically in various ways. Recent studies have revealed the fractal nature of corrosion and fatigue. Since corrosion and fatigue results in texture changes of a metal surface, they change its fractal dimension as well. The degree of damage by corrosion/fatigue manifests itself in the severity of surface texture change. Thus, one can quantify corrosion /fatigue with fractal dimension.

A new technique named Fractal Damage Sensor (FDS) was applied to the on-line monitoring of corrosion/fatigue process during the experiments. A series of processes were designed to simulate the different situations that aircraft may experience in service. In one case, Al2024-T3 alloy specimens were first subject to a various amount of fatigue loading and then immersed in a corrosive solution for a fixed amount of time. Subsequently the specimens were fatigued to failure; In another case the specimens were subject to corrosion and fatigue simultaneously. In both cases fractal dimensions were calculated at different stages of corrosion/fatigue. The preliminary results show that certain relationship exists between the fractal dimension and the corrosion/ fatigue process. The study provides a new approach to quantify corrosion/fatigue with the aim of establishing a theory to assess damage and estimate the remaining life of a damaged structure.

2. Electronic Speckle Pattern Interferometry (ESPI) for NDE of crevice corrosion

2.1 Introduction

Considerable efforts have been devoted to the development of optical techniques for NDE. Doyle et al. (1993) proposed a laser-based profilometer to locate and measure corrosion fatigue cracking in boiler tubes. A similar approach using laser light scattering is found in the work of Buerkle et al.'s (1992). The system uses laser light scattering to count defect features rather than image them. It has been used successfully in a laboratory environment on both polished and unpolished metal samples containing scratches, fatigue cracks and holes. A recent study introduced the concept of fractal geometry into the evaluation of surface corrosion [Jin and Chiang, 1996b]. It is found that corrosion surfaces can be well described by multifractals. Fractal dimensions are related to the damage caused by corrosion and fatigue [Jin and Chiang, 1997c].

Shearography has also shown promise for inspection of aircraft structures [Newman, 1991]. It has been used to inspect the strain field in riveted lap joints under tensile loads as well as for the NDE of composite and honeycomb repairs. An enhanced visual technique for surface inspection called D sight [Komorowski et al., 1991; Hageniers, 1987; Reynolds and Hageniers, 1988] has been applied to detecting cold-worked holes, corrosion, and fatigue cracks associated with a high stress-intensity factor. It is a simple process that provides enhancement to small amplitude undulations of flat and moderately curved surfaces. It is claimed to be adaptable to the detection of any phenomenon leading to a change in surface topography greater than 10 μm . Another technique proposed to evaluate impact and fabrication damage in composite is a digital image correlation scheme [Russell et al., 1989]. This method records a digital image of a paint-speckled surface before and after the body is deformed. The two images are compared to yield both the displacements and strains needed to map one image into another. Anomalies present in the strain field are used to locate regions of suspected damage and also quantify the severity of damage. A relatively new method, thermal wave imaging was reported to do NDT on aging aircraft [Favro et al., 1993]. This technique uses pulses of heat to interrogate subsurface features in solid objects. These pulses propagate into the object as thermal waves, are reflected from subsurface defects. These thermal wave echoes can be detected by infrared video cameras and the patterns of echoes are used to image subsurface corrosion and disbonds in aircraft skins. This method is fast, noncontact, and sensitive to the defects so close to the surface that they are essentially unobservable by ultrasonics. The only shortcoming of the thermal wave imaging is that the surfaces under test have to be heat absorptive. Some aircraft with raw metal surfaces have low heat absorption coefficient, therefore are not suitable for the thermal wave imaging.

The reported work focuses on finding an effective and economic way to detect and evaluate corrosion damage using a technique that is sensitive, nondestructive, noncontacting and remote-sensing. ESPI is usually used to measure full field surface deformations of a diffuse object. Lately, it is increasingly being looked on as a potentially valuable tool for nondestructive evaluation of structures [Gulker et al., 1990; Paoletti et al., 1990]. The attractiveness of this technique is its noncontact nature, the relatively simple inspection procedure and the ability to show real time results. Being an interferometric method, ESPI possesses sensitivity as high as

holographic interferometry. But it has much more tolerance to environmental noise than holography. In this paper it is shown to reveal crevice corrosion rapidly with high resolution.

2.2 Theoretical Background

The major feature of ESPI is that it displays real time correlation fringes on a monitor. Since it utilizes the speckle pattern, ESPI possesses an intrinsic resistance to environmental noise. Speckle has been introduced to the field of metrology for decades. When an optically rough surface (i.e. its RMS roughness is much larger than the wavelength of the illuminating light) is illuminated by a coherent light such as laser, the reflected wavelets from each point of the surface mutually interfere to form a very complicated pattern called speckle [Chiang, 1989]. A typical speckle pattern is shown in Fig.2.1. The principle of ESPI has been discussed extensively in other publications [Jones and Wykes, 1990; Creath and Slettemoen, 1985]. And there are recent works addressing the issue of improving the system's tolerance to poor environmental conditions [Lokberg and Malmo, 1988; Spooren, 1992; Pouet and Krishnaswamy, 1993]. A schematic representation of ESPI is shown in Fig.2.2. The laser light is split into two branches to form an interferometer. Each of the two beams is expanded by a beam expander. One of the expanded beams is used to illuminate the object under test while the other is used as a reference by passing it through a ground glass diffuser. The coherent light scattered from the test object is made to interfere with the reference beam, and the resulting interferometric speckle pattern is imaged by a CCD camera for digital image processing. Before the deformation of the object the speckle pattern intensity recorded on the CCD camera is given by

$$I_R = I_1 + I_2 + 2\sqrt{I_1 I_2} \cos(\Phi_1 - \Phi_2) \quad (1)$$

where all the variables are functions of x and y as registered on the CCD board. I_1 is the intensity of the object beam, I_2 is the intensity of the reference beam, and Φ_1 , Φ_2 are the phases of the respective waves.

After the object is deformed, the intensity becomes

$$I_D = I_1 + I_2 + 2\sqrt{I_1 I_2} \cos(\Phi_1 - \Phi_2 + \Phi) \quad (2)$$

where $\Phi(x,y)$ carries the information of the object deformation: $\Phi = (2\pi/\lambda) \Delta \mathbf{n} \cdot \mathbf{d}$, where $\Delta \mathbf{n} = \mathbf{n}_1 - \mathbf{n}_2$, with \mathbf{n}_1 and \mathbf{n}_2 being the direction vectors of the each illuminating beams; and $\mathbf{d} = (dx, dy, dz)$ is the displacement vector. I_R is stored in the computer image processing system and subsequently subtracted from I_D . The rectified result is a speckled fringe pattern given by:

$$I_R - I_D = 2\sqrt{I_1 I_2} |\cos(\Phi_1 - \Phi_2) - \cos(\Phi_1 - \Phi_2 + \Phi)| = 4\sqrt{I_1 I_2} |\sin[(\Phi_1 - \Phi_2) - \Phi/2] \sin(\Phi/2)| \quad (3)$$

The first sine term of Eq. 3 represents the random speckle noise, whereas the second sine term is the fringe pattern. The intensity of the fringe pattern varies between maximum and minimum I_{\max} & I_{\min} given by

$$I_{\max} = \sqrt{I_1 I_2} \quad \Phi = (2n+1)\pi, \quad n = 0, 1, 2, \dots \quad (4)$$

$$I_{\min} = 0 \quad \Phi = 2n\pi, \quad n = 0, 1, 2, \dots$$

By using high-pass filtering the low frequency noise together with variations in mean speckle intensity is removed and the quality of the fringe is enhanced. The real-time fringes displayed on the monitor are similar in appearance to conventional holographic fringes, but with speckle noise

and lower contrast. ESPI with such a working mode is referred to as subtractive ESPI. Another algorithm is the additive ESPI. But it is characterized by poor fringe quality and seldom used.

2.3 NDE of crevice corrosion by ESPI

Experiments were performed using the out-of-plane deformation sensitive setup as shown in Fig.2.2. Two specimens were used in the investigation. Both were two-layered aluminum structures with a thick back plate (3.175mm) and a thin front plate (1.143mm) bonded together by bolts. In between there existed a crevice corrosion cavity wherein the interior central portion of the front plate had been thinned. Fig.2.3 shows the schematic of specimen-I.

The coherent light source was a 40 mw He-Ne laser with a wavelength of 633 μm . Two types of loading methods were applied. One is thermal loading and the other vacuum loading. A hot air gun (a commercial hair dryer with 500/1000 W output) was used to blow the top surface of the specimen assembly for one to three seconds (at 500 W output). Deformation field varied due to the difference in heat transfer at various parts of the structure. Two specimens were tested. The specimen without crevice corrosion yielded relatively uniform speckle fringes (as shown in Fig.2.4-a), while the deformation of the specimen with crevice cavity gave a quite different fringe appearance (Fig. 2.4-b). The fringes concentrated to a region where the crevice corrosion hid beneath. This anomaly was what revealed the existence of crevice corrosion. The visual effect was much more vivid when the live fringes were displayed on the monitor in real time fashion. The region with the hidden defect manifests itself as a source (when heating up) or sink (when cooling down) with fringes continuously generating or vanishing there.

In order to generate a vacuum loading a specifically designed vacuum cell was used. It was in the form of a suction cup with a Plexiglas window of 11 cm in diameter. The vacuum ranged from 0-30 in-Hg and was precisely adjusted by a minute vacuum regulator. The vacuum cell applied an uniform negative pressure to the specimen's surface. The resulting ESPI speckle

fringes were circular in general except where there was a crevice corrosion (Fig. 2.5). Fig. 2.6 is a three dimensional plot of the out-of-plane deformation data. The advantage of vacuum loading is that since the load is well defined the deformation fields can be quantitatively calculated. As a result the size and the depth of the cavity can be determined with precision if a mechanics model is built based on plate theory and numerical simulations. The future work will be focussing on this aspect.

2.4 Discussion and Conclusions

In this chapter we have demonstrated the potential of using ESPI for NDE of crevice corrosion. Test results clearly indicate that the damage regions manifest themselves as anomalies in the displacement data. ESPI is characterized by high sensitivity(each fringe represents a one-half of a wavelength out-of-plane displacement, roughly $0.3 \mu\text{m}$) and fringe vacillation. Anomalies caused by relatively small crevice corrosion can be detected. While ESPI as it is configured has a much less stringent vibration isolation requirement than that of holographic (or other classical) interferometry technique, it nevertheless needs relatively vibration free environment.

The sensitivity of the ESPI for NDE of crevice corrosion can be estimated based on a simplified model. When the thermal loading is applied to a corrosion sample, the nonuniform displacement field is due to the uneven heat transfer and thinning of the front plate at the corroded region. Even without taking into account the contribution of the heat transfer, the difference in displacement field caused by the thinning alone is evaluated as follows. Suppose the stiffness of the plate is EI , the thickness is t , where E is Young's modulus and I is area moment of inertia of the cross section. Since $I \propto t^3$, the deflation of the plate is $Y \propto 1/I = 1/t^3$. If the change of thickness is as mild as 2%, the deflation of the plate Y will change about 8%. Such a difference is significant enough to be picked up by ESPI. So it is safe to say the sensitivity of ESPI to the crevice corrosion is better than 2% (thickness change). Meanwhile, the spatial

resolution largely depends on the optical imaging system. Usually a couple of centimeter is about the size of distinguishable crevice corrosion.

In order to make the methods described above suitable for the aircraft maintenance hangar environment, a prototype of the system is being devised. It consists of an optical head and a control unit. The optical head including a CCD, optical imaging components and an illuminator can sit on a tripod and is ready to move around. The laser light is delivered to the illuminator via a single mode optical fiber (cable). The control unit composed of a computer and a laser can be carried on a cart. Such a configuration can satisfy the requirement of the major applications of ESPI. In case of a more unstable environment, in order to get clear ESPI fringes the optical head will be put in a vacuum cell and the vacuum cell sucks to the fuselage. While applying the vacuum loading the vacuum cell together with the optical head stick to the fuselage so that there will not be any relative motion.

3. Digital Speckle Correlation

3.1 Introduction

Digital Speckle Correlation (DSC) is a noncontact NDE method that is used here as remote sensor to detect pitting, stress-corrosion cracks and crevice corrosion. A simulated pitting and a real pitting created on Al7075 by 0.1 M HCL solution were used to demonstrate the resolution of this technique. A fully developed fatigue crack was used as the stress-corrosion sample. The crevice corrosion specimen was made up with two layers of aluminum plate with a crevice corrosion cavity in between. This method has been shown to have a large varied sensitivity range. The fact that this technique is fast, noncontact and nondestructive satisfies the requirement for in-situ inspection.

Digital Speckle Correlation method is based on the concept of image correlation. It is well known that one of the most sensitive ways to compare the feature of different objects is through spatial correlation. Digital correlation algorithm has been applied to experimental stress analysis^[8,9]. In general, the method of digital image correlation requires two digital images of the specimen under test: one image before the specimen is deformed and a second image after deformation. The two images are compared by a computer image identification algorithm.

Our effort seeks to develop a new nondestructive evaluation method based on digital image correlation. For detection of pitting and cracking, two speckle patterns are needed, one from the specimen under test, another from a reference surface. Defects are revealed by the cross correlation coefficient. There is no special requirement for environmental condition. The procedure of detection of crevice corrosion is similar to that for deformation measurement. Two speckle patterns, one before deformation another after deformation are captured and registered by an image acquisition system. The pronounced decorrelation of speckle patterns reveals the existence of crevice corrosion.

3.2 Principle

Laser speckle is the result of multiple interference from an optically rough surface and its structure depends on the texture of surface under illumination. In speckle interferometry the amplitudes in the recording plane before and after recording contain terms of the form [16]:

$$U_1 = U_s \exp(i\phi_s) \quad (5)$$

$$U_2 = U'_s \exp[i(\phi'_s + \Delta\phi)] \quad (6)$$

And it has been assumed that $U_s = U'_s$ and $\phi_s = \phi'_s$. The correlation coefficient of U_1 and U_2 is defined as:

$$\Gamma(U_1 U_2) = (\langle U_1 U_2 \rangle - \langle U_1 \rangle \langle U_2 \rangle) / (\langle U_1^2 \rangle \langle U_2^2 \rangle) \quad (7)$$

Since it can be assumed that $\langle U_1 \rangle = \langle U_2 \rangle = 0$ and $\langle U_1^2 \rangle = \langle U_2^2 \rangle = \langle I_s \rangle$, where $\langle I_s \rangle$ is the mean intensity of the speckle pattern, (7) becomes

$$\Gamma(U_1 U_2) = \langle U_1 U_2 \rangle / (\langle U_1^2 \rangle \langle U_2^2 \rangle) \quad (8)$$

A minute change of the surface texture between exposures leads to the decorrelation of the speckle structure [Osintsev et al., 1992, 1988]. There are three major ways that can change the speckle pattern [Streckenrider and Wagner, 1995]. The first is a displacement gradient in the speckle field that may result from a small elastic strain or rotation on the surface. The second is the rigid body translation of the speckle field. Finally, the speckle pattern can undergo a morphology change where the initial and the final state are totally decorrelated. The surface may have undergone one of several transformations in order to produce this speckle morphology change: excessive surface displacement (either in-plane, out-of-plane or rotational), excessive elastic strain, excessive surface tilt, or plastic deformation. Also the optical imaging system can cause the decorrelation of speckle field, Lens aberration or defocus for example [Li and Chiang, 1986]. In this investigation we take advantage of this effect to detect pitting, stress-corrosion cracking and crevice corrosion through a digital correlation calculation algorithm.

The specimen is illuminated by a white light or laser beam so that either white light or laser speckles are generated on its surface. The speckle pattern of the object is imaged by a CCD camera and its intensity is digitized into an array of 512×480 pixels with 8 bit gray level by a frame grabber and then stored in a frame buffer or diskette. A PC is used to process the data (Fig. 3.1).

Two registered speckle patterns are first segmented into a number of very small subimages (either 16×16 pixels or 8×8 pixels). Each subimage pair is analyzed to yield the local correlation coefficient which reveals the difference of features of the subimage pair. The correlation coefficient for digital images is given by :

$$C(x = 0, y = 0) = \frac{\sum_i \sum_j f_{x+i, y+j} g_{i,j}}{\sqrt{\sum_i \sum_j f_{x+i, y+j}^2 \sum_i \sum_j g_{i,j}^2}} \quad (9)$$

where f and g are the intensity functions of the subimage pair. Instead of direct calculation of (10), the computational efficiency is enhanced by doing FFT twice:

$$C(f, g) = \mathcal{F}^{-1}\{F \times G^*\} \quad (10)$$

Where $F = \mathcal{F}\{f\}$, $G = \mathcal{F}\{g\}$, where \mathcal{F} is the Fourier transform operator, G^* is the complex conjugate of G .

3.3 Application to Detection of Corrosion

3.3.1 Pitting corrosion

Pitting corrosion always results in cavities or holes in the metal with little or no general dissolution of the rest of the surface. Pitting first appears as a white, powdery deposit, but when the surface is buffed it reveals tiny pits or holes. In moderate to severe cases, the pits appear as well defined hills and valleys when viewed through a magnifying lens. Fig. 3.2. shows a sample of Al7075 having sustained pitting corrosion. Fig. 3.3. depicts the distribution of cross correlation of the corroded surface with an uncorroded surface. Each peak in the 3D plot corresponds to a pit at that position. An artificial pitting sample as shown in Fig. 3.4 was used to demonstrate the resolution of the technique. Fig. 3.5 shows the 3D view of correlation coefficient distribution. This method can reveal pitting corrosion areas as small as 5 mm (0.2 in.) \times 5 mm (0.2 in.) wherein exists a cluster of pits of 0.3 mm (0.012 in.) (diameter) \times 0.1 mm (0.004 in.) (depth) in size. This resolution is achievable when the viewing area is 1 m (39.4 in.) \times 1 m (39.4 in) using a CCD camera situated at 2 m (78.8 in.) away. Much higher resolution can be obtained

when the viewing distance is shorter. The size of the corroded area can easily be calculated using an appropriate algorithm.

3.2.2 Stress-corrosion cracking

Stress-corrosion cracking is caused by simultaneous effects of both stress and corrosion. It manifests itself as a crack in the metal but is not necessarily accompanied by obvious corrosion. Fig. 3.6. shows a fatigue crack generated to simulate a stress-corrosion crack. The length of the crack is about 20 mm (0.8 in). In Fig. 3.7 the location of the crack is clearly shown by the drastic change of correlation coefficient data.

3.2.3 Crevice corrosion

Experiments were carried out on specimen-I with vacuum loading. The specimen was a two-layered aluminum structure with a thick back plate (3.175 mm (0.125 in.)) and a thin front plate (1.143 mm (0.045 in.)) bonded together using bolts. In between there existed a crevice corrosion, whereby the interior central portion of the front plate had been thinned. Fig. 3.8 gives the inside view of the crevice corrosion.

A laser beam was used to illuminate the specimen. The experimental setup was similar to that of Electronic Speckle Pattern Interferometry (ESPI) but without the reference beam. The laser speckle patterns generated from the diffuse specimen surface before and after loading were recorded by a CCD camera and stored into a frame grabber board in a personal computer. If the front plate should deform, the deformation in the crevice corrosion area should be larger than that in other areas due to the thinning of the plate thickness in this area. The excess out-of-plane deformation resulted in decorrelation of the speckle patterns which in term resulted in reduced coefficient of correlation in the affected area.

The coherent light source for illumination was a 40 mw He-Ne laser with a wavelength of 633 μm . Two types of loading were tried. One was a thermal loading and the other is vacuum loading. A hot air gun (a commercial hair dryer with 500/1000 W output) was used to blow the top surface of the specimen assembly for several seconds and the temperature change was monitored by a thermal meter. The temperature rose from 70 F (21 C) to 156 F (69 C). The resultant correlation data was plotted in 3D fashion shown in Fig. 3.9. The advantage of heat loading is: noncontact, rapid and easy to apply.

In order to generate a vacuum loading, a specifically designed vacuum cell was used. It was in the form of a suction cup with a 114 mm (4.5 in.) (diameter) Plexiglas window. The vacuum ranged from 0-30 in-Hg and was precisely adjusted by a minute vacuum regulator. The vacuum cell applied an uniform negative pressure to the specimen's surface. If the speckle decorrelation of a certain region shows any abnormal concentration, it reveals the crevice corrosion. The advantage of vacuum loading is that the testing procedure and specifications can be quantitatively determined based on the experiments.

3.4 Conclusion

In this chapter Digital Speckle Correlation method finds its new application on detection of corrosion. Three cases: pitting , stress-corrosion cracking and crevice corrosion were discussed. This technique has been proved to be fast, automatic, noncontact and nondestructive. There is great potential for it to become an important utility on NDE of corrosion of aging structures.

4. Time-Average Digital Specklegraphy(TADS)

4.1 Introduction

Our effort was devoted to the development of a simple and robust device to detect corrosion caused damage, especially hidden ones such as crevice corrosion. A novel optical system integrates high resolution CCD camera, fiber optics and image processing was developed. When an optically rough surface is illuminated by a coherence laser beam, a random interferometric pattern called speckle is generated in front of the surface covered by the reflected wavelets. If the surface is under motion these speckles also move accordingly. By recording the speckles contained in a plane in front of the surface appropriately the resulting specklegram will yield a variety of information concerning the displacement of the surface. And it is this information that we exploit results in the development of the technique reported in this paper.

4.2 Theoretical Background

The theory of the laser speckle formation and its application can be found in the works of Dainty & Ennos (1984), Jones & Wykes (1983), and Chiang & Li (1985,1986), for example. When an optically rough surface is illuminated by a coherent light, the intensity of the scattered light is found to vary randomly with position-- this is referred to as objective speckles; When an image of the surface is formed through a lens, the image shows a similar random intensity variation, that is called subjective speckle. It is the latter that we exploit in developing the TADS techniques.

The size of a subjective speckle σ can be taken as the separation between the first two minima of the Bessel function on the image plane:

$$\sigma = 2.4\lambda F \quad (1)$$

where λ is the wavelength, F is the $f/$ number of the imaging lens. When the object moves, these tiny "spots" move accordingly. If the surface as a whole displaces in the line of sight, there will be no change in the imaged speckle (Dainty, 1984). When a surface with a weakened area (a hidden defect, for example) is under either thermal or vacuum loading, it will generate an out-of-plane deformation which

in turn results in the local surface tilting. And an excessive out-of-plane deformation will cause decorrelation of the speckle pattern resulting in a blurred image. In the region with no flexing of the surface, the speckle pattern remains sharp. Fig. 4.1 shows schematically the formation of a laser speckle and its movement as the result of surface tilt.

Let $w(x, y)$ be the out-of-plane displacement of the surface of the specimen, the slope, Φ , of a point

$$\Phi(x, y) = \mathbf{s} \frac{\partial}{\partial \mathbf{s}} w(x, y) \quad (2)$$

(x, y) may be written as

in which s is the distance along an arbitrary direction, denoted by the unit vector \mathbf{s} . The surface tilts the spatial speckles in much the same way as a mirror tilting light rays. Thus, if the camera is at a sufficient distance away from the specimen and focused at a plane away from the specimen surface one can approximate the local slope as [Chiang and Juang, 1976]:

$$\Phi(x, y) = \frac{d(x, y)}{2D} \quad (3)$$

where d is the tilt induced displacement of the speckles in the focused plane and D the distance between the object and the focused plane. When the recording is done in a time-average fashion, the moving speckle will streak at the image plane rendering them distinct from the rest of the speckles. And it is these streaked speckles that serve as the defect indicator.

4.3 System Configuration

A prototype of the system has been built. The schematic set up is shown in Fig. 4.2. It consists of a high resolution CCD camera, a workstation computer for image acquisition and processing, a laser and a set of single mode fiber optics components for illumination. The CCD camera has a resolution of 2029×2048 pixels with pixel size being 9×9 microns. The fiber optic devices for light outlet are mounted on the CCD camera, rendering it a portable illuminating/imaging device. The entire optical head can be mounted on a tripod. The compact design makes the system ideal for field test.

4.4 Experiments

A series of tests were carried on different specimens. The schematic of a crevice corrosion specimen is shown in Fig. 4.3. It was a double-layer aluminum alloy structure with a thick back plate (3.175 mm) and a thin front plate (1.143 mm) bonded together by bolts simulating an aircraft fuselage structure. In between the plates there exists a crevice corrosion cavity wherein the interior central portion of the front plate has been thinned. The cavity is unnoticeable from the outside. When disassembled, it has the appearance as shown in Fig. 4.4(a).

The coherent light source was a 40 mw He-Ne laser with a wavelength of $633\text{ }\mu\text{m}$. The CCD camera was set to focus on a plane a small distance away from the surface. A hot air gun (a commercial hair dryer of 500/100w output) was used to blow the top surface of the specimen assembly for a couple of seconds (at 500 w output). Right after the thermal loading was stopped, a series of images (3 -- 8 frames) were recorded and results averaged. The intensity-averaged images contain a variety of information concerning the displacement of the surface and can be immediately displayed on a monitor. A typical time-average speckle pattern is shown in Fig. 4.4(b). The anomalies on the speckle patterns reveal the existence of weakened region. Further image processing can substantially enhance the visibility of the defect. Fig. 4.4(c) shows the same speckle pattern processed by a contrast-based segmentation algorithm, and Fig. 4.4(d) by a binarization algorithm. It is seen that both algorithms work well in distinguishing the weakened region of the specimen.

In an effort to evaluate the resolution of TADS three specimens with different size of crevice corrosion were created. Fig. 4.5 illustrates the geometry of the crevice corrosion together with their corresponding speckle patterns. It can be seen that both the size and location of the crevice corrosion are clearly revealed by the patterns. Since in an aging aircraft a crevice corrosion tends to find its way near the fasteners, a sample was made to simulate this case as shown in Fig. 4.6. The area of crevice corrosion was almost twice the size of the fastener itself. The presence of the fastener adds extra constraints on the front plate. As a result the out-of-plane displacement was rather small. However, TADS had sufficient resolution to reveal its existence and the result is depicted in Fig. 4.6(b).

4.5 Conclusion

We have developed a new optical NDE technique called TADS (Time-Average Digital Specklegraphy) and have demonstrated that it can be successfully applied to the detection of crevice corrosion in metal structures and delamination in composites. The system is simple and

robust and is easily portable. It has a resolution of detecting slope change of the order of 10^{-4} gradient.

TADS can be used to detect other defects as well. An example is the delamination defect in structures. Fig. 4.7 shows the application of TADS to a honeycomb plate with metal face plates commonly used in aircraft construction. It had a narrow blade shaped delamination on one side of the plate. The TADS technique was employed to detect its existence and the result is as shown. Fig. 4.7(b) depicts the resulting speckle pattern after a small thermal loading without image enhancement and Fig. 4.7(c) with image enhancement. It is seen that the delamination area is distinctly revealed.

5. Projection Grating Technique

5.1 Introduction

Surface corrosion and some crevice corrosion results in the modification of surface topographical texture. This can be revealed by 3-D contouring technique. Many optical 3-D contouring methods have been developed, which can generally be categorized into two groups: scanning and non-scanning imaging techniques [Bieman 1988]. The scanning techniques are represented by point triangulation [Blais and Rioux 1986], laser radar [Svetkoff, et al. 1984], and structured line methods, of which point triangulation and structured line methods are based on the triangulation principle and the laser radar is based on the measurement of the travel time or phase of either a pulsed or modulated laser. All these techniques require either one-dimensional or two-dimensional scanning of the laser to cover the entire surface of the object, which generally makes the systems more sophisticated and the measurement more time-consuming.

Typical non-scanning techniques include stereo vision and moiré interferometry. Stereo vision obtains three-dimensional information of an object by viewing a scene from two different perspectives and then locating common features in both images [Hobrough and Hoborough

1983]. The processing of the images is computationally intensive, which makes the technique not suitable for high-speed 3-D contouring.

Moiré interferometry is probably the most commonly used technique for 3-D surface contouring. Compared to other techniques, it has the primary advantage of fast measurement speed due to the fact that it does not require scanning to cover the whole object surface and the image processing for extracting 3-D contour information is relatively simple. Moiré contouring techniques can be classified as either shadow or projection moiré. Shadow moiré uses the same grating for both illumination and observation, while projection moiré uses separated gratings. Another surface contouring technique is fringe projection which is not really moiré but is typically considered as a moiré technique. The fringe projection method uses only one grating and measures surface height by triangulation.

Shadow moiré has the advantage of easiness in obtaining quantitative contour information from the moiré pattern because the grating is flat and its period known. However, with shadow moiré, the contouring of large objects can be difficult because a grating with approximately the same size as the object has to be used, which is difficult to make, and has limited mobility.

The major advantages of projection moiré and fringe projection are their ability to contour large objects, and the ease with which phase measuring techniques can be implemented to increase the measurement resolution. Their primary limitation is the tedium associated with obtaining quantitative height information. This limitation arises because it is necessary to calibrate both the projection geometry and the magnification factor. Also when phase shifting technique is used, the physical scan of one of the gratings is necessary which requires additional actuators and control.

When a grating is projected onto the surface of a specimen, its three-dimensional shape is revealed by the distortion of the (originally straight) grating lines. Classical moire method requires that a undisturbed reference grating be superimposed onto the "deformed" grating to

yield moire fringes which are nothing but the elevation contours of the object. Modern CCD camera and computer technique have eliminated this need, for the distortion can be easily calculated and related to the shape or shape change.

A revolutionary digital light processing technology recently developed by Texas Instrument has made the potential of the fully-automated projection grating method more promising than ever. We take the advantage of the device of Digital Light Processing (DLP) and turn it into a programmable Digital Fringe Projector. The preliminary investigation shows that it can be used to contour objects ranging from small to very large. The surface height information can be quantitatively and accurately obtained because of potential self-calibration capability. Phase-shifting measurement can be implemented electronically without using additional devices. The fringe pattern and density can be changed and controlled by computer for optimized results.

5.2 Digital Phase-shifting for High Resolution Surface Contouring

The resolution of moiré interferometry or moiré contouring depends on fringe density on the object; higher fringe density generally means higher resolution. However, there is a limit to the fringe density that can be applied because overly dense fringes may not be resolvable by the camera. To solve the dilemma, phase-shifting technique has been developed and widely used in optical metrology applications [Halioua and Liu 1989; Moore 1979; Srinivasan et al. 1984, 1985; Boehnlein and Harding 1986; Kujawinska 1987; Toyooka and Iwaasa 1986]. It can dramatically increase measurement resolution without the need of using high density fringes. In general, it works by shifting one of the gratings to create a series of phase-shifted fringe images, based on which image processing techniques are used to extract the phase of each pixel of the image. Many algorithms can be applied to obtain the phase, which include the three-step [Gallagher and Herriott 1972; Creath 1988], four-step, least-squares [Bruning et al. 1974; Greivenkamp 1984], Carre [Carre 1966], averaging 3+3 [Schwider et al. 1983; Wyant and Prettyjohns 1987], Hariharan [Hariharan et al. 1987], and 2+1 [Angel and Wizinowich 1988; Wizinowich 1989,

1990] algorithms. For example, in the three-step algorithm, three phase-shifted images are taken with phase shifting of 120° in between any two adjacent images. The brightness of each pixel in the three images can be represented as follows:

$$I_1(x, y) = I_0(x, y)[1 + \gamma(x, y)\cos(\phi + 0^\circ)] \quad (1)$$

$$I_2(x, y) = I_0(x, y)[1 + \gamma(x, y)\cos(\phi + 120^\circ)] \quad (2)$$

$$I_3(x, y) = I_0(x, y)[1 + \gamma(x, y)\cos(\phi + 240^\circ)] \quad (3)$$

where $I_0(x, y)$ is the average brightness of the pixel, $\gamma(x, y)$ is the fringe visibility, and ϕ is the phase to be determined. Solve the above three equations simultaneously for ϕ yields the following solution:

$$\phi = \arctan\left(\frac{I_3 - I_2}{2I_1 - I_2 - I_3}\right). \quad (4)$$

With ϕ for each pixel determined, a saw-tooth-like phase wrapped image can be generated from which the height information for each pixel of the image can be extracted based on the standard phase unwrapping process. More than three phase-shifted images can be taken, which generally translate into higher accuracy. The trade-off is longer processing time both in image capture and processing.

Phase-shifted images are generally obtained by mechanically shifting one of the gratings. The shortcomings are that the system becomes more complicated because of the introduction of moving parts into the system and the phase-shifting may not be accurate due to mechanical errors. The Phase Shifting And Logical Moiré (PSALM) was proposed to eliminate some of the problems with the traditional phase-shifting technique [Asundi 1991], which uses only one grating with the other grating generated by software in the computer. The phase-shifted moiré fringes are obtained through logic calculations on the image of the object and the software created grating. Since no moving parts are necessary, this technique greatly simplifies the contouring system. The problem of this technique is that the contouring result is subject to

possible errors due to surface reflectivity changes and existing surface marks. Other attempts to simplify the contouring system used Liquid Crystal Display (LCD) panel as the projection system [Asundi 1991; Arai 1991]. With the creation of the fringe pattern and the phase-shifting of it done digitally by the software, the system is flexible and simple. However, because of the low image brightness and contrast of LCD panels [Sansoni 1991], the quality of the fringe image reflected from the object is poor which causes errors in extracting surface contour information. For this reason, any meaningful contouring can only be done for small objects.

To address the problem associated with the traditional phase-shifting techniques, we plan to take full advantage of the new digital projection technology to implement the concept of digital phase-shifting technique for improved contouring resolution. With the capabilities of high projected fringe brightness, contrast, and spatial accuracy and digital accuracy of phase shifting, higher level of contouring accuracy can be achieved as compared to the traditional techniques. Also, because of the fact that no moving parts are involved in the phase-shifting mechanism, higher system precision and reliability are expected. Since a 2k x 2k pixel CCD camera was used in this experiment, a total of 4 million data points were obtained simultaneously. We also measured a 600 x 600 mm panel with the same technique. As a result, we found that a resolution of better than 0.1 mm in surface height measurement is attainable.

5.3 Experimental Results:

In our experiment, we used a projection system with 800 x 600 resolution for fringe projection and a high resolution black-and-white CCD camera with 2k x 2k pixels for image capture. The projected fringes were sinusoidal in their brightness with 256 gray levels. For each object, three phase-shifted images with 120 degrees of phase difference between any two consecutive images were obtained. From these three images, the phase-wrapped image was calculated based on the three-step phase wrapping algorithm³. Then a phase unwrapping algorithm was applied to reconstruct the 3-D surface contour of the object. A total of 4 million data points were generated for each object surface contoured. Figure 5.1 shows the contouring

results of a dummy face. (a) - (c) are the three phase-shifted images. (d) is the mask generated by taking the average of the three phase-shifted images and then binarizing it at the gray level of 20. This mask is generated to remove the noise in the background of the phase-wrapped image. (e) shows the phase-wrapped image with the background noise removed. (f) shows the reconstructed 3-D contour of the dummy face. In another experiment, a sheet metal panel (approximately 600 x 600 mm) was contoured using the same technique. From the results, we found that a resolution of better than 0.1 mm in surface height measurement was achievable. An artificial pitting corrosion sample was inspected by Projection Grating method (Fig. 5.2). The smallest pits are 1 mm in diameter.

6. Fractal Damage Sensor

6.1 Nondestructive Evaluation of Corrosion by Fractal Geometry

6.1.1 Introduction

Fractal geometry is finding many applications in science and engineering. Essentially it characterizes a complex geometrical pattern by a parameter called the fractal dimension. It has been found that surfaces of fracture, wear, erosion, corrosion etc. are fractals [Russ, 1992]. It has also been shown [Pentland 1983, Peleg et al., 1984] that the brightness pattern in images of fractal surfaces is also mathematically a fractal and that this also holds for SEM images. Dai et al. (1990) even utilized fractal dimension to estimate surface roughness and plastic strain of a metallic specimen. Costa et al. (1991) described the structure of the corrosion pit profiles in terms of fractal dimensions. Many works were reported on the application of fractal geometry to fracture mechanics and earth science [Wong, 1988; Zhang and Lung, 1989; Long et al. 1991;

Poon et al. 1992; Nagahama, 1994]. People may find it helpful that D. E. Roach et al. (1993) presented and compared standard and new methods used to estimate the fractal dimension of random(natural) fractals.

Since corrosion results in texture changes of a metal surface it changes its fractal dimension as well. The degree of corrosion damage manifests itself in the severity of surface texture change (*i.e.* damage). Thus, one can use the fractal dimension not only to characterize the type of corrosion but also the severity of corrosion. A typical result is shown in Figures 6.1.1 and 6.1.2 where the fractal dimension of a pitting corrosion is illustrated. It is noted that the connection of the data points has a constant slope, thus indicating that the corrosion pattern has a constant fractal dimension. When the type and severity of corrosion change, this fractal dimension will also change accordingly. Thus, the fractal dimension presents itself as natural way to categorize corrosion damage.

A Fractal is defined as " a set for which the Hausdorff dimension strictly exceeds the topological dimension" and is less than the embedding dimension [Mandelbrot, 1982]. Consider measuring a stretch of curve, a coastline for example. By using a ruler of length e , we can get the length of coastline L . By using a smaller ruler, we get a bigger result, and so forth. As the ruler(scale) becomes smaller and smaller, the measured result becomes larger and larger. L is the function of e and satisfies:

$$L(e) = e^{1-D} \quad (1)$$

where D is called fractal dimension. Because $L(e) = N \times e$, so: $N \times e^D = 1$. Then

$$D = \log(N) / \log(1/e) \quad (2)$$

6.1.2 Approaches

Two algorithms were used to calculate the fractal dimension of corrosion surfaces. One was the Box-counting Method, and another was the Coherent Light Scattering Method.

Box-counting Method

For the analysis of the pitting corrosion patterns the images were digitized , low-pass filtered and thresholded to produce a white and black representation of pitted and unpitted regions, respectively (Fig. 6.1.1). The filtering was used to eliminate "noise" due to features below the resolution at a particular magnification.

The first method to characterize the pattern is to search for an experimental fractal size distribution. The procedure starts by covering the digitized picture with an imaginary net of square boxes of size r . The number of boxes, $N(r)$, containing any part of the objects to be analyzed is counted. For a fractal structure it is expected that $N(r) \propto r^{-D}$. A log-log plot of $N(r)$ versus r should thus produce a straight line with slope $-D$.

Fig. 6.1.2 shows the result for the pitting region in the digitized image of Fig.1. By treating these data with regression formulas, we obtained a straight line: $y=A+Bx$. For our case the fractal dimension $D=-B=1.859$.

Coherent Light Scattering Method

Suppose we illuminate a fractal object whose surface dimension is D_s by coherent light of wave length λ . The light will be diffracted by the object and the incident energy dispersed in all directions. The diffraction is due to a transfer of momentum characterized by a length $\eta(\theta) = (4\pi/\lambda)\sin(\theta/2)$. It can be shown that the direction θ follows the law $I(\eta) \propto \eta^{-\nu}$ [11]. This law holds for diffraction in what is called the "Porod" region, characterized by $1/\eta$ being less than the characteristic length of the diffraction object. The exponent ν depends on the structure of the object. If the fractal structure is defined by the surface, the light intensity

$$I(\eta) \sim \eta^{-\nu}, \text{ and } \nu=2d-D_s \quad (3)$$

where d is the dimension of the space in which the object is embedded (2 for a plane, 3 for ordinary space)[Mehaute, 1991].

6.1.3 Experiments and Discussions

In order to reveal the relationship between the corrosion pattern and the fractal dimension, three pieces of sample made of aluminum alloy Al7075 were investigated. The samples were 10mm × 10mm in size and were polished. One was retained as a reference surface and the others were corroded by polarization process. A pitting corrosion was produced in 1M NaCl solution and an intergranular corrosion surface was generated in 0.1M HCl. Their microstructures along with the polished surface were revealed by SEM, shown in Fig. 6.1.3.

In our experiments, the corrosion surface is illuminated by a narrow laser beam. The diffraction light intensity, which is the power spectrum, is recorded by a CCD camera with a resolution of 512*512 pixels. Each pixel has 256 gray levels. The image was imported by a frame grabber to the computer.

Fig. 6.1.4 shows the power spectrum of (a) polished surface without corrosion, (b) intergranular corrosion surface corroded by 0.1M HCl solution, and (c) pitting corrosion surface corroded by 1M NaCl solution. The intensity $I(\eta)$ vs. η is plotted in Fig. 6.1.5. The data can be linked with two distinct lines rather than a single line depending on the spatial frequency. That means the phenomenon can be approximated by multifractal. The data on the left side of the plot corresponds to a fractal description of raw structures of low spatial frequency whereas the data on the right side represent textures of high spatial frequency. In the later discussion these two parts of data will be called low part and high part respectively. However, for the polished surface (Fig. 6.1.5-a) the slope of the data on the left side of the plot (low part) is -0.222. If Eq. (3) is to be used to calculate the fractal dimension of the low part, a fractal dimension of 3.778, which is obviously not correct, would be obtained. It is due to the fact that, as stated before, Eq. (3) holds only when $1/\eta$ is less than the characteristic length of the diffraction object. For the polished sample, the low part data most likely do not satisfy this condition. Therefore, Eq. (3) cannot be used in this case. In fact, since the low part data only represent a rather flat surface, only the high part data will be taken into account in the further discussion. The fractal dimension D of the polished surface is 1.179. Fig. 6.1.5-b & c show the high part data from the pitting and the intergranular corrosion surface respectively. The data seem to fit quite well lines with constant slopes, from which the fractal dimensions of the surfaces under various conditions were obtained. The fractal dimension D of the intergranular corrosion sample is 2.241, and of the pitting corrosion sample is 2.038.

The second experiment was carried out to determine the fractal dimension of specimens experiencing different process. The specimens were made of aluminum alloy Al2024. Fig. 6.1.6-a shows the data from virgin material surface without any treatment and its fractal dimension is 1.334. The specimen corroded in 3.5wt% NaCl solution for 12 hours has a fractal dimension of 1.562 (Fig. 6.1.6-b). Fig. 6.1.6-c is the specimen sustained corrosion for 100 hrs and its fractal dimension is 2.057. It can be seen with the corrosion time going longer, the fractal dimensions go up. Fig. 6-d is the result from the specimen that was first corroded for 12 hrs and then fatigue for 241k cycles. Its fractal dimension is 1.790.

6.1.4 Conclusions

Fractal geometry is a useful concept to characterize materials undergoing various process. Different process results in different fractal patterns. A corrosion surface can be described by multifractals. It was also observed that fatigue may have a similar effect on the fractal dimension. The fractal dimension can be used to quantify the damage caused by corrosion and fatigue and also may be used to categorize different types of corrosion. While corrosion accumulates, the fractal dimension of the surface increases. Fractal geometry has great potential to be an effective tool in NDE of aircraft corrosion. The fractal dimension can quantify the extent of corrosion. The proposed approach for quantitative NDE of corrosion is a noncontact, rapid and automatic test.

6.2 On Fractal Aspect of Corrosion/Fatigue

6.2.1 Introduction

Economic considerations have driven the industry toward the retention of older aircrafts (Flournoy and Seher, 1995). These aging aircrafts exhibit various kinds of damage due to fatigue and corrosion (Chubb et al., 1995). Very often fatigue cracks initiate on the surfaces roughened by corrosion (Kawahara et al., 1988 and Doyle et al., 1990). Crack initiation is a function of many surface features such as the presence of pits or crevices, fatigue induced voids, intrusions and extrusions (Lin and Ito, 1969, Lin et al., 1990), etc.

Since corrosion/fatigue results in texture changes of a metal surface it changes its fractal dimension as well. The degree of corrosion/fatigue damage manifests itself in the severity of surface texture change (*i.e.* damage). Thus, one can use the fractal dimension not only to characterize the type of damage but also the severity.

In an effort to quantify the corrosion and fatigue damage, fractal geometry has been applied [Jin & Chiang, 1996b]. It was found that corrosion and fatigue surfaces can be well described by multifractals. An optical technique, namely Fractal Damage Sensor (FDS), was developed to evaluate the fractal dimensions and the validity was tested. In this chapter we present some new results of our continuous investigation on the aging process of aluminum alloy using FDS. One group of specimens is subject to fatigue and then to corrosion and then to fatigue again. Another group is subject simultaneous corrosion and fatigue. This study helps us in better understanding the mechanism of damage in materials sustained corrosion and fatigue.

6.2.2 Fractal Damage Sensor (FDS)

Fractal Damage Sensor is based on the theory of coherent light scattering from fractal objects [Mehaute, 1991]. Suppose we illuminate a fractal object whose surface dimension is D_s by coherent light of wave length λ . The light will be diffracted by the object and the incident energy dispersed in all directions. The diffraction is due to a transfer of momentum characterized by a length $\eta(\theta) = (4\pi/\lambda)\sin(\theta/2)$. It can be shown that the direction θ follows the law $I(\eta) \propto \eta^{-v}$ [11]. This law holds for diffraction in the region characterized by $1/\eta$ being less than the characteristic length of the diffraction object. The exponent v depends on the structure of the object. If the fractal structure is defined by the surface, the light intensity

$$I(\eta) \sim \eta^{-v}, \text{ and } v = 2d - D_s$$

where d is the dimension of the space in which the object is embedded (2 for a plane, 3 for ordinary space).

A schematic of FDS is shown in Fig.6.2.1, where a laser beam (a He-Ne laser with $\lambda = 0.628 \mu\text{m}$ and beam size of 2 mm) illuminates the specimen surface. The reflected beam is scattered in various directions according to the characteristics of the surface. The scattering wavelets, being coherent, mutually interfere to form a speckle halo whose size and shape can be directly related to the surface roughness. The speckle halo

on U-V plane is captured on a ground glass, and a CCD camera (with 512×480 pixels array in 8-bit gray level) records the speckle halo and digitizes its spatial intensity variation. As the laser scans the specimen surface the speckle halos at various points is recorded. Nine points in the area of interest of the specimens were scanned during the experiment. Then these series of images were imported into a computer and calculated to yield the fractal dimensions of the corresponding stages.

6.2.3 Design of Experiment

The specimens were made of Al 2024-T3 with a yield strength $\sigma_y=320$ MPa. The size and geometry of the specimens are as shown in Fig.2, they were subject to tension-tension cyclic loading of sinusoidal form with a frequency of 9 Hz, a load ratio R equal to 0.2, and a maximum stress of 200 MPa. The geometry was so designed that we could be reasonably certain that a fatigue crack would initiate near the center region of the specimen, where the technique of FDS was used to monitor the aging process. The size of the specimen was constrained by the need to examine the specimen for surface analysis.

It is well known that both fatigue and corrosion cause damage to metallic materials that manifest themselves macroscopically in the form of surface microstructure change. Those damage could be fatigue induced slip lines, intrusion, extrusion, grain rotation and/or corrosion pits, intergranular corrosion etc. This surface microstructure change as a function of the fatigue cycle and/or the corrosion period would be a useful indicator to monitor the degree of aging of materials. Traditionally surface texture is characterized by roughness and the corresponding parameters are measured by a mechanical profilometer. However, it is difficult to use a profilometer in real time or without dismounting the specimen. Furthermore, this very process often damages the material surface resulting in scratches which may become sites of fatigue crack initiation. Fractal dimension provide an overall measure of the texture/microstructure of material thus, directly correlates to the damage caused by mechanical or chemical

processes. Fractal Damage Sensor makes possible the on-line noncontact monitoring of the damage development.

In this investigation, the specimens were first fatigued (under tension-tension cyclic load of 9 Hz and load ratio $R=0.2$, maximum stress of 200 MPa) to various degrees of damage and then immersed in a corrosive solution of 3.5 wt% NaCl and 10 v% H_2O_2 for a period of 48 hours. They were then further fatigued to failure. The speckle halo response from nine points of the specimen surface (see Fig.1) were monitored. To ascertain the role corrosion plays in the total fatigue life of the aluminum alloy, we varied the initial fatigue cycle but kept the corrosion period fixed in this investigation.

Besides the sequential fatigue, corrosion and then fatigue test, the wet test is also conducted. This is to see the simultaneous effect between corrosion and fatigue. The experimental set-up is shown in Fig. 6.2.3. Same material and same specimen configuration are used. A corrosive solution of 3.5 wt% NaCl is pumped into the solution cell. The solution flow rate is 80 ml/min. 9 specimens were tested under the maximum stress of 200MPa with stress ratio $R=0.2$. The average fatigue life is 929,000 which is about only $\frac{1}{4}$ that of fatigue life tested in air.

6.2.4 Experimental results and discussion

The general mechanism of metal fatigue involves three stages, surfaces of which have different microstructure. The stage 1 is resulting in intrusion and extrusion and the creation of micro-voids and micro-cracks. Visible cracks are then formed along shear planes. Stage 2 involves the propagation and coalescence of micro-cracks across one or several grains until one dominant crack takes over and propagates perpendicular to the imposed principal tensile stress. In stage 3 failure occurs when the remaining ligament breaks by plastic failure or brittle fracture.

Fig. 6.2.4(a) shows a typical fatigue damaged (at stage 1) Al 2024-T3 specimen after

150,000 cycles of loading. It is seen that the micro-damage manifested in the form of micro-cracks, voids, extrusion and intrusion. From a global viewpoint the damage appears to be randomly oriented resulting in macroscopically isotropic texture change.

Aluminum alloys are susceptible to various forms of localized corrosion depending on the microstructure, heat treatment, grain orientation, applied stress, etc. Pitting attack is most prevalent when exposed to solutions containing chloride ions, which is believed to be caused by the localized breakdown of the passive film. Pits sometimes are isolated but often cluster together to form a roughened surface. They act as stress raisers facilitating the initiation of fatigue cracks. Fig.6.2.4(b) shows a surface damaged with pitting.

As noted before both fatigue and corrosion damage result in surface roughness change macroscopically. To demonstrate such a change, the surface roughness of three specimens were measured by a mechanical profilometer, and the results were plotted as shown in Fig. 6.2.5. The specimens were subjected to fatigue loading at 50,000, 150,000 and 200,000 cycles respectively, and then immersed in corrosive solution for 48 hours and then fatigued again to failure. It is seen that the surface roughness gradually changes as the loading cycle increases. The sudden jumps in roughness were due to the corrosive process. However, roughness measurement using mechanical profilometer creates its own damage. Instead, we used the FDS technique to monitor the specimen damage in-situ during fatigue, except when the specimen was dismounted for immersion into corrosive solution.

Fig. 6.2.6 shows the fractal dimension changes as the specimen sustains the fatigue-corrosion-fatigue sequence. Fig. 6.2.6(a) depicts the variation of fractal dimension at the point 7, 8 and 9 of the specimen which was subject to fatigue of 100k then corrosion 48 hrs and fatigue to failure. A fatigue crack initiated at the edge near point No. 9 when loading cycle reached 310K. In fractal dimension---load cycle (D--N) plot point No. 9 has a sudden increase at the corresponding cycle number, indicating the sensitivity of fractal dimension to material damage. In another test the initial fatigue

was 50K cycles and then also was corroded for 48 hrs (Fig. 6.2.6(b)). Again, Crack took place near point No. 9, which has the biggest jump and highest magnitude among all in the D--N plot. It is noticed that right after 48 hrs corrosion the fractal dimensions D of different points are quite close. Then they diverse with the increase of the fatigue cycle. This homogenization effect of the fatigue--corrosion process actually benefits the total fatigue life. The result of simultaneous corrosion--fatigue is shown in Fig.6.2.7. The crack occurred between point No. 7 and 6, closer to No.7. After a certain stage (60K cycles) most the curves rise rapidly and monotonously.

In general, as the damage accumulates the fractal dimension of the surface increases. At the time a fatigue crack initiates the fractal dimension in that region has a jump, i.e. a high gradient with respect to fatigue cycle, and the area near the crack tip has the highest magnitude of fractal dimension. It is observed that fatigue and corrosion have different effects on surface microstructure. In the dry environment the curves of fractal dimension vs. number of cycle oscillate, except at the end of fatigue life there is an over-shoot. At the early stage the fractal dimension tends to drop a little bit. The explanation may lie in the fact that surface undergoes a certain texture changes -- microstructure reorganization from the manufactured state. Another phenomenon worth mentioning is that after some initial fatigue cycles (150k) then the specimen sustains a modest amount of corrosion (48 hrs in 3.5% NaCl), the total fatigue life is even longer than that of those which are brought to fatigue failure from the virgin state. A reasonable explanation is that after the microstructure reorganization, the corrosion actually homogenizes the surface texture by minimizing the damage localization. This theory is supported by the experimental measurement of fractal dimension.

While the fatigue life in the air lasts several hundred kilo-cycles, the one in corrosive environment has a life span which is only 1/4 of the former. On the fractal dimension--number of cycle plot the curves demonstrate a monotonous and rapid rise after reaching a certain stage--in contrary to the one in the dry environment. It indicates the damage, quantified by the fractal dimension, accumulates faster due to the synergistic effects of corrosion and fatigue.

6.2.5 Conclusions

Fractal dimension is sensitive to the surface microstructure change caused by mechanical or chemical damage. As the damage accumulates the fractal dimension of the surface increases, and right before failure occurs the fractal dimension has a high gradient with respect to the fatigue cycle. The damage mechanism of the fatigue in a dry environment and the simultaneous corrosion/fatigue are different. The homogenization effect of a modest amount of corrosion after the initial fatigue can benefit the fatigue life. The primary results show that certain relationships exist between fractal dimension and corrosion/ fatigue process and it may help to gain better insight of some interesting phenomena that lead to a better understanding of the mechanism of damage. The study provides a new approach to quantify corrosion/fatigue with an aim of establishing a theory to assess the damage and to estimate the remaining life of a damaged structure.

References

- Bieman, Leonard H., "Survey of design considerations for 3-D imaging systems," *Proc. SPIE*, Vol. 1005, 138-144 (1988).
- Bieman, Leonard H., Harding, Kevin G., and Boehnlein, Albert, "Absolute measurement using field shifted moiré," *Proc. SPIE*, 1614, 259-264 (1991).
- Blais, F. and Rioux, M., "BIRIS: a simple 3-D sensor," *Proc. SPIE*, Vol. 723, 235 (1986).
- Boehnlein, A. J. and Harding, K. G., "Adaptation of a Parallel Architecture Computer to Phase Shifted Moiré Interferometry," *Proc. SPIE*, 728, 183-193 (1986).
- Boehnlein, Albert, and Harding, Kevin G., "Field shift moiré, a new technique for absolute range measurement," *Proc. SPIE*, Vol. 1163, 2-9 (1989).
- Bruning, J. H., Herriott, D. R., Gallagher, J. E., Rosenfeld, D. P., White, A. D., and Brangaccio, D. J., "Digital Wavefront Measuring Interferometer for Testing Optical Surfaces and Lenses," *Appl. Opt.*, 13, 2693 (1974).
- Buerkle, J., Dunn-Rankin, D., Bowo, K., and Earthman, C., "Rapid Defect Detection by Laser Light Scattering", *Materials Evaluation*, 50(June, 1992), pp. 670-677.
- Carre, P., "Installation et Utilization du Comparateur Photoelectrique et Interferentiel du Bureau International des Poids de Mesures," *Metrologia* 2, 13 (1966).
- Chiang, F. P., "Techniques of Optical Signal Filtering Parallel to the Processing of Moiré-Fringe Patterns," *Exp. Mech.*, 9(11), 523-526 (1969).
- Chiang, F. P., and Juang, R. M., "Vibration analysis of plate and shell by laser speckle interferometry", *OPTICA ACTA*, 23(12), 997-1009, 1976.
- Chiang, F. P., "Random (speckle) patterns for displacement and strain measurement: some recent advances", *Optical Engineering* 24(6), 936-943, 1985.
- Chiang, F. P., "Speckle Metrology", *Metals Handbook* (9th Edition), Vol. 17, p.432-437. The American Society for Metals, Cleveland, 1989
- Chiang, F. P., "Moiré Methods for Contouring, Displacement, Deflection, Slope, and Curvature," *Proc. SPIE*, 153, 113-119 (1978).
- Chiang, F. P., "Moiré Methods of Strain Analysis," in *Manual on Experimental Stress Analysis*, A. S. Kobayashi, Ed., Soc. for Exp. Stress Anal., Brookfield Center, CT, 1983, pp. 51-69.
- Crane, R., "Interference Phase Measurement," *Appl. Opt.*, 24, 3053 (1985).
- Creath, K., "Phase-Measurement Interferometry Techniques," in *Progress in Optics. Vol. XXVI*, E. Wolf, Ed., Elsevier Science Publishers, Amsterdam, 1988, pp. 349-393.
- Chubb, J. P., Morad, T. A., Hockenhull, B. S. and Bristow, J. W., 1995, "The Effect of Exfoliation Corrosion on the Fracture and Fatigue Behavior of 7178-T6 Aluminum," *International Journal of Fatigue*, Vol.17, No.1, pp.49-54.
- Costa, J. M., Sagues, F., and Vilarrasa, M., "Fractal Patterns from Corrosion Pitting", *Corrosion Science*, Vol. 32, No. 5-6, 1991, pp.665-8.
- Creath, K., and Slettemoen, G. A., *J. Opt. Soc. Am. A* 2: 1629-1636 (1985)
- Dai, Y. Z. and Chiang, F. P., "Moiré interferometry applied to topographic contour measurement," *Proc. SPIE*, 954, (1988).
- Dai, Y. Z. and Chiang, F. P., "Estimation of Plastic Strain by Fractal", *SPIE* 1332, 1990,

pp. 767-774.

- Dainty, J. C., *Laser Speckle and Related Phenomena*, Springer-Verlag, 1984.
- Doyle, J. L., Wood, G. R., and Bondurant, D. P., May, 1990, "Using Laser-based Profilometry to Locate and Measure Corrosion Fatigue Cracking in Boiler Tubes," *Materials Evaluation*, pp.556-560.
- Fang, Q., Yiao, H., Tan, Y., and Ku, C., "A fast deformation Analysis Method by Digital Correlation Techniques", SPIE 954 (1988), PP 333-336.
- Favro, L.D., Kuo, P.K., Thomas, Robert L. and Shepard, V., *Materials Evaluation* 51: 1386-89 (1993)
- Flournoy, T. H. and Seher, C. C., 1995, "Corrosion Activity in the Federal Aviation Administration's National Aging Aircraft Research Program," *Corrosion* 95, Orlando, Florida, March 26-31, pp.8/1-8/7.
- Gallagher, J. E. and Herriott, D. R., "Wavefront measurement." U.S. Patent 3,694,088 (1972).
- Geng, Z. Jason, "Rainbow three-dimensional camera: new concept of high-speed three-dimensional vision systems," *Optical Engineering*, 35 (2), 376-383 (1996).
- Gove, R. J., "DMD Display Systems: The Impact of an All-Digital Display," Society for Information Display International Symposium (1994).
- Greivenkamp, J. E., "Generalized Data Reduction for Heterodyne Interferometry," *Opt. Eng.*, 23, 350 (1984).
- Gulker, G., Hinsch, K., Holoker, C., Kramer, A., and Nauscaber, H., *Opt. Eng.* 29: 816-823 (1990)
- Hagemaiier, D.J., Wendelbo, A. H., Jr., and Bar-Cohen, Y., "Aircraft Corrosion and Detection Method", *Material Evaluation*, 43 (March, 1985), pp 426-437.
- Hageniers, Omer L., " DiffractoSight - a new form of surface analysis", SPIE 814 (1987), pp. 193-198.
- Halioua, M., Krishnamurthy, R. S., Liu, H., and Chiang, F. P., "Projection moiré with moving gratings for automated 3-D topography," *Applied Optics* 22 (6), 850-855 (1983).
- Halioua, M., Krishnamurthy, R. S., Liu, H. -C., and Chiang, F. P., "Automated 360° Profilometry of 3-D Diffuse Objects," *Appl. Opt.*, 24(12), 2193-2196 (1985).
- Halioua, M. and Liu, H. -C., "Optical Three-Dimensional Sensing by Phase Measuring Profilometry," *Opt. Lasers Eng.*, 11(3), 185-215 (1989).
- Handdley, Mark C., "Capabilities of Moiré Interferometry for Automotive Body Panel Inspection,"
- Harding, Kevin G., Coletta, Michael P., and VanDommelen, Carl H., "Color encoded moiré contouring," *Proc. SPIE*, Vol. 1005, 169-178 (1988).
- Hariharan, P., Oreb, B. F., and Eiju, T., "Digital Phase-Shifting Interferometry: A Simple Error-Compensating Phase Calculation Algorithm," *Appl. Opt.*, 26, 2504 (1987).
- Hobrough, G. and Hobrough, T., "Stereopsis for robots by iterative stereo image matching," *Proc. SPIE*, Vol. 449, 62 (1983).
- Hornbeck, Larry, J., "Deformable-Mirror Spacial Light Modulators," *Proc. SPIE*, Vol. 1150, (1989).
- Hornbeck, Larry, J., "Current status of the digital micromirror device (DMD) for projection television applications," *IEDM*, 15.1.1 (1993).
- Hornbeck, Larry, J., "Digital Light Processing and MEMS: Timely Convergence for a Bright Future," <http://www.ti.com/dlp/docs/papers/mems/0memsab.htm> (1996).

- Jin, F. and Chiang, F.P., "Nondestructive Evaluation of Corrosion by Fractal Geometry", *Research in Nondestructive Evaluation*, 7(4), 229-238, 1996.
- Jin, F. and Chiang, F.P., "A New Technique Using Digital Speckle Correlation for Nondestructive Inspection (NDI) of Corrosion", *Materials Evaluation*, 55(July, 1997), pp.813-816.
- Jin, Feng & Chiang, F.P., "ESPI and Digital Speckle Correlation Applied to Inspection of Crevice Corrosion on Aging Aircraft", *Research in NDE*, in press, 1997.
- Jin, Feng, Wu, S.Y., and Chiang, F.P., "Quantitative Evaluation of Crevice Corrosion by TADS", The First Joint DoD/FAA/NASA Conference on Aging Aircraft, Ogden, Utah, July 8-10, 1997.
- Jin, Feng, Du, M.L., and Chiang, F.P., "On Fractal Aspect of Corrosion/Fatigue", The First Joint DoD/FAA/NASA Conference on Aging Aircraft, Ogden, Utah, July 8-10, 1997.
- R. Jones and C. Wykes. *Holography and Speckle Interferometry*, p.165. Cambridge University Press, Cambridge, 1990.
- Kawahara, M., Rujita, T., Kurihara, M., Inagaki, H., and Kitagawa, H., 1988, "Corrosion Fatigue Crack Initiation of Carbon Steels in Seawater," *Basic Questions in Fatigue: Volume II, ASTM STP 924*, R.P.Wei, and R.P.Gangloff, Eds., American Society for Testing and Materials, Philadelphia, pp.145-163.
- Komorowski, J. P., Simpson, D. L., and Gould, R. W., "Enhanced Visual Technique for Rapid Inspection of Aircraft Structures", *Materials Evaluation*, 49(December, 1991), pp. 1486-1490.
- Kujawinska, M., "Use of Phase-Stepping Automatic Fringe Analysis in Moiré Interferometry," *Appl. Opt.*, 26(22), 4712-4714 (1987).
- Li, D.W. and Chiang, F.P., "Laws of Laser Speckle Movement", *Optical Engineering*, 25(5), 667-670, 1986.
- Li, D.W. and Chiang, F.P., *J. Opt. Soc. Am. A* 3: 1023-31 (1986)
- Lin, T. H., and Ito, Y. M., 1969, "Mechanics of a Fatigue Crack Initiation Mechanism," *Journal of the Mechanics and Physics of Solids*, Vol.17, pp.511-523.
- Lin, T. H., Lin, S. R., and Wu, X. Q., 1990, "Micromechanics of an Extrusion in High-Cycle Fatigue With Creep," *Journal of Applied Mechanics*, Vol.517, pp.815-820.
- Lokberg, Ole J. and Malmo, Jan T., *Opt. Eng.* 27: 150-156 (1988)
- Long, Q. Y., Li, Suqin and Lung, C. W., "Studies on the fractal dimension of a fracture surface formed by slow stable crack propagation", *J. Phys. D: Appl. Phys.*, Vol. 24, 1991, pp. 602-7.
- Mandelbrot, B. B., "The Fractal Geometry of Nature", pp.15, Freeman, New York, 1982.
- Mehaute, Alain Le / Translated by Jack Howlett, *Fractal Geometries*, CRC Press, 1991, pp. 126.
- Monk, D., "Digital Micromirror Device Technology for Projection Displays," EID Exhibition & Conference (Sandown, UK, 1994).
- Moore, D. T. and Truax, B. E., "Phase-Locked Moiré Fringe Analysis for Automated Contouring of Diffuse Surfaces," *Appl. Opt.*, 18(1), 91-96 (1979).
- Nagahama, Hiroyuki, "A fractal criterion for ductile and brittle fracture", *J. appl. Phys.* Vol. 75, No. 6, 1994, pp. 3220-22.

- Newman, J. W., " Shearographic Inspection of Aircraft Structure", *Materials Evaluation*, 49(September, 1991), pp.1106-1110.
- Osintsev, A.V., Ostrovskii, Yu. I., Shchepinov, V. P., and Yakvlev, V. V., " Determination of a contact surface by the method of speckle photography", *Sov. Phys. Tech. Phys.*, 33(1988), pp. 847-849.
- Osintsev, A.V., Ostrovskii, Yu. I., Presnyakov, Yu. P., and Shchepinov, V. P., " Fringe contrast in correlation speckle photography and in correlation holographic interferometry", *Sov. Phys. Tech. Phys.*, 37(1992), pp.878-882.
- Paoletti, D., Schirripa, G., Carelli, P., Altorio, A. D., *J. Optics* 21: 247-252 (1990)
- Peters, W.H., Ranson, W.F., and Sutton, M.A., "Application of digital correlation method to rigid body mechanics", *Optical Engineering*, 22 (1983), pp738-742.
- Poon, C. Y., Sayles, R. S., and Jones, T. A., " Surface measurement and fractal characterization of naturally fractured rocks", *J. Phys. D: Appl. Phys.*, Vol. 25, 1992, pp. 1269-75.
- Pouet, Bruno F. and Krishnaswamy, Sridhar. *Opt. Eng.* 32: 1360-1369 (1993)
- Power, J. D., *Initial Quality System Reports*, 1994.
- Roach, D. E. and Fowler, A. D., " Dimensionality Analysis of Patterns: Fractal Measurements", *Computers & Geosciences*, Vol. 19, No. 6, 1993, pp. 849-69.
- Reynolds, Rodger L. and Hageniers, Omer L., " Optical Enhancement of Surface Contour Variations", *SPIE* 954 (1988), pp. 208-216.
- Russ, John C., *The Image Processing Handbook*, CRC Press (1992), pp219.
- Russell, S. S., Sutton, M. A., and Chen, H. S., " Image Correlation Quantitative Nondestructive Evaluation of Impact and Fabrication Damage in a Glass Fiber-Reinforced Composite System", *Materials Evaluation*, 47(May, 1989), pp. 550-557.
- Sampsel, J. B., "The digital micromirror device," *Proceedings of the 7th ICSS&A* (Yokohama, Japan, 1993).
- Sampsel, J. B., "An Overview of the Performance Envelope of Digital Micromirror Device Based Projection Display Systems," *SID Digest*, 669-672 (1994).
- Sansoni, G., Docchio F., Minoni U., and Bussolati C., "Development and characterization of a liquid crystal projection unit for adaptive structured illumination," *Proc. SPIE*, 1614, 78-86 (1991).
- Schwider, J., Burow, R., Elssner, K. E., Grzanna, J., Spolaczyk, R., and Merkel K., "Digital Wavefront Measuring Interferometry: Some Systematic Error Sources," *Appl. Opt.*, 22, 3421 (1983).
- Streckenrider, J. Scott & Wagner, James W., *Optics and Lasers in Engineering* 22: 3-15(1995)
- Shaw, M. M., Harvey, D. M., Hobson, C. A., and Lalor, M. J., "Non-contact ranging using dynamic fringe projection," *Proc. SPIE*, Vol. 1163, 22-29 (1989).
- Spooren, Rudie, *Opt. Eng.* 31: 1000-1007 (1992)
- Srinivasan, V. H., Liu, H. -C., and Halioua, M., "Automated Phase-Measuring Profilometry of 3-D Diffuse Objects," *Appl. Opt.*, 23(18), 3015-3018 (1984).
- Srinivasan, V. H., Liu, H. -C., and Halioua, M., "Automated Phase-Measuring Profilometry of 3-D Diffuse Objects," *Appl. Opt.*, 24(2), 185-188 (1985).
- Stahl, Philip H., "White-light phase-measuring interferometry," *Proc. SPIE*, Vol. 1332, 720-728 (1990).

- Stumpf, K. D., "Real-Time Interferometer," *Opt. Eng.*, 18, 648 (1979).
- Svetkoff, D. J., Leonard, P. F., and Sampson, R. E., "Techniques for real-time," *Proc. SPIE*, Vol. 521, 302 (1984).
- Takasaki, H., "Moiré Topography," *Applied Optics* 9 (6), 1457-1472 (1970).
- Toyooka, S. and Iwaasa, Y., "Automatic Profilometry of 3-D Diffuse Objects by Spatial Phase Detection," *Appl. Opt.*, 25(10), 1630-1633 (1986).
- Wizinowich, P. L., "System for Phase Shifting Interferometry in the Presence of Vibration," *Proc. SPIE*, 1164, 25 (1989).
- Wizinowich, P. L., "Phase Shifting Interferometry in the Presence of Vibration: A New Algorithm and System," *Appl. Opt.*, 29, 3271 (1990).
- Wong, Po-zen, "The Statistical Physics of Sedimentary Rock", *Physics Today*, Vol. 41, No. 12, 1988, pp. 24-32.
- Wyant, J. C., "Use of an ac Heterodyne Lateral Shear Interferometer with Real-Time Wavefront Correction Systems," *Appl. Opt.*, 14, 2622 (1975).
- Wyant, J. C. and Prettyjohns, K. N., "Optical Profiler Using Improved Phase-Shifting Interferometry," U.S. Pat. 4,639,139 (1987).
- Yoshizawa, Toru and Tomisawa, Teiyu, "Moiré topography with the aid of phase shift method," *Proc. SPIE*, 1554B, 441-450 (1991).
- Younse, J. M., "Mirror on a chip," *IEEE Spectrum*, 30(11), 27 (1993).
- Zhang, Shou-zhu and Lung, Chi-wei, "Fractal dimension and Fracture toughness", *J. Phys. D: Appl. Phys.*, Vol. 22, 1989, pp. 790-3.

Figures

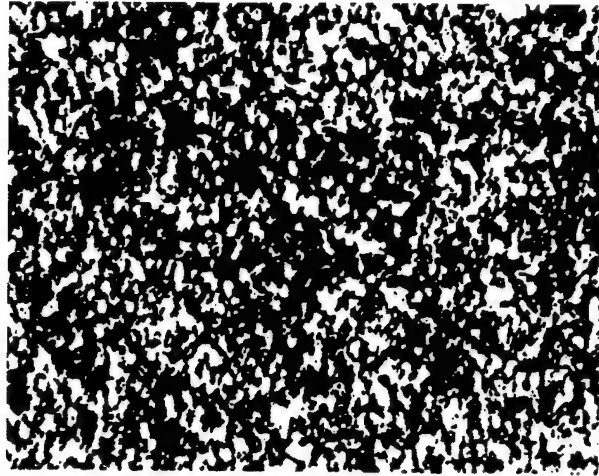


Fig. 2.1 Laser speckle pattern

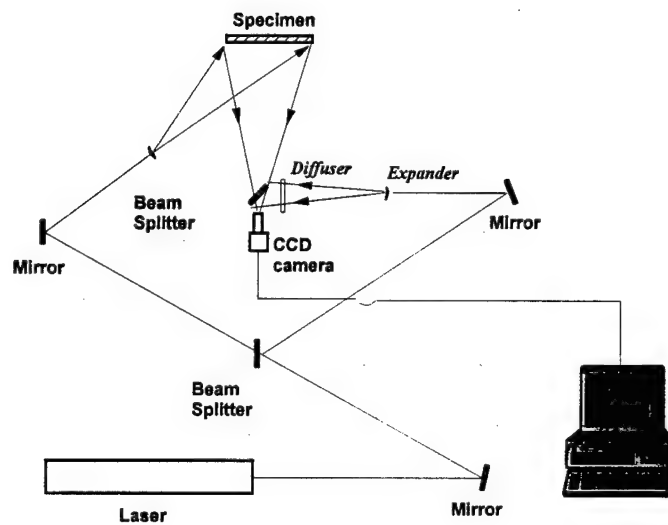


Fig. 2.2 Configuration for Electronic Speckle Pattern Interferometry (ESPI)

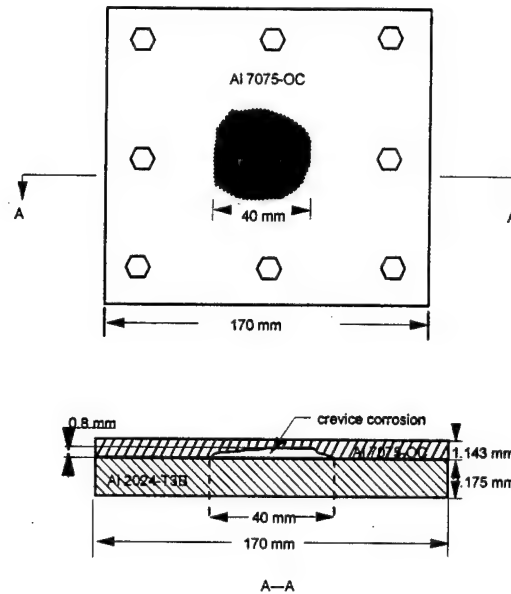


Fig. 2.3 Schematic for specimen-I with crevice corrosion

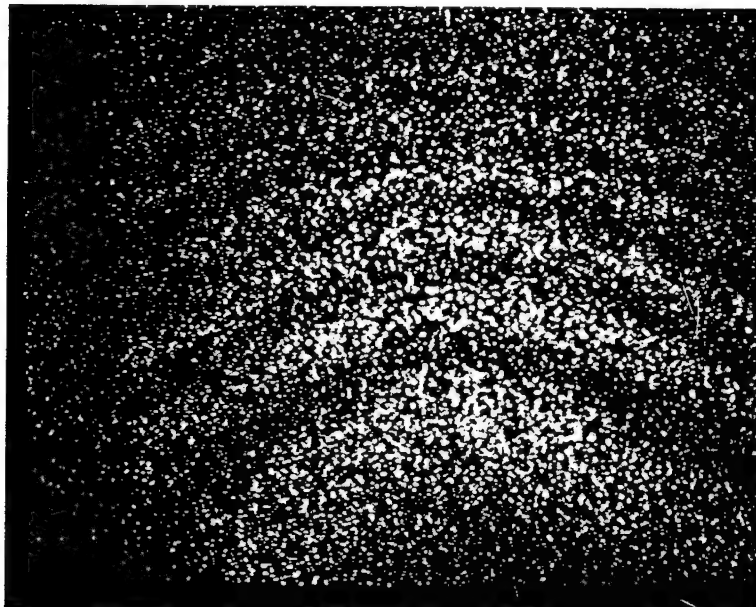


Fig. 2.4-a ESPI fringe pattern of specimen without crevice corrosion (thermal loading)

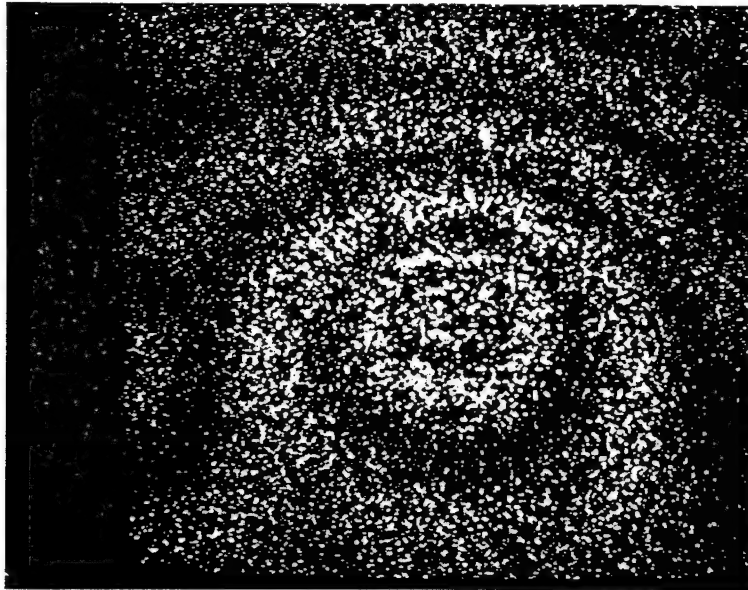


Fig. 2.4-b ESPI fringe pattern of specimen with crevice corrosion (thermal loading)

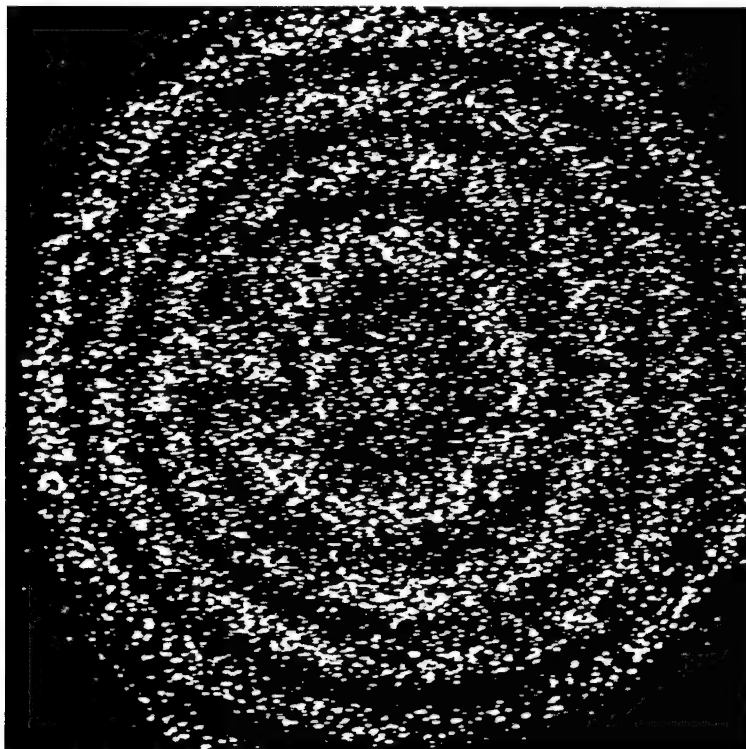


Fig. 2.5 Fringe of ESPI (vacuum loading) reveals the crevice corrosion

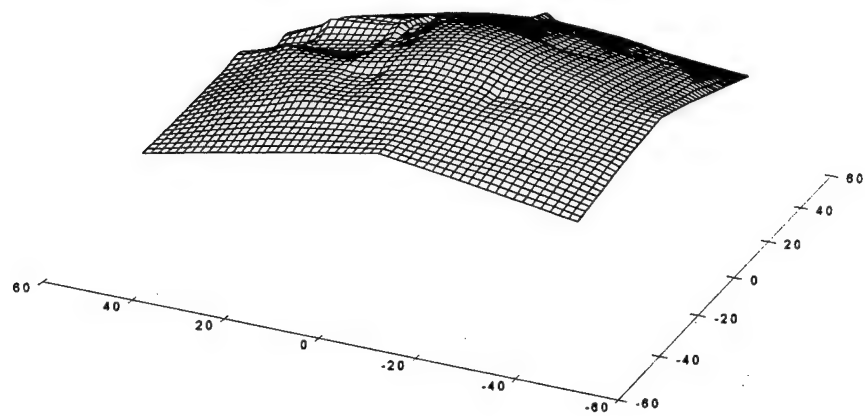


Fig. 2.6 3D view of the out-of-plane deformation field

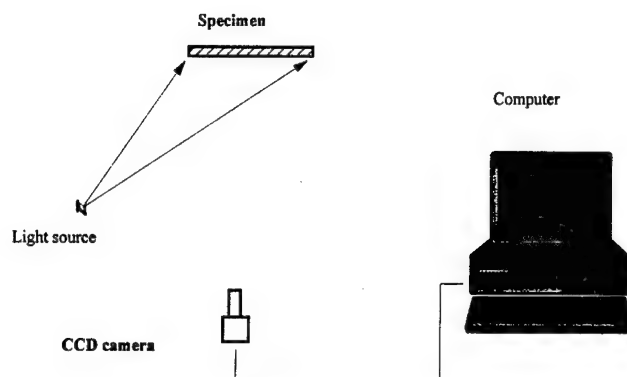


Fig. 3.1 System Configuration

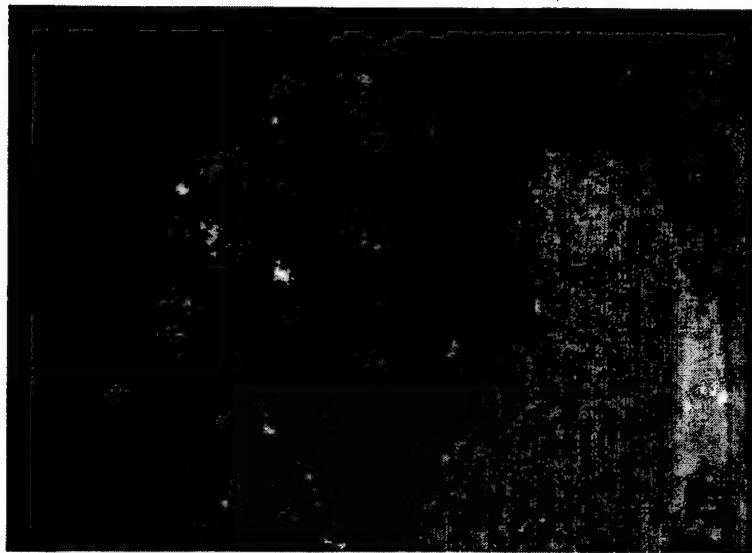


Fig. 3.2 Sample of pitting corrosion

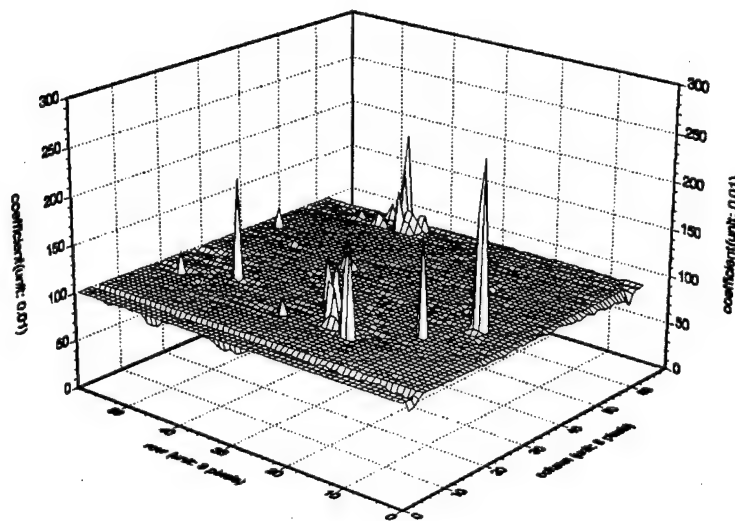


Fig. 3.3 Pits revealed as drastic change of correlation



Fig. 3.4 Artificial pitting sample

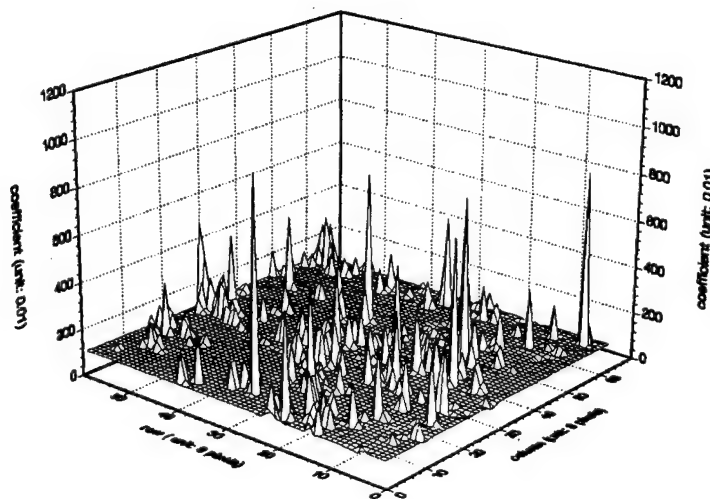


Fig. 3.5 3D plot of cross-correlation coefficient from artificial pitting sample

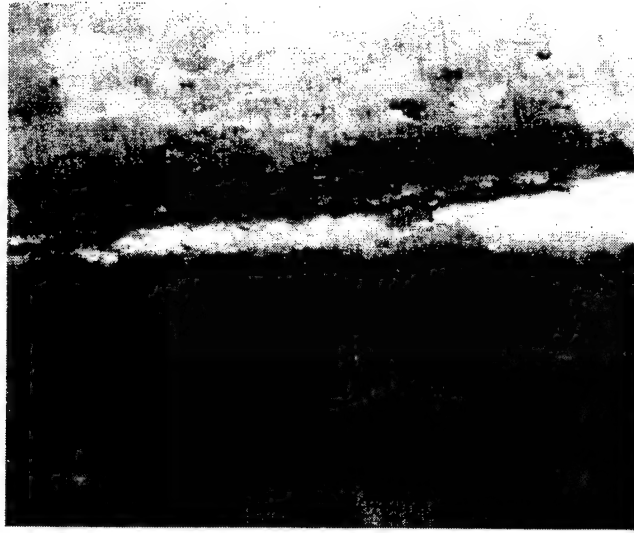


Fig. 3.6 Stress-corrosion crack

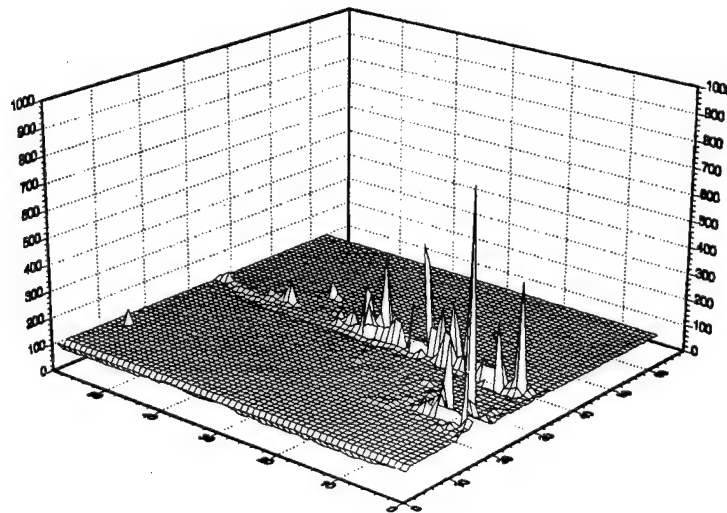


Fig. 3.7 3D plot of cross-correlation coefficient from cracking sample

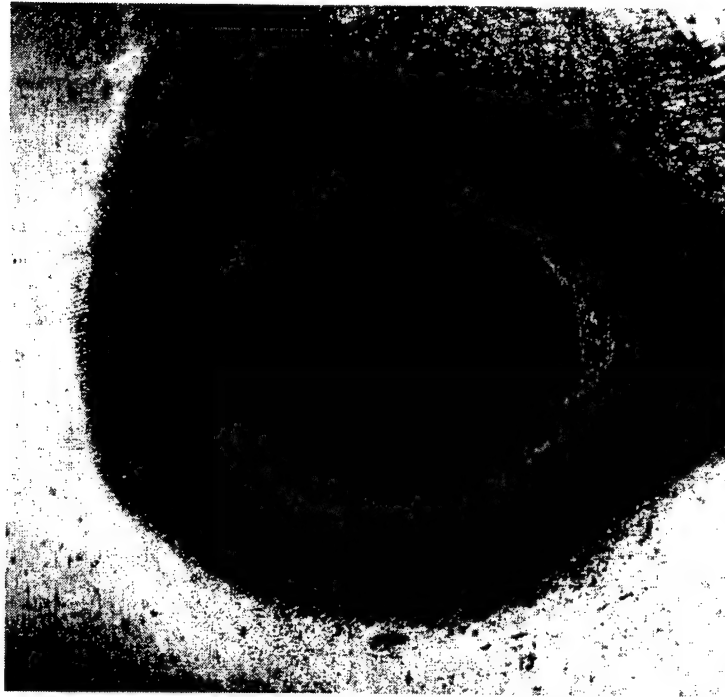


Fig. 3.8 Inside-view of the crevice corrosion

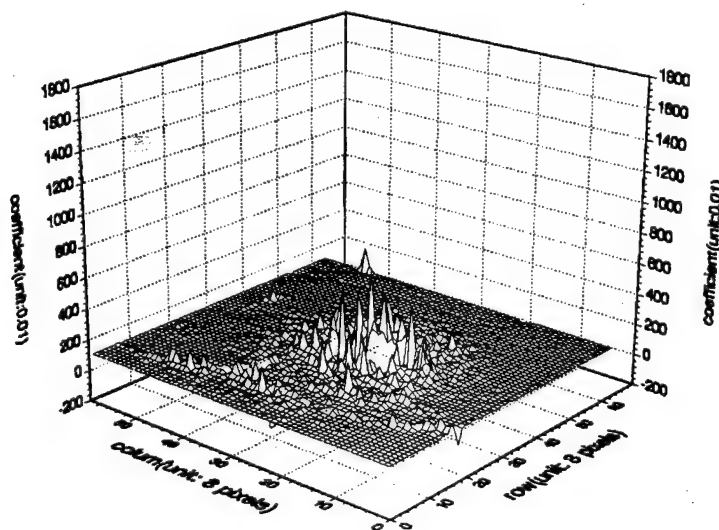
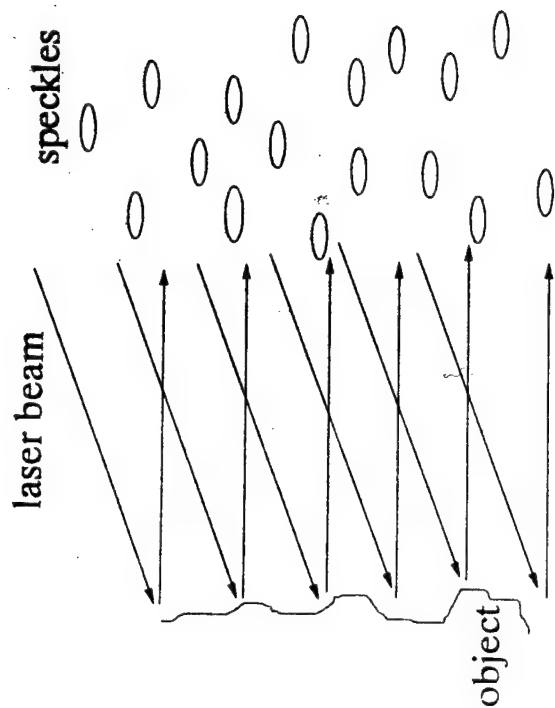
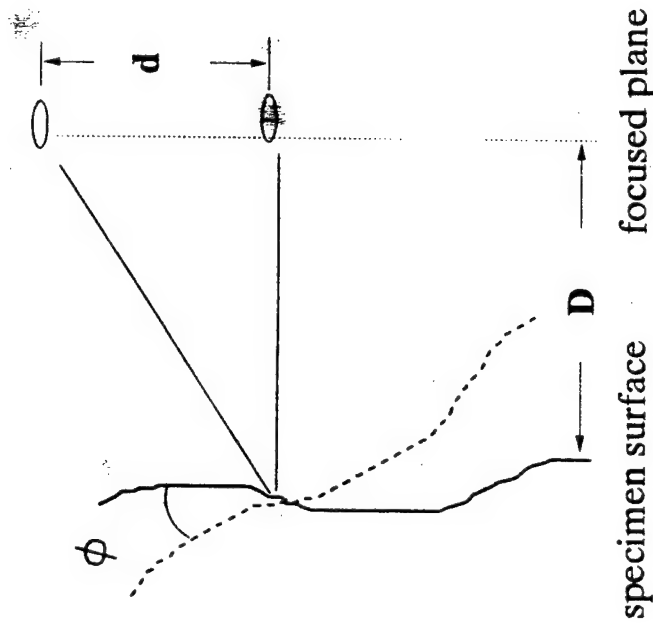


Fig. 3.9 3D view of correlation coefficient from crevice corrosion sample (heat loading)



(a)



(b)

Fig. 4.1 Principle of the laser speckle method
(a) Formation of speckles (b) Speckle movement due to tilt

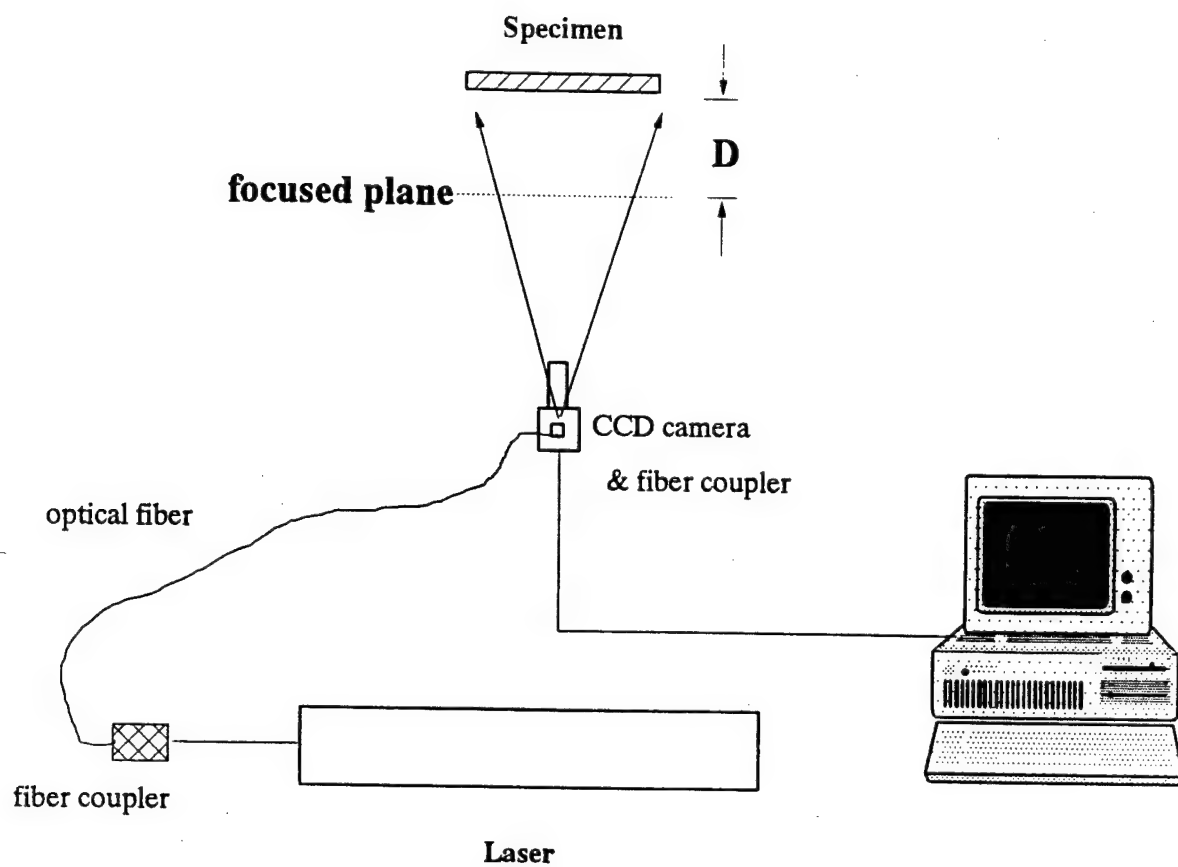


Fig. 4.2 System setup of TADS

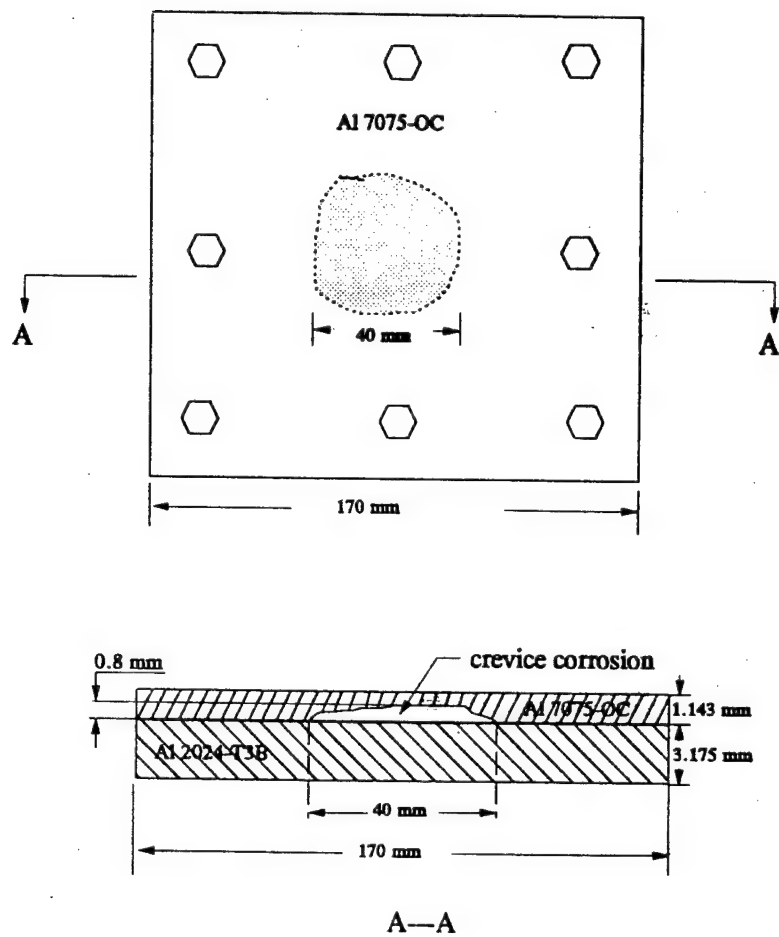


Fig. 4.3 The schematic of a crevice corrosion specimen

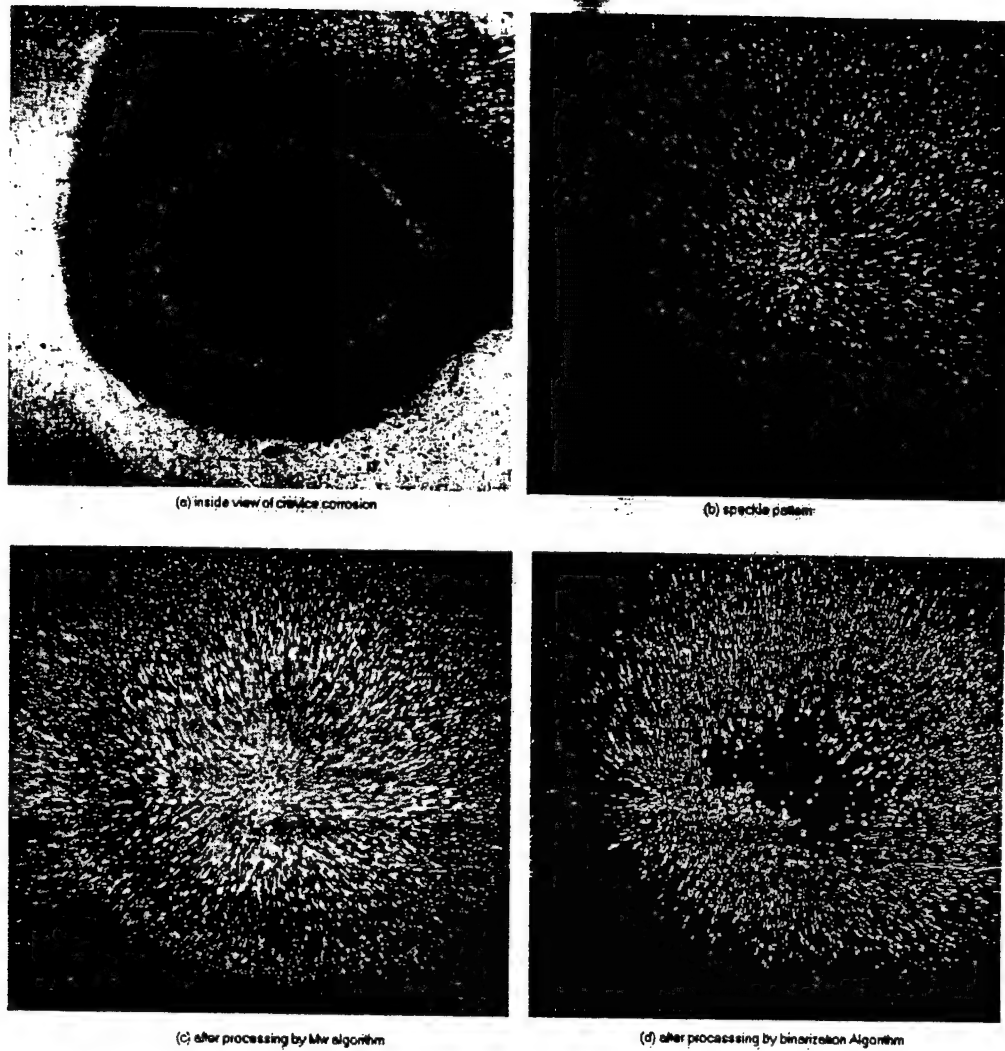
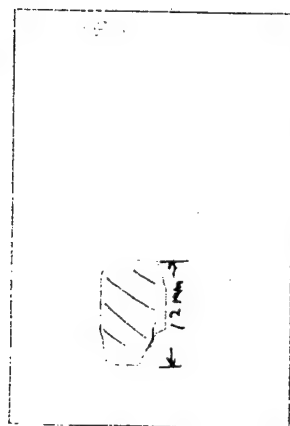
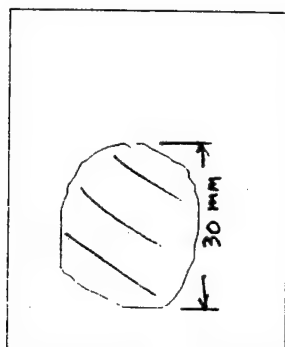
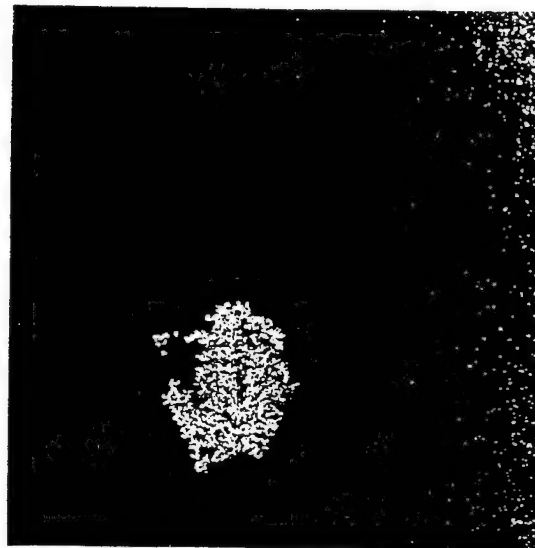


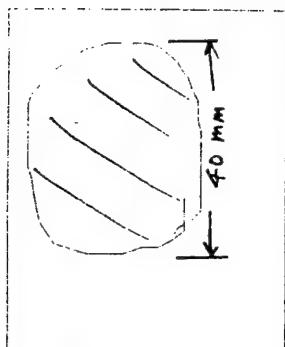
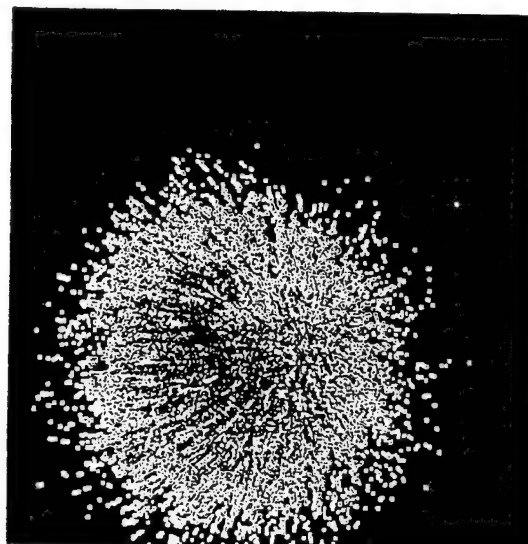
Fig. 4.4 Crevice corrosion and speckle patterns of TADS



(a)



(b)



(c)

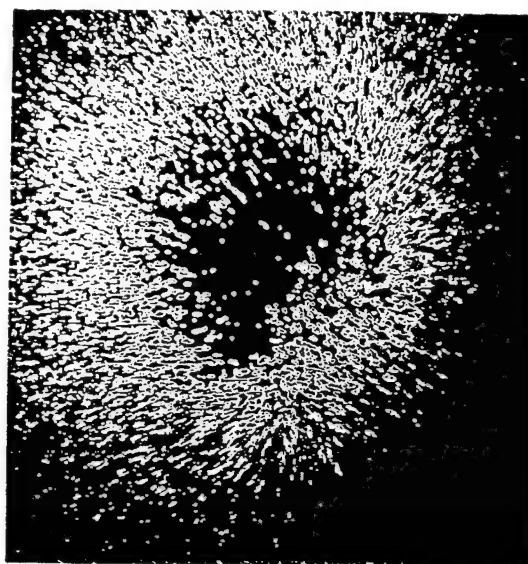


Fig. 4.5 Hidden defects determined by TADS: (a) to (c) crevice corrosion of

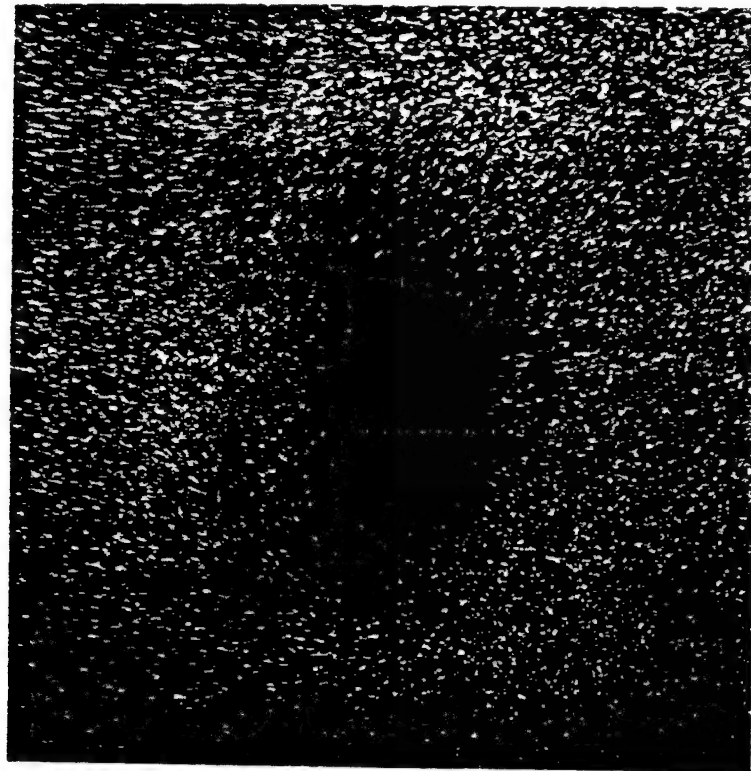


Fig. 4.6 (a) Crevice corrosion under a bolt and (b) Its speckle pattern

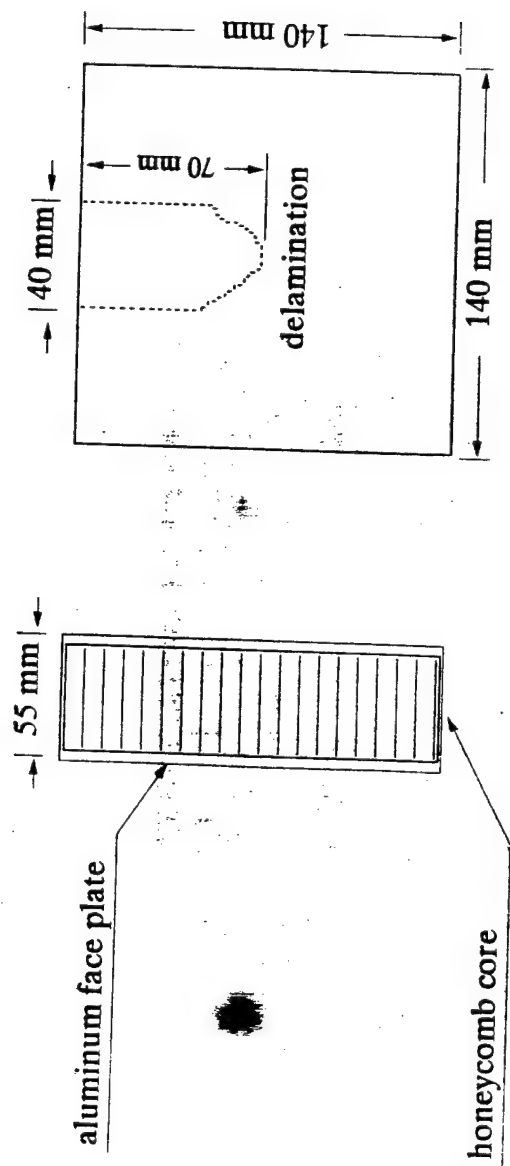
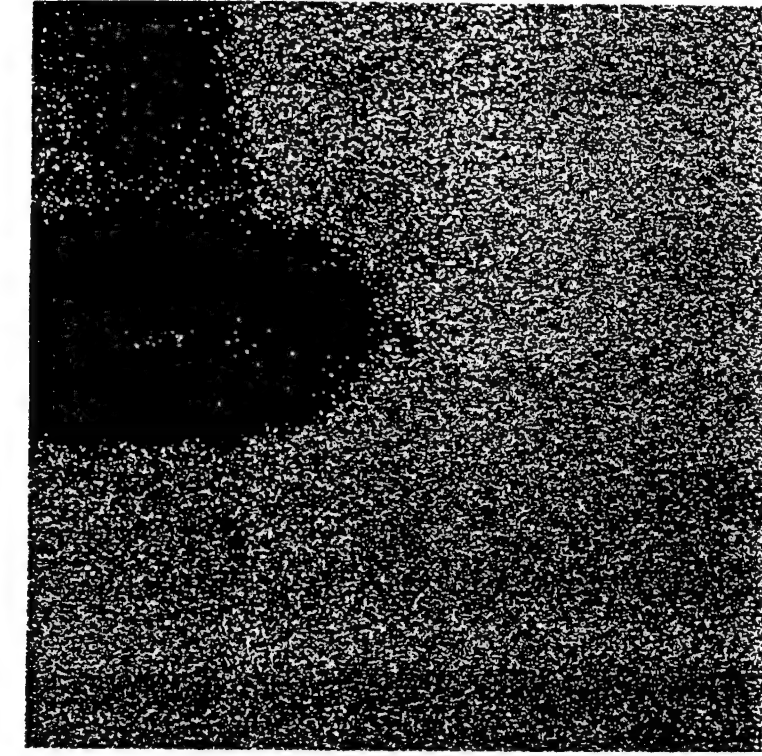


Fig. 4.7 (a) Honeycomb structure_plate with delamination



(c) Enhanced pattern

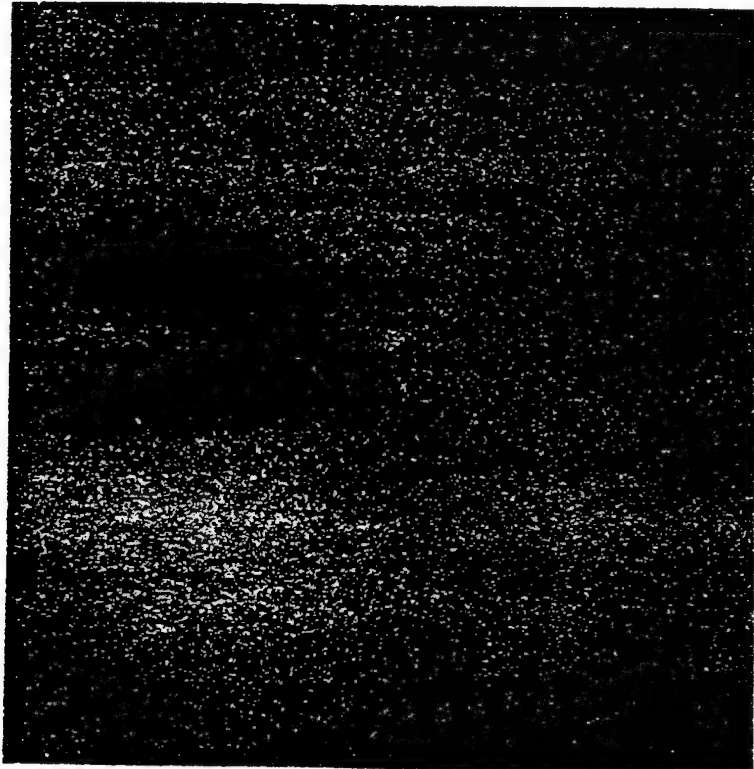


Fig. 4.7 (b) Resulting speckle pattern

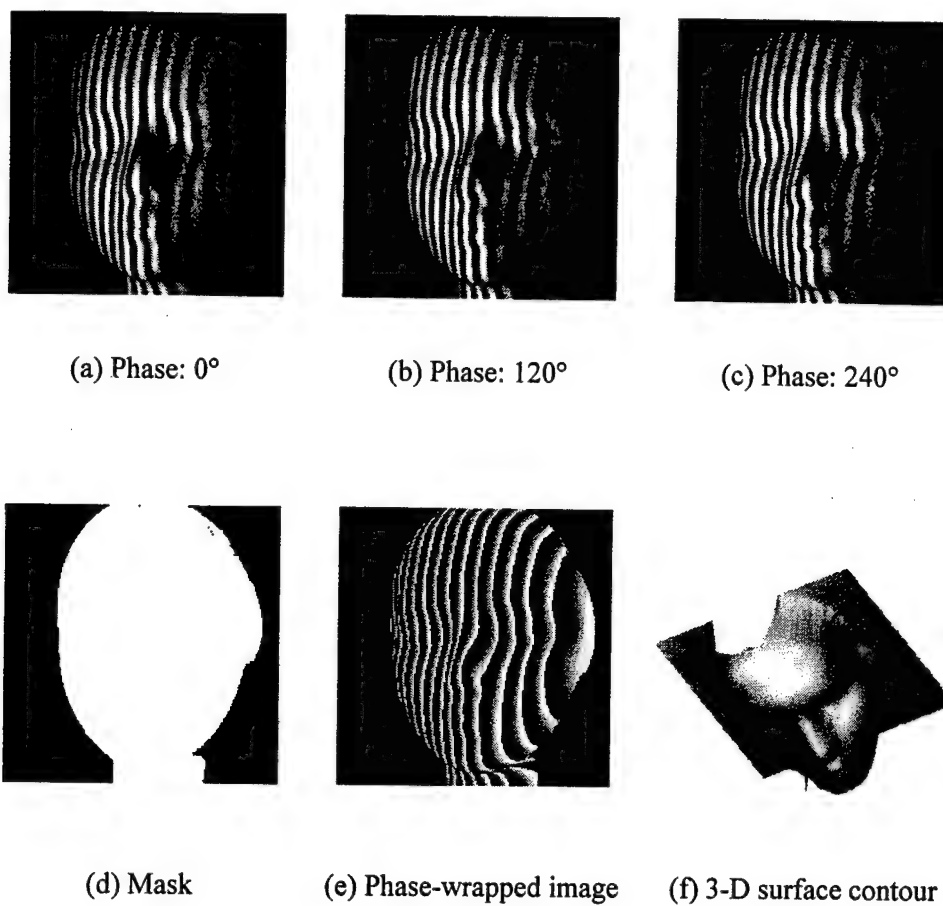


Figure 5.1 3-D surface contouring results of a dummy face.

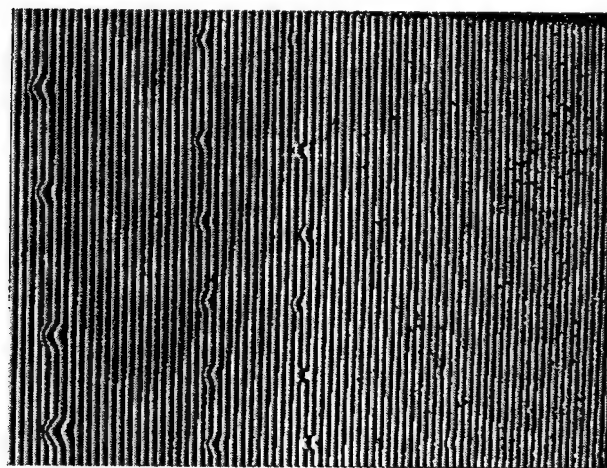


Figure 5.2 Phase-wrapped pattern reveals pitting

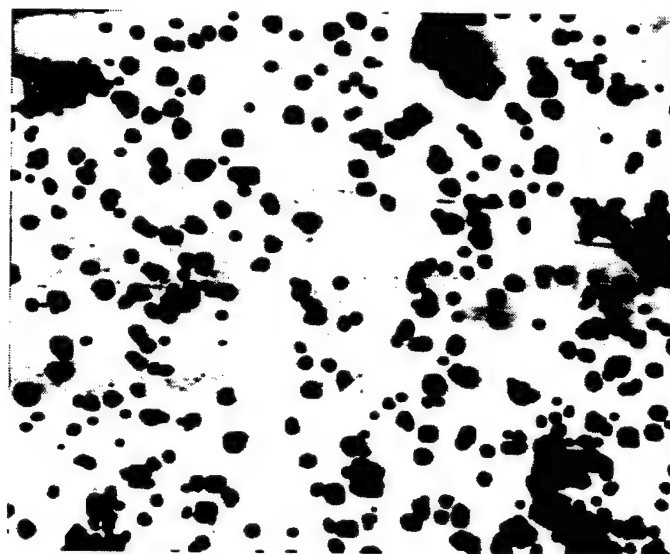


Fig. 6.1.1 Pitting Corrosion Pattern

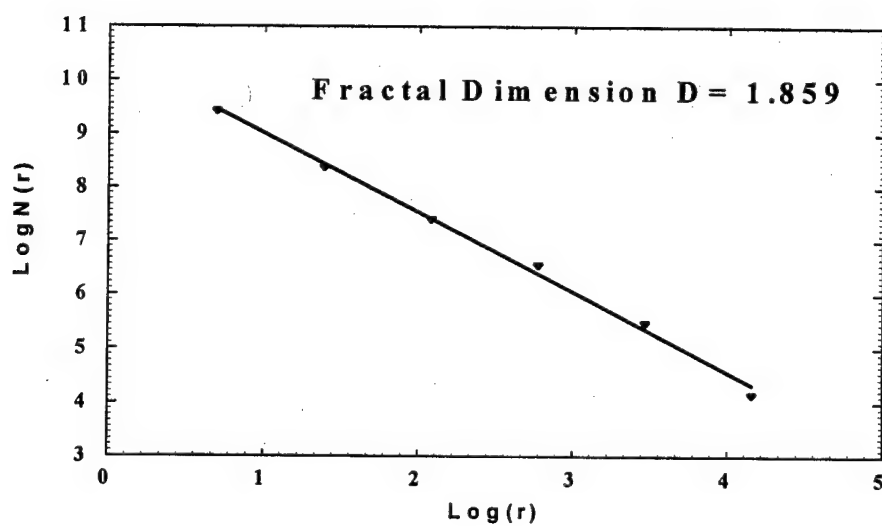
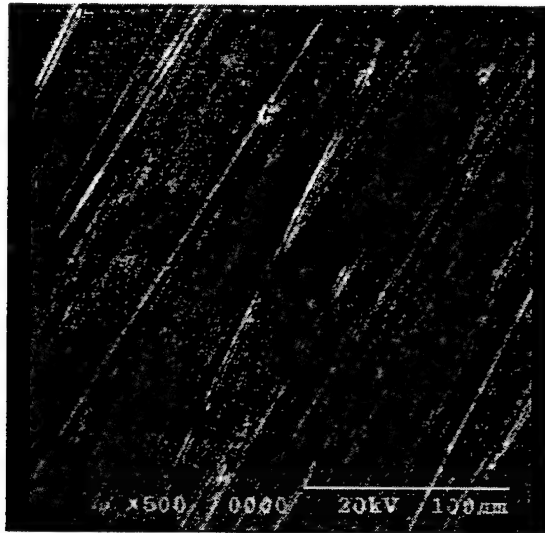
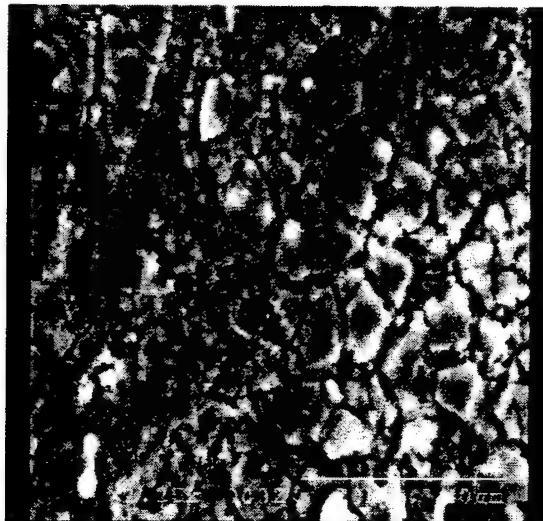


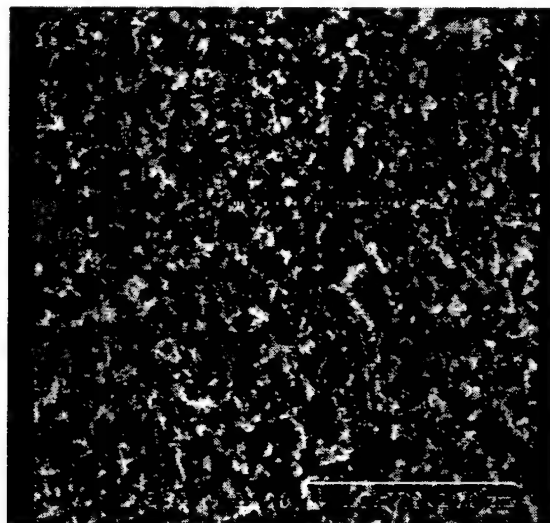
Fig. 6.1.2 Fractal Dimension of Pitting Surface



(a)



(b)



(c)

Fig. 6.1.3 Microstructures of (a) polished surface (b) intergranular corrosion (c) pitting corrosion

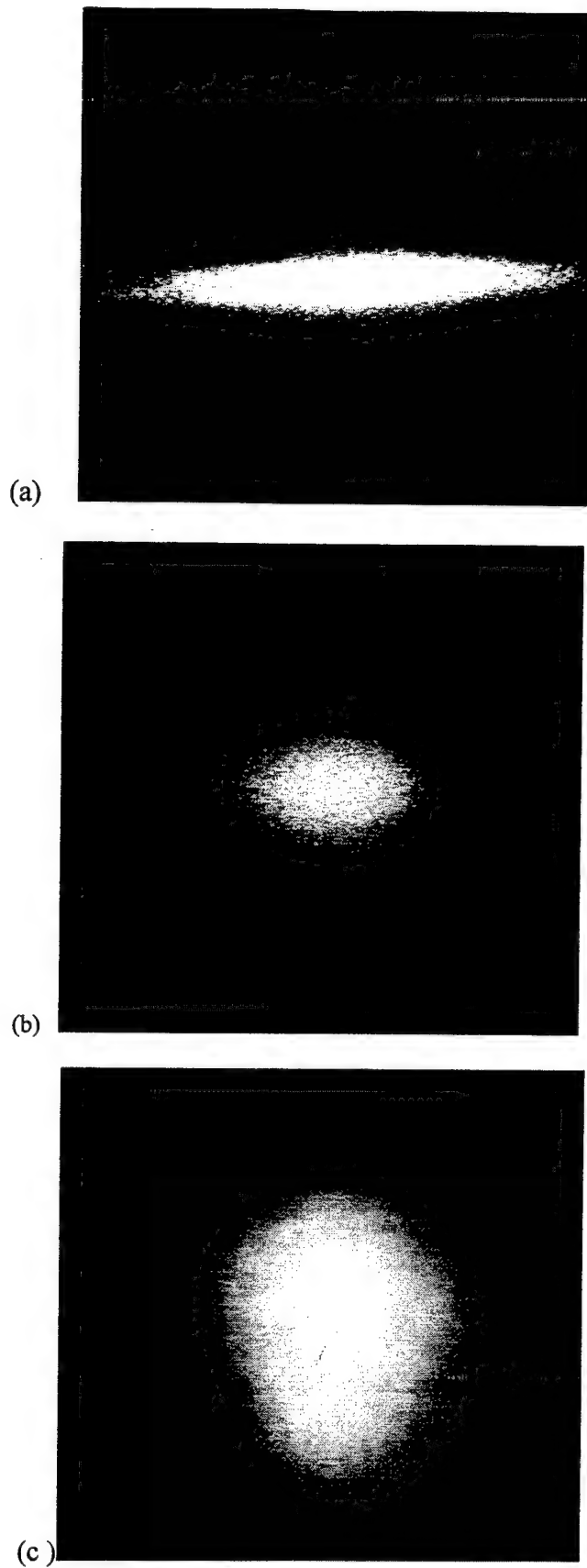


Fig. 6.1.4 Power spectrum of (a) polished surface (b) intergranular corrosion (c) pitting corrosion

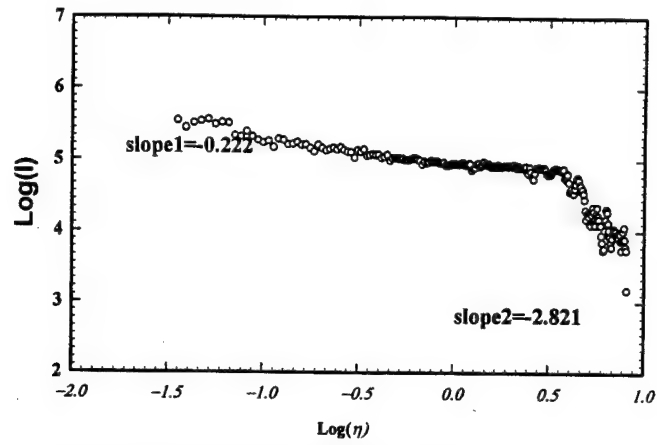


Fig.6.1.5(a) Polished surface (without corrosion)

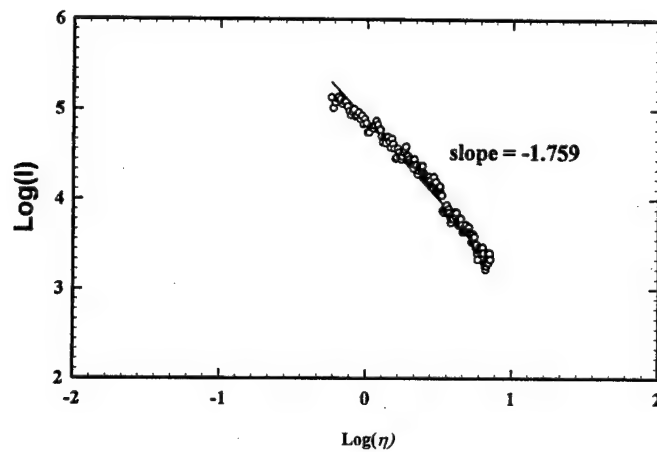


Fig.6.1.5(b) Intergranular corrosion (high part)

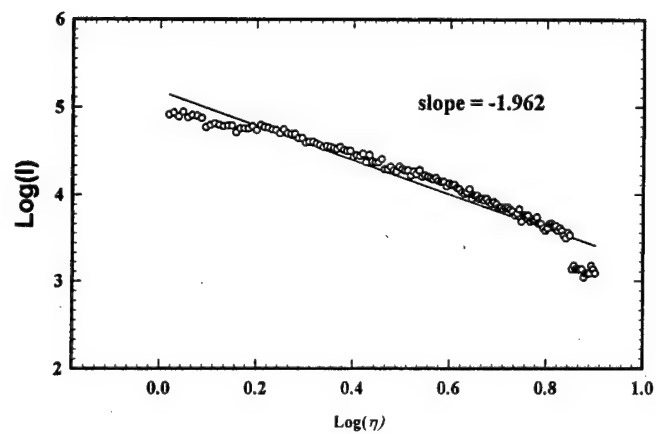


Fig.6.1.5(c) Pitting corrosion (high part)

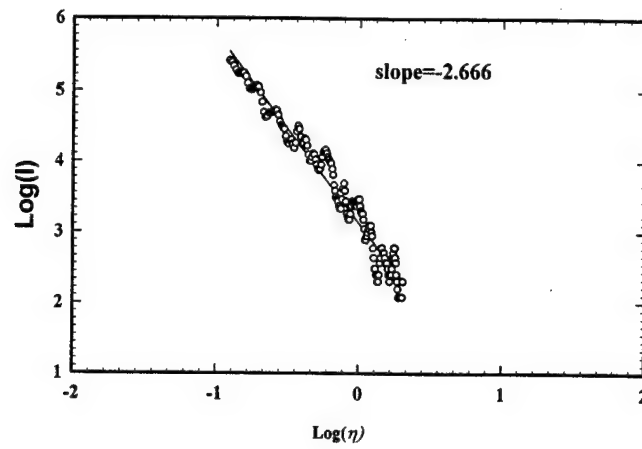


Fig.6.1.6(a) Virgin sample

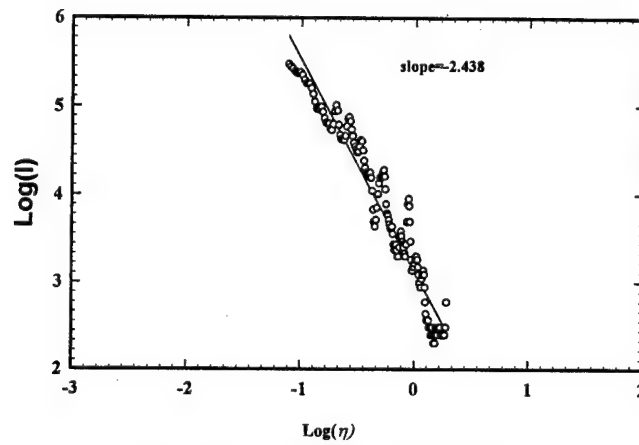


Fig.6.1.6(b) Corroded in 3.5% NaCl for 12 hrs

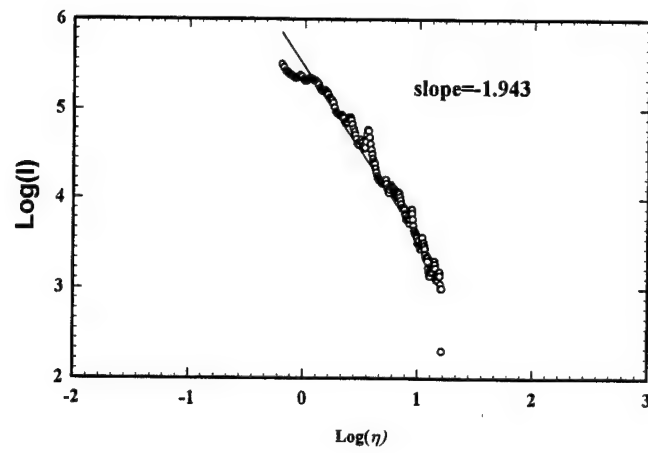


Fig.6.1.6(c) Corroded in 3.5% NaCl for 100 hrs

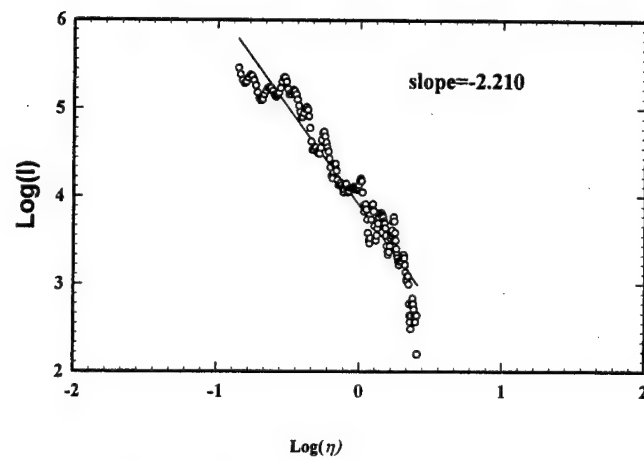


Fig.6.1.6(d) Corrosion and fatigue

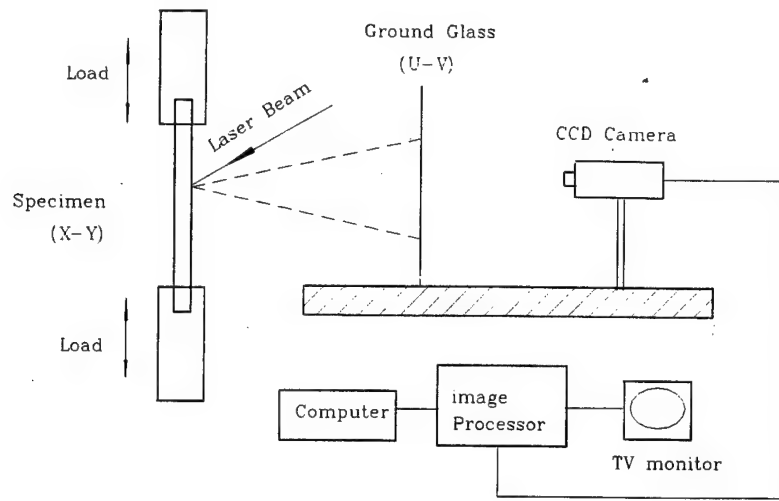


Fig. 6.2.1 Experimental Set-up for Fractal Damage Sensor (FDS)

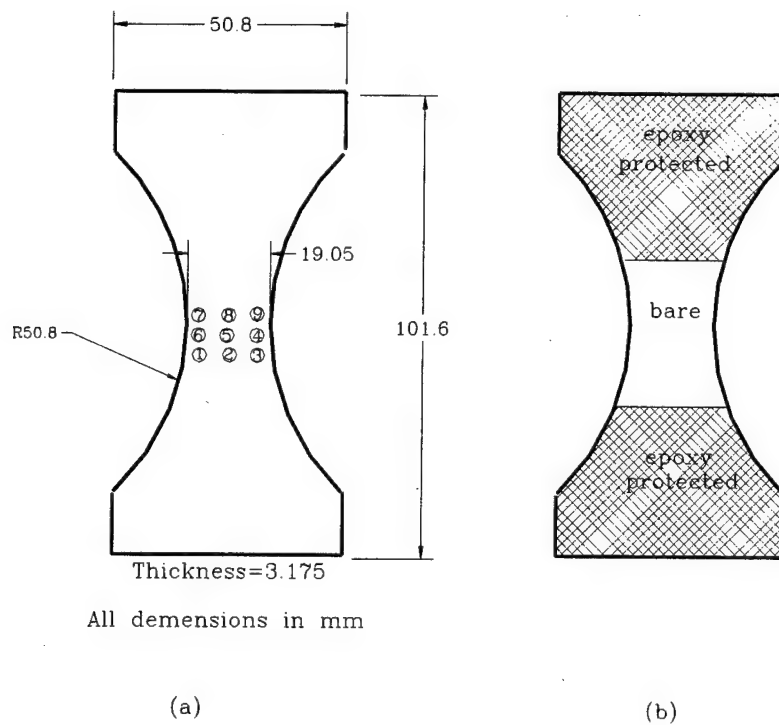


Fig.6.2.2 (a) Specimen geometry, circle spots are monitoring points; (b) the central area of specimen is bared and other wise is epoxy protected.

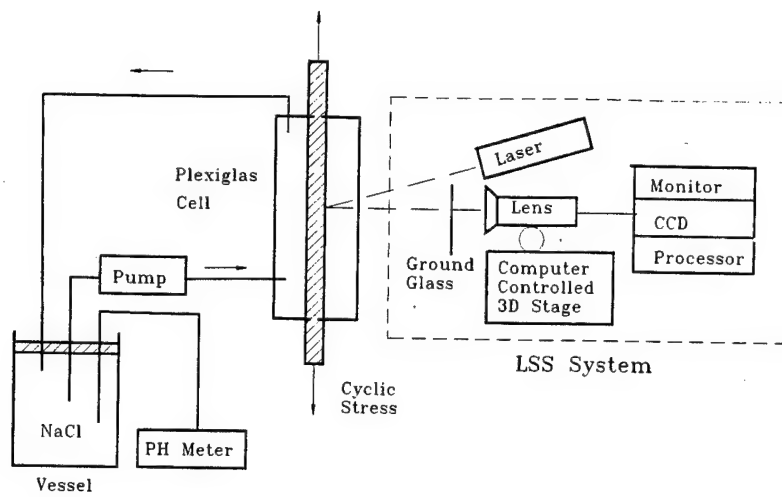


Fig.6.2.3 Schematic set-up for corrosion fatigue simultaneous test and in-situ monitoring.

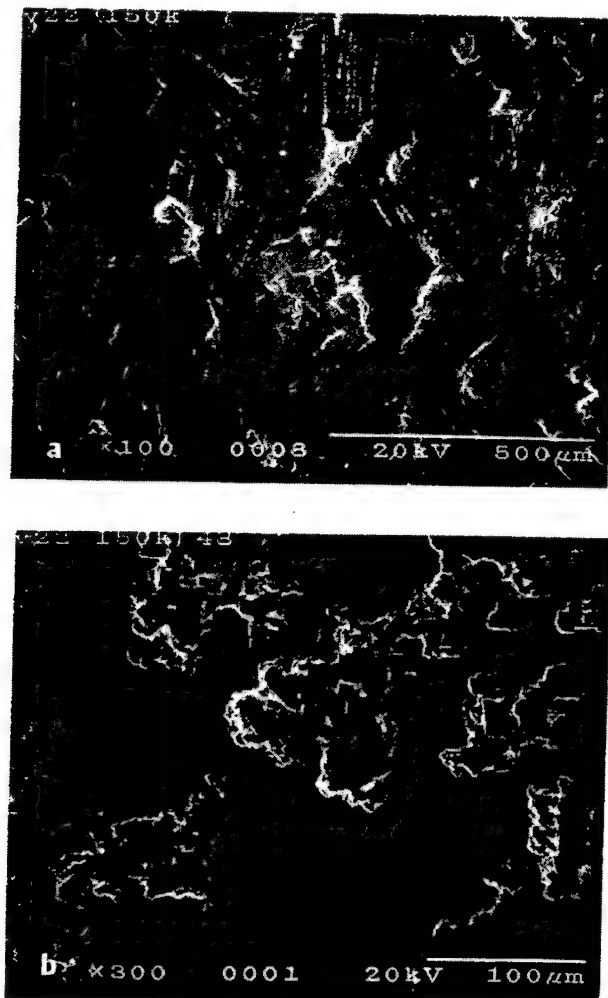


Fig.6.2.4 Micro-damage of Al2024-T3 due to (a) fatigue only and (b) fatigue then corrosion

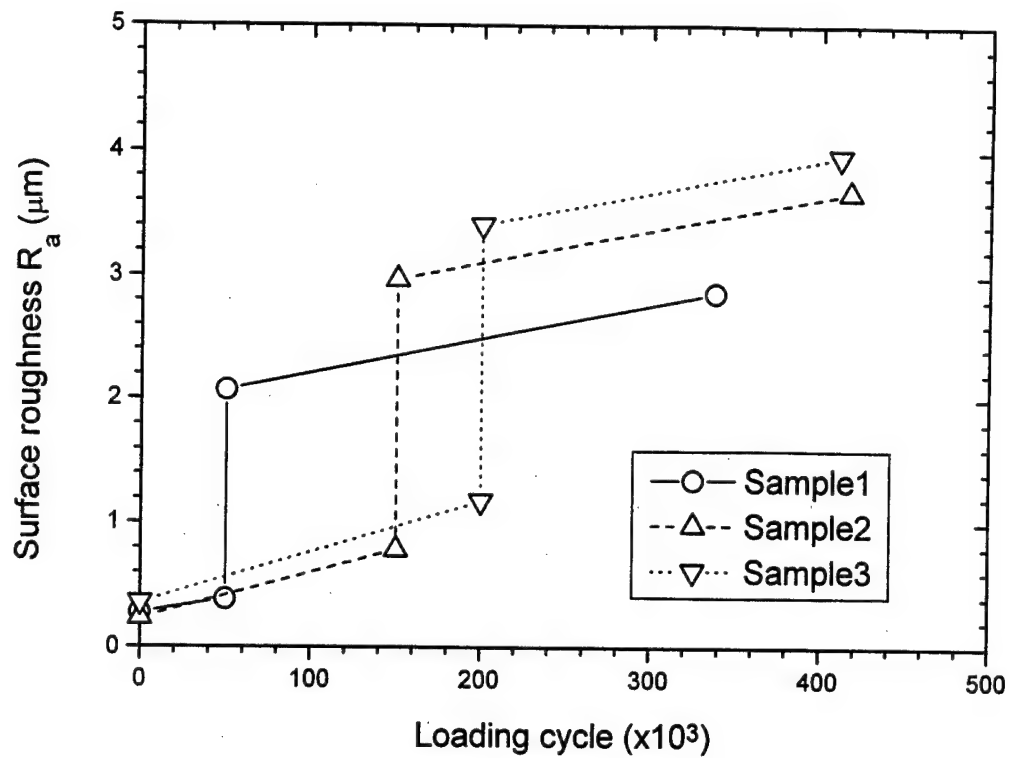


Fig.6.2.5 Mechanical measured surface roughness change due to the sequential fatigue, corrosion and fatigue (vertical jumps due to corrosion only—samples immersed in sea water for 48 hours)

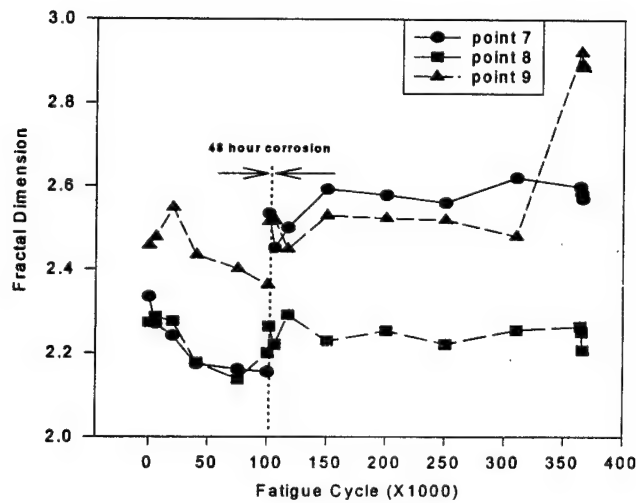


Fig. 6.2.6(a) Whole Sequence of Fatigue-Corrosion-Fatigue

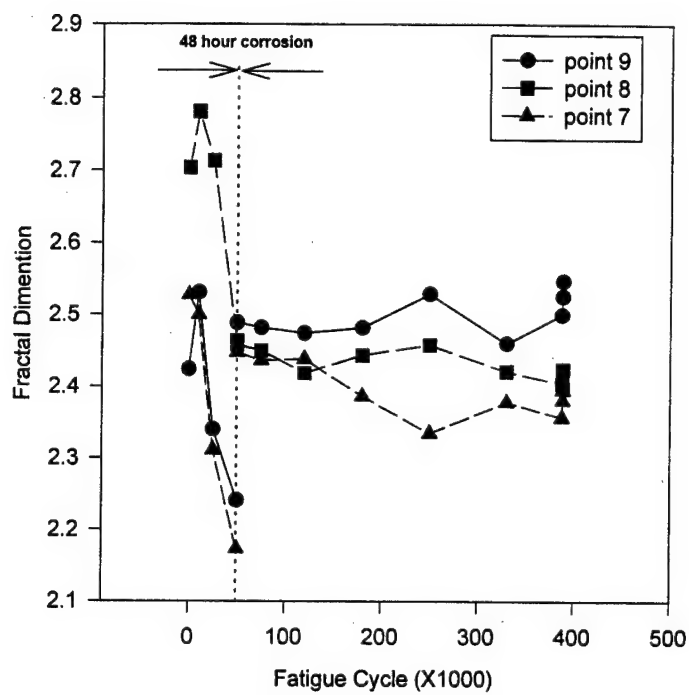


Fig.6.2.6(b) Sequence of fatigue-corrosion-fatigue

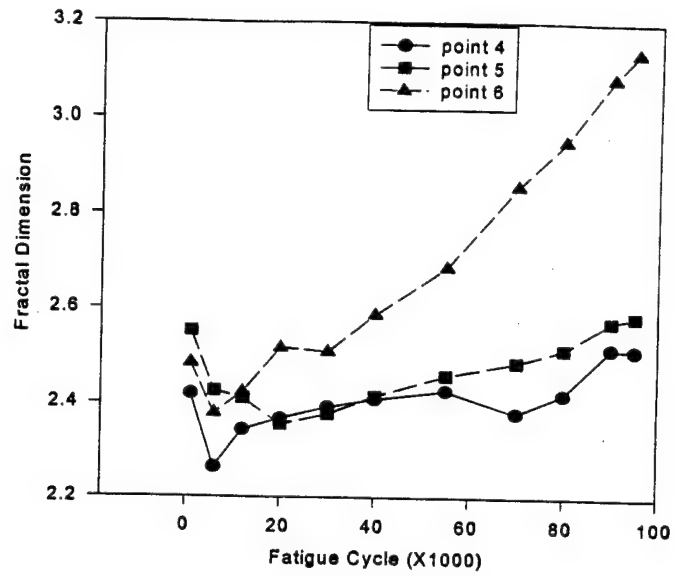


Fig. 6.2.7 Simultaneous corrosion-fatigue

Part II Studies of Corrosion and Corrosion Fatigue

1. Introduction

It is reported that the cost of fracture to the U.S. is estimated to be more than 100 billion per year. 70-90 percent of all structural fractures result from fatigue. If the fatigue process is combined with a chemically reactive environment, the synergistic process takes place and it is generally referred as corrosion fatigue.

Many of the aircraft in service today have exceeded their original design life span and economic considerations have driven the industry toward the retention of older aircraft (Flournoy and Seher, 1995). These aging aircraft exhibit various kinds of damage due to fatigue and corrosion (Chubb et al., 1995). Crack initiation is a function of many surface features such as the presence of pits or crevices, fatigue induced voids, intrusions and extrusions (Lin and Ito, 1969, Lin et al., 1990), etc. The influence of a corrosive environment on fatigue has typically been studied by considering the environment and fatigue behavior simultaneously. The results of such tests indicate a significant synergism between corrosion and fatigue (Pao et al., 1988, Piascik and Gangloff, 1990, Duquette, 1990). However, there are situations wherein corrosion and fatigue processes do not occur at the same time. For examples, when an aircraft is in flight, cyclic loading due to engine vibration and flutter is at its maximum, and corrosive processes due to moisture and/or other factors are minimal. And when the aircraft is on the ground the corrosive process is at its maximum; and there is little or no cyclic loading at play. Thus, it is necessary to investigate the effect of fatigue and corrosion when the two aging factors are acting sequentially. The systematic studies of corrosion fatigue include following steps. First, the influence of corrosion on the fatigue properties of Al 7075 and Al 2024-T3 is studied (Du & Chiang et al, 1995, 1998a). Second, we will present some results on the aging process of first being subject to fatigue and then to corrosion and then to fatigue again (Du & Chiang et al, 1995, 1998b). Third, the synergism of corrosion and fatigue

interaction is studied. And finally, the influence of acetone degreasing on the corrosion behavior of Al2024-T3 is investigated (Kagwade, Clayton, Du & Chiang, 1996, 1997).

It is well known that cyclic loading produces a random roughening of the surface (Wood, 1958, May, 1960 and Hunsche and Neumann, 1988). Surface roughness will eventually lead to crack initiation and then crack growth and finally material failure. We developed the Laser Speckle Sensor technique for surface roughness measurement and its principle is introduced in the next chapter.

2. Surface Roughness and its Measurement Techniques

2.1 Introduction

From a global view point the damage appears to be randomly oriented resulting in surface roughness change. Fig. 2.1 shows the surface feature of a fatigue sample. The surface roughening is manifested as microscopic “hills” and “valleys” at sites where slip bands emerge at the free surface. As the cumulative strain increases, the valleys between the peaks grow deeper and deeper. The deepest valleys may eventually develop into cracks. Lin and Ito (1969) considered the microstrain fields in and around the slip bands and proposed the first quantitative micromechanics theory of fatigue crack initiation. The microstress field reveals that cyclic plastic shear strains cause the start and monotonical growth of extrusion or intrusion and the nucleation of fatigue crack. Ma and Laird (1989a, 1989b) have examined the surface roughening in fatigued Cu by observing extrusions and intrusions on the surface. In the case of metals in corrosive environment, the environment produces surface roughening (Hunsch & Neumann, 1988). Pitting is the most common and important form of corrosion. It is observed that fatigue cracks initiate on the surfaces roughened by corrosion pitting (Kawahara et al., 1988, Doyle et al., 1990). The facts and the related studies show that the roughness of materials caused by cyclic fatigue or corrosion governs the initiation of cracks and may be used to define the development of fatigue damage. Surface roughness can be generally measured in two ways: contact and non-contact.

2.2 Contact Measurement Technique

The typical contact method is to use mechanical profilometry technique. For several decades stylus instruments have provided the only reliable means of obtaining a quantitative record of the shape of a specimen surface. Average roughness (R_a) is generally used to quantify the surface roughness information. It is defined by

$$R_a = \frac{1}{L} \int_0^L |f(y)| dy \quad (2.1)$$

where $f(y)$ is the departure of the profile from the mean line and L is the length of the profile.

One of the main criticisms of R_a is that it cannot distinguish between profiles of different shapes.

2.3 Laser Speckle Sensor

Laser Speckle Sensor (LSS) technique is a non-contact, nondestructive optical technique based on laser speckle and computerized image processing.

2.3.1 The Relationship between Surface Variation and Speckle Pattern

When an opaque surface is illuminated by a narrow laser beam, the rough surface scatters the laser beam in a broad spectrum of directions. The reflected wavelets mutually interfere to form a random interference pattern called speckles (Chiang, 1978). In this Laboratory, laser speckle (Dai et al., 1991, Chiang et al., 1995, Kato et al., 1995) with computer based image processing is used in surface roughness monitoring and damage analysis.

The LSS technique is briefly described here. The schematic of the set-up of LSS is shown in Fig.2.2. A laser illuminates a specimen surface in X-Y plane and the light scattered from the surface is observed on a piece of ground glass on the U-V plane. The light intensity, or the Fourier power spectrum at the U-V plane is

$$I(u, v) = \frac{1}{(\lambda L)^2} \left| \int_{-\infty}^{\infty} \int_{-\infty}^{\infty} P(x, y) h(x, y) \exp(i \frac{2\pi}{\lambda} (1 + \cos \alpha)) \exp(-i \frac{2\pi}{\lambda L} (ux + vy)) dx dy \right|^2 \quad (2.2)$$

where $P(x, y)$ is the complex field incident on the surface, $h(x, y)$ is the surface height variation, λ is the wavelength of the incident light, L is the normal distance between X-Y plane and U-V plane, α is the angle formed by the incident light and surface normal. The intensity distribution is a function of, among other factors, the surface height variation $h(x, y)$. Fatigue and corrosion processes roughen the surface of a specimen resulting in a change of the surface height $h(x, y)$, and hence alters its corresponding speckle pattern, or speckle halo. Fig.2.3 is a speckle pattern of aluminum surface roughened by fatigue.

2.3.2 Evaluation of Spectrum

Before the evaluation of the surface damage a speckle pattern is smoothed by the following procedures. First, the centroid of the speckle pattern is determined by a moment method using the following equations:

$$i_c = \frac{\sum_{i=1}^M \sum_{j=1}^N g(i, j) \times i}{\sum_{i=1}^M \sum_{j=1}^N g(i, j)}, \quad j_c = \frac{\sum_{i=1}^M \sum_{j=1}^N g(i, j) \times j}{\sum_{i=1}^M \sum_{j=1}^N g(i, j)} \quad (2.3)$$

where $g(i, j)$ is the digitized intensity levels of the speckle pattern and the (i_c, j_c) is the position of the centroid of a pattern. M and N are the total discrete points in the i (horizontal) and j (vertical) directions ($M=512$, $N=480$), respectively.

Second, the spatial intensity is averaged by:

$$G(r_i) = \frac{1}{n_i} \sum_{r_i=1}^{n_i} g(i, j) \quad (i=1, 2, \dots, M \text{ and } j=1, 2, \dots, N) \quad (2.4)$$

where $r_i = \sqrt{((i-i_c)^2 + (j-j_c)^2)}$, and n_i is the total number of points within the ring $i-1 < r_i < i$.

To quantify the information brought in laser speckle pattern, two kinds of correlation coefficients are used in this study. One is an auto-correlation coefficient to quantify the

single diffraction pattern and the other is the cross correlation coefficient to calculate the degree of correlation between two diffraction patterns from surfaces.

Auto-correlation involves only one function and the auto-correlation coefficient C_a for smoothed function $G(i)$ is defined as (Rosenfeld, 1982):

$$C_a(\tau) = \frac{\sum_{i=1}^N G(i) \times G(i + \tau)}{\sum_{i=1}^N G^2(i)} \quad (2.5)$$

where $G(i)$ is the smoothed discrete light intensity at point (i) of an image. τ is the distance shifted along the i direction. When C_a is $1/e$, the particular τ is considered as the lag length. The lag length increases as the spread of a scattered field increases due to the corrosion and fatigue processes.

Cross correlation coefficient is a measure of the degree of similarity between two different objects. The coefficient of cross correlation of two arbitrary functions $g(i,j)$ and $f(i,j)$ is defined as (Rosenfeld, 1982)

$$C_{gf} = \frac{\sum_{i=1}^{i=M} \sum_{j=1}^{j=N} g(i,j) \times f(i,j)}{\sqrt{\sum_{i=1}^{i=M} \sum_{j=1}^{j=N} g^2(i,j) \times \sum_{i=1}^{i=M} \sum_{j=1}^{j=N} f^2(i,j)}} \quad (2.6)$$

where $g(i,j)$, $f(i,j)$ are discrete light intensity levels at point (i, j) of images g and f , respectively. The values of C_{gf} range between 0 and 1. If $C_{gf}=1$, patterns $g(i,j)$ and $f(i,j)$ are exactly the same, and the bigger the difference between the two images, the smaller the correlation coefficient.

3. Influence of Corrosion on the Fatigue Process of Aluminum Alloy

3.1 Introduction

As described in the preceded chapter, fatigue leads to changes in surface roughness, crack initiation and final fracture by damage accumulation. In the case of metals in corrosive environments, fatigue cracks initiate on the surfaces roughened by corrosion (Du & Chiang et al. 1995, 1998a, Kawahara et al, 1988, Doyle et al, 1990). Crack initiation depends on many surface features, such as the presence of pits or crevices, surface finish, intrusions and extrusions. The mechanism of environmental degradation of stressed metals in the presence of chloride ions is a multi variety process. It has at least relied on one or more of the following (Duquette, 1977): (1) stress concentration at the base of pits created by the corrosive medium, (2) electrochemical attack at plastically deformed areas of metal with non-deformed areas acting as cathodes, (3) electrochemical attack at ruptures on an otherwise protective surface film, and (4) lowering of surface energy of the metal due to environmental adsorption and increased propagation of microcracks. The influence of corrosive environments on fatigue has typically been studied considering the interaction between environment and fatigue behavior. However, little work has been done on fatigue crack initiation and propagation in aged or corroded aircraft structures (Koch, 1990).

Aluminum alloys are subject to different forms of localized corrosion depending on microstructure, heat treatment, grain orientation and applied stress. One of the most common forms of localized corrosion is pitting corrosion (especially in the presence of chloride ions), which is believed to be caused by the localized breakdown of the passive film. Pits can act as fatigue crack initiation sites by generating stress concentrations. They are also known to create and harbor acidic environment inside every pit (Koch, 1990). To cause pitting, an anion such as chloride must, in turn: (1) adsorb at the oxide/solution interface, (2) penetrate or dissolve through the oxide film, and (3) react locally with the

underlying alloy. As the passive film on aluminum alloys is amorphous, pitting is the active dissolution of the bare metal sites in the micro-fissures (Richardson and Wood, 1977). The exact sites of micro-fissures in passive films depend randomly on the prevailing conditions such as the purity of the metal, its microstructure and surface preparation and composition of the electrolyte.

It is important to be able to detect the extent of corrosion and fatigue damage, either in a service application or in laboratory test specimens. Both visual inspection and more elaborate methods of non-destructive inspection are available for examination of the metal surface. The former includes the microscopic and metallographic examination; the latter includes radiographic, electromagnetic and acoustic examination. Most of the methods were developed to detect cracks or flaws in metals. None of these non-destructive test methods provide satisfactory detailed information about the surface morphological changes associated with corrosion and fatigue degradation.

The Laser Speckle Sensor (LSS) technique is used in this investigation to detect the damage caused by corrosion and fatigue processes. The fundamental question raised here is: What is the influence of the surface damage caused by prior corrosion on the fatigue properties of aircraft materials? The surface roughness has been considered as a contributing factor in this work.

3.2 Specimen and Experiment

The specimens were made of Al 2024-T3 sheet with the yield strength 320MPa. The specimen was cut with a continuous radius between the ends as shown in Fig.3.1(a). The geometry was so designed that we could be reasonably certain that a fatigue crack would initiate near the center region of the specimen, where the technique of Laser Speckle Sensor (LSS) was used to monitor the aging process. The size of the specimen was constrained by the need to examine the specimen for surface analysis.

A large part of the sample was covered with commercially available epoxy so as to form a protective barrier and rendering the sample passive to corrosive solution. Illustration of the regions protected is shown in Fig.3.1(b). Samples were in 3.5 W% NaCl and 10 V% H₂O₂ solution for a varying period of time to observe the exposure time effect on the surface roughness. After suitable hours of exposure to the solution, the

samples were removed from the solution and were transferred to the fatigue-testing machine for the study of the fatigue behavior. The fatigue tests were carried out under constant-load-amplitude sinusoidal waveform loading in the frequency of 9 Hz and a load ratio R of 0.2.

Both corrosion and fatigue cause non-uniform surface roughness. It is necessary to scan the surface of interest by a laser beam to get the statistical profile. To ensure the laser beam illuminated the same location each scan, a computer controlled 3-D stage was used to locate the laser beam positions. 3×3 matrix-like scanning points in the interested area were monitored during the fatigue test as shown in Fig.3.1(b).

3.3 Results and Discussion

Fig.3.2 shows three typical SEM images of a virgin sample, a corroded sample and a subsequent fatigue sample. The rolling direction in the horizontal direction is clearly seen from Fig.3.2(a). In Fig.3.2(b), the surface is significantly roughened by pitting. The linkage of pits and pit coalescing around voids are also observed, which means the corrosion is non-uniform or irregular on the specimen surface due to localized attack of the passive film. The corrosion pits are distributed along the rolling line. It is noticed that pits coalesce along the rolling direction. Coalescing pits may become a crack if the loading direction is perpendicular to this direction. This should be avoided in practical application. Fig 3.2(c) shows the fatigue damage of the corroded sample, where in the vicinity of the crack, the surface is roughened.

A typical result from the LSS monitoring system is shown in Fig.3.3(a), (b), depicting patterns of speckle halos before and after 24 hour corrosion in the solution. The speckle patterns spread out horizontally with respect to the vertical rolling direction. Fig.3.3(c), (d) and (e) show a series of halos change with different position of fatigued specimen, from left to right the distance of the illuminated point from crack tip is 10, 5 and 0 mm. It should be noted that in the micro-scale view, corrosion damage (such as pits, transgranular corrosion) fatigue damage (such as extrusions/intrusions, voids, and microcracks) are local, while in the macro-scale view, they (especially fatigue process) manifest isotropically. This leads to more spherical halos as the roughness increases.

The surface roughness change can be monitored during the whole procedure of fatigue test of corroded specimens by illuminating the laser beam at different points where the cracks are likely to initiate and propagate. The cross-correlation coefficient as a function of the fatigue cycle is shown in Fig.3.4. The square corresponds to the laser beam point 1 where cracks could initiate and propagate. The circle corresponding to the laser beam point 2 refers to the center of the sample, the triangle to the point 3 near the farther edge, respectively. Please refer to Fig.3.1 for the laser beam scanning positions. The variation of the cross-correlation coefficient indicates the change of surface roughness. The curve with square shows that the surface exhibits a precipitous change with increasing fatigue cycle (region I, approximately below the cycles of 10,000). This is followed by a region of material damage (region II, approximately between 10,000 to 90,000) in which the surface roughness change rate is essentially independent of the fatigue cycles. As the surface roughness approach the critical point of the material (region III, from approximate 90,000 to last), there is a drastic change in the surface roughness according to the steep drop in the cross-correlation coefficient. It implies that surface roughness change will cause the crack initiation, and once the crack initiates, it in return causes more surface roughness changes. The triangle (beam point 3, crack free surface) curve shows that the surface roughness change is smaller than the point 1 where the crack initiates later. The surface roughness change at center is lower than that at edges of sample at region I and II, as there are some stress concentration near the sample edges. The cross-correlation coefficient at the point 2 falls off faster than the point 3 in region III because of the fact that crack tip almost reaches the center of the sample.

Fig.3.5 shows the relationship between the fatigue life and period of exposure leading to corrosion. During the fatigue test, cracks will easily form at pits, where the strain is higher. In the mechanical viewpoint, pits are stress raiser and considered to be the semi-elliptical surface cracks or other surface flaws. The linking of corrosion pits might provide the initiation sites for the fatigue process. In Fig.3.6 a crack is observed to initiate and propagate from the damage site in the coalesced corrosion pits corner.

3.4 Conclusions

1. Pits can be considered as crack initiators due to the stress concentration during the fatigue process.
2. Surface roughening causes the crack initiation, and the crack growth leads to further changes in surface roughness.
3. SEM images show that pits tend to coalesce along the rolling direction. Loading perpendicular to the rolling direction should be avoided because the coalesced pits may act as a crack.
4. Subsequent fatigue life is strongly dependent on the exposure time for Al 2024-T3.

4. Effect of the Initial Fatigue Cycles on the Behavior of Corrosion-Fatigue

4.1 Introduction

When an aircraft is in flight, cyclic loading is at its maximum, while corrosive process due to moisture and/or temperature is minimal. When the aircraft is on the ground, the corrosive process is at its maximum and there is little or no cyclic loading at play. Fatigue and corrosion thus repeats cyclically. We present some results on the aging process of Al 2024-T3, first subject to fatigue and then to corrosion and then to fatigue again. The results are compared to those subject to fatigue alone and those subject to corrosion first and fatigue afterwards. Interesting synergistic phenomena are observed.

4.2 Experimental Procedure

The specimens were made of Al 2024-T3 with a yield strength $\sigma_y=320$ MPa. The size and geometry of the specimens are the same as shown in Fig.3.1. The geometry was so designed that we could be reasonably certain that a fatigue crack would initiate near the center region of the specimen, where the technique of LSS was being used to monitor the damage process. The size of the specimen was constrained by the need to examine the specimen for surface analysis.

The specimen was first fatigued (under a tension-tension cyclic load of sinusoidal form with a frequency of 9 Hz and load ratio $R=0.2$, maximum stress of 200 MPa) to various degrees of damage at different fatigue cycles. Then it was dismantled from the testing machine. A large part of the specimen was covered with a layer of epoxy thus rendering the sample passive to the corrosive solution. Illustration of the protected regions is shown in Fig.3.1(b). The sample was then immersed in a corrosive solution of 3.5 wt% NaCl and 10 v% H_2O_2 for a period of 48 hours. Afterwards it was taken out from the solution

and the protective coat of epoxy was peeled off and the specimen washed in distilled water. Finally it was further cyclically loaded in air to failure.

4.3 Damage Caused by Fatigue and Corrosion

In the early stage of the fatigue process, the localization of plastic deformation due to cyclic loading results in intrusion and extrusion of the lattice plane and creates micro-voids and micro-cracks. Fig.4.1(a) shows a typical fatigue damaged Al 2024-T3 specimen after 150,000 cycles of loading. It is seen that the micro-damage manifest in the form of micro-cracks, voids, extrusion and intrusion planes. From a global viewpoint the damage appears to be randomly oriented, resulting in a macroscopically isotropic roughness change.

Pitting attack is most prevalent when aluminum alloys are exposed to solutions containing chloride ions, causing by the localized breakdown of the passive film. Since the native oxide film on the aluminum alloy is amorphous, pitting is the active dissolution of the bare metal sites in the micro-fissures and defects of the oxide film covering the alloy (Richardson & Wood, 1970). Pits sometimes are isolated but often clustered together to form a roughened surface. They act as stress raisers facilitating the initiation of fatigue cracks. On the other hand, the surface defects created by fatigue are the favorite sites of corrosion attack (Wood et al, 1974). Indeed, such an evidence is shown in Fig. 4.1, where (b) depicts the damage sites after the specimen was fatigued to 150,000 cycles and then immersed in the corrosive solution for 48 hours. It is seen that the damage sites was originated from the micro-defects created by fatigue. The less the initial fatigue cycle, the smaller and more superficial were the corrosion damage as evidenced in Fig.3(c) where the picture depicts the corrosion damage of a specimen subject to a 50,000 loading cycles followed by an immersion into corrosive solution for 48 hours.

As noted before both fatigue and corrosion damage result in surface roughness change macroscopically. To demonstrate such a change, the surface roughness of three specimens were measured by a mechanical profilometer, and the results were plotted as shown in Fig.4.2. The specimens were subject to fatigue loading at 50,000, 150,000 and 200,000 cycles respectively. And they were then immersed in the same corrosive

solution for 48 hours and then fatigued again to failure. It is seen that the surface roughness gradually changes as the loading cycle increases. The sudden jumps in roughness were due to the corrosive process. However, It should be noted that the roughness value plotted here is a relative value since roughness measurement using a mechanical profilometer creates its own damage as evidenced in Fig. 4.1(c) (the vertical scratch mark to the right).

As noted before the degree of surface roughness can also be revealed by the LSS technique. A typical set of speckle patterns from the LSS monitoring system is shown in Fig.4.3, depicting speckle halos at different stages of the fatigue-corrosion-fatigue test. Fig.4.3(a) shows the speckle halo from a specimen having experienced 1,000 cycles of loading. At this stage very little damage had occurred and the horizontal spread of the halo was largely due to the rolling marks on the surface imprinted during the manufacturing process. The spread along the 30° (approximately) direction was from an existing mechanical scratch on the surface upon which the illuminating beam happened to have impinged. Fig. 4.3(b) shows the speckle halo after the specimen had experienced 50,000 cycles of loading. At this stage fatigue had set in resulting in isotropic roughening. The specimen was then dismantled and immersed in the corrosive solution for 48 hours, and the recorded resulting speckle halo is shown in Fig.4.3(c). The roughness change had progressed further. The specimen was then fatigued again, and after an additional 285,000 loading cycles later, the speckle halo was recorded again and is shown in Fig.4.3(d). It is seen that at this stage the halo is almost circular indicating roughness isotropy.

Cross correlation coefficients of the speckle halos from a typical specimen at different stages of damage are shown in Fig.4.4. The result may be divided into three regions (I, II, III, as marked in the graph). It is seen that most of the surface roughness change occurs at the first region wherein a virgin specimen fatigued up to 50,000 cycles. A sudden roughness change occurs after the 48-hour corrosive immersion. The surface texture continues to change gradually after the specimen is cyclically loaded again. After about 100,000 cycles, the rate of surface roughness change remains essentially constant. This constitutes the second region, and after that the specimen fails quickly (Region III). The different symbols in Fig. 4.4 indicate the position of points at which the laser beam

had pointed. For this specimen a dominant fatigue crack was initiated near point 3; thus the cross correlation coefficient dropped more here (denoted by triangles) than at other points.

4.4 Fatigue Life Span as a Result

How much additional fatigue life a specimen was left after it was first fatigued and then corroded? The results are shown in Fig. 4.5 where the remaining fatigue life span of the specimens was plotted against the initial loading cycles before the 48-hour corrosion process. It is interesting to note that those specimens which had experienced initial (before the corrosive immersion) fatigue loading up to about 250,000 cycles actually have a greater remaining life span than the total life span of those which were corroded first and fatigued to failure. As expected the fatigue life span of all the specimens having gone through the three-stage (fatigue-corrosion-fatigue) tests is shorter than those which are brought to failure by fatigued alone (Du et al., 1995). It appears that for a given corrosive environment, a virgin material sustains more damage than those who have already been damaged by a modest amount of fatigue loading. Of course if the initial fatigue damage is substantial, as the data at and after 250,000 initial cycles show, the additional of corrosion will reduce the remaining life span.

The total fatigue life as a function of the initial fatigue cycles was plotted as shown in Fig.4.6. The total fatigue life is defined as the sum of the initial fatigue cycles before the corrosive process and the additional fatigue cycles needed to bring it to failure after corrosive process. It is seen that the total fatigue lives of all the specimens are substantially greater than that of those which had suffered from corrosion starting at the virgin state. The total fatigue life increases with the increase of the initial fatigue cycles. And most interestingly at and after 150,000 initial fatigue cycles, the total fatigue life span is even greater than that of those which were brought to fatigue failure from the virgin state (Du et al., 1995). It seems that a modest amount of corrosion actually has a beneficial effect to the material's fatigue life. We attribute this effect to the following reasons. As noted before, at the early stage of fatigue micro-cracks, micro-voids and minute intrusion and extrusion planes are formed. They act as stress raisers if further loading is applied. However, if the material is subjected to corrosive environment at this

stage, corrosion tends to blunt the tips of micro-cracks and the sharp corners of voids, and the intrusion and extrusion interfaces. As a result stress concentration is reduced, leading to a longer fatigue life. This hypothesis seems to be borne out by the Scanning Electron Microscopy (SEM) photograph shown in Fig. 4.7. Fig.4.7(a) shows how sharp a fatigue crack can be. Fig.4.7(b) shows that an initial micro-crack due to fatigue is seen to be blunted by corrosion. Fig.4.7(c) shows that other micro-damages (such as intrusion/extrusion) of fatigue are removed or substituted by corrosion pits.

4.5 Conclusions

In this study we investigated the damage and subsequently the fatigue life of Al 2024-T3 subject to fatigue, corrosion and fatigue sequentially. A novel optical technique called LSS was used to monitor the damage in real time. We find that mechanically induced flaw such microcracks, voids, scratches and extrusion/intrusion on the metal surface are favorite sites to initiate corrosion pits.

Synergism between fatigue and corrosion gives rise to some unexpected results. We find that when Al 2024-T3 alloy is first fatigued modestly and then subject to a corrosive solution and fatigued again, the total fatigue life is greater than those specimens which have been subject to the same corrosive solution (for the same length of time) from the virgin state and then fatigued.

Surprisingly we find that when the initial fatigue cycles before corrosion exceeds more than 1/2 of the total fatigue life of virgin material, a subsequent modest corrosion actually increases the total fatigue life of the material. We attribute this to the blunting of fatigue generated micro-cracks and removal of other mechanical micro-damage such as intrusion/extrusion.

5. Synergism between Corrosion and Fatigue

If corrosion pits act as geometric stress raisers, it is expected and examined that corrosive environments which cause pitting might lower fatigue strength. If corrosion pits act as the crack tip blunters, it explains that the fatigue strength is enhanced by a modest amount of corrosion. Both conclusions are based on the assumption that corrosion and fatigue exist separately. However, in real service, environment and fatigue effects exist simultaneously. The total damage due to corrosion fatigue is usually greater than the sum of the mechanical and chemical components if each was isolated from the other. A study of simultaneous interaction between corrosion and fatigue was also conducted and it shows how much the difference the environment can make.

Aqueous sodium chloride solution is pumped into a chamber with designed flow speed. LSS monitoring system is used to monitor surface change during corrosion fatigue process. The set up is shown in Fig.5.1. The laser beam goes through the plexiglas and liquid to the specimen surface. Under cyclic loading conditions the solution embrittles the material which can accelerate the initiation of a surface crack in an initially crack-free material. The samples are the same shape and dimensions as it used to be. The surface of the sample is polished.

The results are shown in Fig.5.2. The fatigue life of simultaneous corrosion fatigue is lower than that of any other test. It should be noted that all specimens subjected to identical corrosive environment (48 hours exposure in solution of 3.5wt% sodium chloride) except simultaneous corrosion fatigue test which only lasts about 6 hours.

Thus, it may be concluded that simultaneous interaction between corrosion and fatigue drastically reduce the fatigue life.

6. The Influence of Acetone Degreasing on the Corrosion Behavior of Al 2024-T3

6.1 Introduction

Appropriate surface preparation of materials is crucial to surface science related studies and engineering applications. Surface preparation protocols are designed such that they do not alter the surface in any form. Physical or chemical changes could significantly modify the designed performance of a material. Seemingly benign organic solvents such as acetone, isopropanol and methanol are used as cleaning agents for metals, alloys and semiconductors. The American Society of Testing Materials (ASTM) recommends protocols for surface preparation of materials for various applications. An ASTM protocol E 1078-85 (ASTM, 1986) specifies that prior to any surface analyses samples must be ultrasonically rinsed in sequence, in analytical grade acetone and isopropanol.

Aluminum alloys such as Al 2024-T3 copper intermetallics provide surface sites for pitting corrosion and in turn aid therefore contribute to the overall poor corrosion resistance of the alloy (Blanc et al, 1997, Murty et al, 1975 and Tomcsanyi et al, 1989).

A comparative study of the susceptibility to corrosion of Al 2024-T3 to corrosion with prior exposure to acetone and isopropanol to that with isopropanol in a mist containing chloride ions was performed. Potentiodynamic polarizations in deaerated 0.5M NaCl was used to determine the polarization characteristics of the alloy. X-ray Photoelectron Spectroscopy (XPS) was used to determine the surface chemistry of the alloy after exposure to the mentioned organics and the chloride mist. Dissolution of aluminum and the alloying elements in the solution at various potentials during the potentiodynamic scan was scrutinized with Inductively Coupled Plasma-Atomic Emission Spectroscopy (ICP-AES).

6.2 Experimental Method

Commercially anodized aluminum alloy Al 2024-T3 as a 3.0 mm thick sheet was obtained from Davidson Aluminum & Metal Corporation, New York. The alloy had an anodic oxide layer of approximately 500 microns thick as determined by the vendor. The composition of the alloy is given in Table 6.1.

Table 6.1 : Composition (weight %) of Al 2024-T3 alloy

Al	Si	Fe	Cu	Mn	Mg	Cr	Zn	Ti
Base	0.5	0.5	4.42	0.51	1.42	0.09	0.25	0.13

Samples were cut into coupons measuring 1 cm² and washed with de-ionized water and mechanically ground with 240 grit SiC paper to remove the anodic layer. Mechanical polishing was continued with 600 grit and with progressively finer grits until a final mirror finish was obtained with 0.5 micron water-based copper-free alumina suspension.

Two batches of samples were prepared. One batch ultrasonically rinsed in acetone for 15 minutes followed by further ultrasonic rinsing in isopropanol for 15 minutes. The other batch was ultrasonically rinsed in isopropanol for 15 minutes. Samples were dried at ambient temperature and mounted onto Plexiglas™ sample holders using commercially available epoxy for potentiodynamic polarization analysis.

A foil of 99.9999% pure Al foil was obtained from Johnson Matthey Company, Massachusetts, was cut into coupons measuring 1 cm². The coupons were ultrasonically rinsed in acetone for 15 minutes and further ultrasonic rinsing in isopropanol for 15 minutes.

All electrochemical measurements were carried out in a Greene cell with a pair of platinum counter electrodes and a saturated calomel reference electrode (SCE) connected through a Luggin capillary. All test solutions were prepared using analytical grade chemicals and de-ionized water.

A VersaStat EG&G potentiostat, interfaced with a M352 data acquisition and analysis system and the Gamry CMS 100 electrochemical system controlled by the CMS 105DC system were alternatively used in certain tests. In the potentiodynamic polarization experiments a scan rate of 0.166 V/s was used and each set of polarization experiments

was performed at least four times for reproducibility. The open circuit potential stabilized after 15 minutes prior to the start of polarization. The potential was scanned from -250 mV (versus SCE) below the stable open circuit potential and the experiment terminated when breakdown occurred. The electrolyte, 0.5M NaCl was deaerated for at least two and a half hours with high purity nitrogen prior to and during polarization. Samples were held above the electrolyte all through the process of deaeration. The bubbling of the nitrogen created fine spray of the electrolyte around the sample which is referred to as a mist. All potentials were measured with respect to the SCE scale.

The Greene cell was wrapped with commercially available aluminum foil to prevent the sample from being exposed to ambient light. The samples were then polarized in deaerated 0.5M NaCl.

A Varian Liberty 150 ICP-AES spectrometer interfaced with Varian Liberty ICP-AES 2.11 data acquisition and analysis system was used for elemental analysis of the test solution. The spectrometer was calibrated to the highest sensitivity for aluminum, copper, magnesium, silicon and iron. During the course of the potentiodynamic polarization the sample rinsed with acetone and isopropanol was held at potentials; -726 mV, -635 mV, and -560 mV for about two minutes each; the sample rinsed in isopropanol at -1100 mV, -900 mV, -800 mV, -772 mV and -714 mV. In each instance after 15 seconds, 14 millilitres of the electrolyte was drawn from close proximity of the sample through a fine-tipped pipette assisted by a peristaltic pump. Details of the complete ICP-AES analysis can be found elsewhere (Moore, 1989).

All XPS measurements were performed using a V.G. Scientific CLAM II spectrometer controlled by a VGX900I data acquisition system. The base pressure of the system during analyses was around 2×10^{-9} Torr. The entrance and exit slits width for the hemispherical analyzer was set at 4 mm and a pass energy of 20 eV was used. An Al $K_{\alpha(1,2)}$ line with an energy of 1486.6 eV and 400 watts was used as the incident radiation source. The photoelectron take-off angles were measured with respect to the sample surface. The spectrometer was calibrated for the Au4f_{7/2} line at 83.8 eV and the Cu2p_{3/2} line at 932.4 eV. Charge referencing was done with respect to the carbon 1s line at 284.6 eV. The data was smoothed using the seven or nine point quadratic or cubic least square fit and peak synthesis was performed using peak fitting routine developed by Sherwood

(Sherwood, 1983). Full details of the complete XPS analysis have been outlined elsewhere (Lu et al., 1989)

Following electrochemical analysis samples were exposed to the mist of 0.5M NaCl for varying periods of time in increments of 30 minutes. The resulting surface was observed and photographed under an Olympus BH-2 binocular microscope which was interfaced with a Javelin CCD camera and computer. Subsequently, the sample surfaces were analyzed using XPS.

6.3 Results and Discussion

6.3.1 XPS Results

To support these electrochemical results, the samples with and without the yellowish brown film were analyzed using XPS. The analyses were performed at a take-off angle of 30 degrees with respect to the sample surface to enhance surface sensitivity.

The sample that was rinsed with acetone and isopropanol showed three distinct species of aluminum in the Al2p spectra: an oxide (Al_2O_3 -gamma phase) with a binding energy of 73.6 eV, a hydroxide ($\text{Al}(\text{OH})_3$ -beta phase) with a binding energy of 75.6 eV and aluminum acetate with a binding energy of 77.5 eV as shown in Fig. 6.1.

Copper was observed on the sample surface that was rinsed with acetone and isopropanol. The corresponding Cu2p spectra shown in Fig. 6.2(a) shows copper chloride (CuCl), on the surface. The chemical state of copper was determined by the Cu LMM line shape. However, no copper was detected in the sample rinsed in isopropanol, as shown in Fig. 6.1(b).

6.3.2 Inductively Coupled Plasma Atomic Emission Spectroscopy

Samples were held at various potentials and the potentiodynamic plot for the two samples are shown in the Fig. 6.3 and 6.4 respectively. Results of the elemental analyses of these test solutions drawn at the specified potentials are given in Tables 6.2 and 6.3. Iron, silicon and manganese were not detected.

Table 6.2 Results of the ICP analyses for samples rinsed with isopropanol

E versus (SCE)	Aluminum	Copper	Magnesium	PH
E= -1220 mV (OCP)	Not detectable	Not detectable	Not detectable	7.01
E = -1100 mV	30.8 ppm	Not detectable	Not detectable	6.981
E = -900 mV	66.4 ppm	Not detectable	Not detectable	6.969
E = -800 mV	94.6 ppm	Not detectable	Not detectable	6.966
E = -772 mV	297.1 ppm	176.2 ppm	95.3 ppm	6.110
E = -714 mV	331.8 ppm	201.6 ppm	116.1 ppm	5.981

At the open circuit potential there was no detectable dissolution of any elements into the solution for the sample rinsed in isopropanol. This is indicative of the stability of the surface in the chloride solution with the pH being close to neutral. On increasing the potential in the anodic direction, traces of dissolved aluminum was detected throughout the passive region, along with a steady drop in the pH of the solution, probably due to hydrolysis. These results indicate that although the sample appears to be passive on a macroscopic scale, there is a small amount of surface activity and dissolution of the base metal into the solution. As the potential nears breakdown, copper and magnesium are also detected, indicative of dissolution into the solution from the intermetallic particles.

Table 6.3 Results of the ICP analyses for samples rinsed with acetone and isopropanol

E versus (SCE)	Aluminum	Copper	Magnesium	pH
E= -726 mV (OCP)	217.2 ppm	188.6 ppm	Not detectable	6.740
E = -635 mV	309.0 ppm	256.7 ppm	Not detectable	6.430
E = -560 mV	396.1 ppm	283.1 ppm	127.2 ppm	6.010

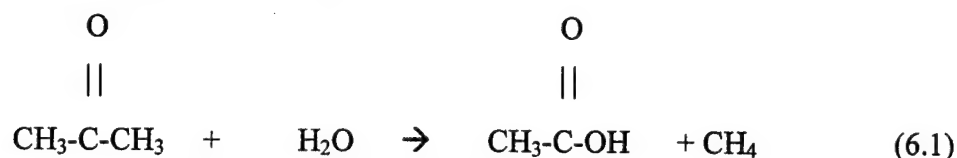
Results from the sample rinsed in acetone and isopropanol were dramatically different. At the open circuit potential aluminum (217.2 ppm) and copper (188.6 ppm) was detected indicating corrosion of second phase particles and the pH of the solution decreases. As the potentials were swept in the anodic direction the amount of dissolution of both

aluminum and copper increased, while magnesium could only be detected at potentials higher than -560 mV (versus SCE). These results confirm the presence of copper on the surface of the alloy due to the exposure to acetone and a chloride ions, similar to the XPS observations of the yellowish brown film.

6.4 Mechanism

6.4.1 Formation of Copper chloride

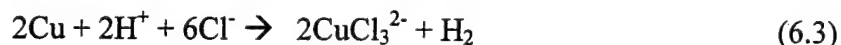
Ultrasonic cleaning of the sample in acetone and isopropanol, leaves traces of acetone on the surface of the sample. In the presence of water vapor, acetone decomposes to acetic acid and methane (Lee et al, 1975),



Copper is photosensitive and hence is activated by light. In the presence of light copper in the aluminum-copper intermetallic is activated and reacts with acetic acid to form copper acetate. Copper acetate which is relatively unstable in the presence of Al^{3+} ions dissolving from the intermetallic particle and the interface with the matrix reacts to form aluminum acetate.



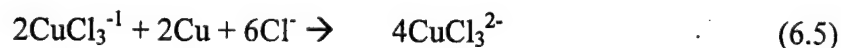
According to Davis and Johnson (1978) in the presence of chlorides



A photo-oxidation reaction takes place, where the copper complex reacts according to



which is followed by a reproporationation reaction wherein Cu (II) goes to the stable Cu(I),



Copper chloride is yellowish brown in color which is found on the surface of the alloy that was rinsed in acetone and isopropanol.

6.4.2 Timed exposure of the alloy to 0.5M NaCl

The optical micrographs of the sample surfaces that were exposed for varying lengths of time are shown in Fig. 6.5(a) through (d). The surface of the samples does not show any marked morphological changes for the initial 60 minutes. However, pitting is observed in samples that have been exposed to the mist for 90 minutes or more as shown in Fig.6.5(b). Samples exposed for 120 and 150 minutes show areas that are light reddish in color suggesting the presence of copper, as seen in Fig.6.5(c) and (d).

The XPS data showed the presence of copper in the 1+ chemical state in samples that were exposed to the mist for 90 minutes or longer. The Al2p and Cu2p photoelectron spectra from samples exposed to the mist for different periods of time are shown through Fig.6.6 and Fig. 6.10. Copper is detected on the sample surface for samples that have shown surface morphological changes, in our case samples exposed for 90 minutes or greater. This is also accompanied by the presence of aluminum acetate. The relevant Al2p and Cu2p spectra are shown in Fig. 6.8, 6.9, and 6.10.

6.5 Conclusions

Acetone changes the surface of the alloy (Al 2024-T3) and in turn the corrosion characteristics. Copper being photosensitive participates in surface reactions with residual acetone which has decomposes to acetic acid. In turn freely corrodes, and in the process enriches the surface in copper. Loss of copper lowers the corrosion resistance of the alloy. Hence it is recommended that copper bearing alloys should not be treated with acetone.

REFERENCES

- ASTM Standards on Surface Analysis, Publisher: ASTM, 1916, Race St., Philadelphia, PA 19103, p. 48, (1986).
- Blanc, C., Lavelle, B., and Mankowski, *Corrosion Sci.*, Vol. 39, pp. 495, (1997).
- Chiang, F.P., 1978, "A New Family of 2D and 3D Experimental Stress Analysis Techniques Using Laser Speckles," *SM Archives*, Vol.3, pp27-58.
- Chiang, F.P. Du, M.L., and Li, S., 1995, "Early Stages of Fatigue Damage of Fastener Hoes Monitored by Laser Speckle," *Structural Integrity of Fasteners, ASTM STP 1236*, P.M.Toor, Eds, American Society for Testing and Materials, Philadelphia, pp.143-154.
- Chubb, J. P., Morad, T. A., Hockenhull, B. S. and Bristow, J. W., 1995, "The Effect of Exfoliation Corrosion on the Fracture and Fatigue Behavior of 7178-T6 Aluminum," *International Journal of Fatigue* , Vol.17, No.1, pp.49-54.
- Congleton, J. And Parkins, R.N., 1988, "Degradation of Mechanical Properties by Corrosion Fatigue," *Proc. Instn Mech Engrs*, Vol 203, pp.73-83.
- Dai,Y.Z., Kato, A., and Chiang, F.P., 1991, "Fatigue Monitoring by Laser Speckle," *International Journal of Fatigue*, Vol.13, pp.227-232.
- Davis, D.D. and Johnson, D.L. *J. Electrochem. Soc.*, p. 1889, (1978).
- Doyle, J. L., Wood, G. R., and Bondurant, D. P., May, 1990, "Using Laser-based Profilometry to Locate and Measure Corrosion Fatigue Cracking in Boiler Tubes," *Materials Evaluation*, pp.556-560
- Du, M. L., Chiang, F. P., Kagwade, S. V. and Clayton, C. R., 1995, "Effect of Corrosion on the Subsequent Fatigue Properties of Aluminum Alloy Sheet," *1995 SEM's Spring Conference* , Grand Rapids, Michigan, June 12-14.
- Du, M.L., Chiang, F.P., Kagwade, S.V. and Clayton, C.R., 1997, Influence of Corrosion on the Fatigue Properties of Aluminum Alloy Al 7075, To Appear in *Journal of Testing and Evaluation*.
- Du, M.L., Chiang, F.P., Kagwade, S.V. and Clayton, C.R., 1997, Interaction between Corrosion and Fatigue of Al 2024-T3 Alloy, Submitted to *International Journal of Fatigue*.
- Duquette, D. J., "Mechanism of Crack Initiation and Propagation in Corrosion Fatigue," *Mechanisms of Environment Sensitive Cracking of Materials: Proceedings of an*

International Conference, P. R. Swann, F. P. Ford and A. R. C. Westwood, Eds., Guildford, 1977, 305-321.

Duquette D. J. 1990, "Corrosion Fatigue Crack Initiation Processes: A State-of-the-art Review", *Environment-Induced Cracking of Metals*, NACE-10, R. P. Gangloff and M. B. Ives, Eds., National Association of Corrosion Engineers, 45-54.

Flournoy, T. H. and Seher, C. C., 1995, "Corrosion Activity in the Federal Aviation Administration's National Aging Aircraft Research Program," *Corrosion 95*, Orlando, Florida, March 26-31, pp.8/1-8/7.

Foley, R.T., *Corrosion*, 42, 277 (1986).

Hunsche, A. and Neumann, P., 1988, "Crack Nucleation Persistent Slipbands," *Basic Questions in Fatigue: Volume I, ASTM STP 924*, J. T. Fong and R. J. Fields, Eds., American Society for Testing and Materials, Philadelphia, pp.26-38 .

Kato, a., Kawamura, M., and Nakaya, I., 1995, "Damage Monitoring of Metal Materials by Laser Speckle Assisted by Image Processing Techniques," *JSME International Journal*, Series A, Vol.38, No.2, pp.249-257.

Kagwade, S.V., Clayton, C.R., Du, M.L. and Chiang, F.P., (1996) "The Effect of Acetone on The Corrosion Characteristics of Al 2024-T3 in a Mist of 0.5M NaCl", 190th Meeting of the Electrochemical Society, Oct. 6-11, San Antonio, Texas.

Kagwade, S.V., Clayton, C.R., Du, M.L., and Chiang, F.P., 1997, The Effect of Acetone on the Corrosion Characteristics of AA 2024-T3 in a Mist of 0.5M NaCl at 24°C, Submitted to Electrochemical Society (ECS), Rapid Communications.

Kawahara, M., Fujita, T., Kurihara, M., Inagaki, H., and Kitagawa, H., 1988, "Corrosion Fatigue Crack initiation of Carbon Steels in Seawater," *Basic Questions in Fatigue: Volume II, ASTM STP 924*, R.P.Wei and R.P.Gangloff, Eds., American Society for Testing and Materials, Philadelphia, pp.145-163.

Lee, J.D., *Concise Inorganic Chemistry*, 3rd Edition, ELBS, London, p. 394, (1975).

Lin, T. H., and Ito, Y. M., 1969, "Mechanics of a Fatigue Crack Initiation Mechanism," *Journal of the Mechanics and Physics of Solids*, Vol.17, pp.511-523.

Lin, T. H., Lin, S. R., and Wu, X. Q., 1990, "Micromechanics of an Extrusion in High-Cycle Fatigue With Creep," *Journal of Applied Mechanics*, Vol.517, pp.815-820.

Lu, Y.C., Clayton, C.R. and Brooks, A.B., *Corrosion Sci.*, 29, 863, (1989).

- Ma, B.T., and Laird, C., 1989b, "Overview of Fatigue Behavior in Copper Single Crystals - I. Surface Morphology and Stage I Crack Initiation Sites for Tests at Constant Strain Amplitude," *Acta Metallurgica*, Vol. 37, pp.325-336.
- Ma, B.T., and Laird, C., 1989a, "Overview of Fatigue Behavior in Copper Single Crystals - II. Population, Size, Distribution and Growth Kinetics of Stage I Cracks for Tests at Constant Strain Amplitude," *Acta Metallurgica*, Vol. 37, pp.337-348.
- May, A.N., 1960, "Dislocation Distribution and Prediction of Fatigue Damage," *Nature*, Vol. 185, No.1, pp.303-304.
- Moore, G.L, Introduction to Inductively Coupled Plasma Atomic Emission Spectrometry, Analytical Spectroscopy Library-Volume 3, Elsevier, New York, p. 3-11, (1989).
- Murty, Y.V.V.R.S. , Kattamis, T.Z., and Devereux, O.F., *Corrosion*, 31, 207, (1975).
- Piasek, R. S. and Gangloff, R. P., 1990, "Aqueous Environment Effects on Intrinsic Corrosion Fatigue Crack Propagation in an Al-Li-Cu Alloy," *Environment induced cracking of Metals*, Ed. R.P.Gangloff and M.B.Ives, National Association of Corrosion Engineers, Houston, pp.233-240.
- Pao, P.S., Gao, M., and Wei, R.P., "Critical Assessment of the Model for Transport-Controlled Fatigue Crack Growth," *Basic Questions in Fatigue: Volume II, ASTM STP 924*, R.P.Wei, and R.P.Gangloff, Eds., American Society for Testing and Materials, Philadelphia, 1988, 182-195.
- Richardson, J. A. and Wood, G. C., 1970, "A Study of Pitting in Aluminum Using Scanning Electron Microscopy," *Corrosion Science*, Vol.10, pp. 313 - 323.
- Rosenfeld, A. and Kak, C.A. *Digital Picture Processing*, Academic Press, 1982.
- Sherwood, P.M.A, Practical Surface Analysis, Briggs, D. and Seah, M.P., Eds., John Wiley and Sons , New York, New York, pg 445, (1983).
- Tomcsanyi, L., Varga, K., Bartik, I., Horayni, G., and Maleczki, E., *Electrochim. Acta*. 34, 855, (1989).
- Wood, G. C., Sutton, W. H., Richardson, J. A., Riley, T. N. K. and Malherbe, A. G., 1974, "The Mechanism of Pitting of Aluminum and Its Alloys," *Localized Corrosion*, Houston, Texas, Ed. Brown, B. F. and Stachle R. W., pp.526-539.
- Wood, W. A., 1958, "Formation of Fatigue Cracks," *Philosophical Magazine*, Vol.3, pp.692-699.

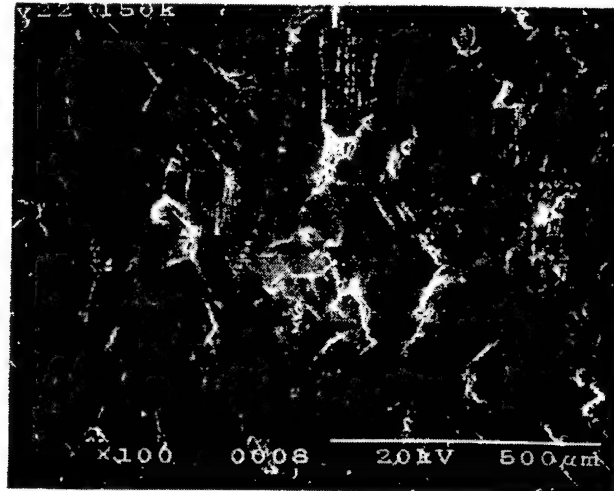


Figure 2.1 Typical SEM image showing the surface feature of a fatigued sample

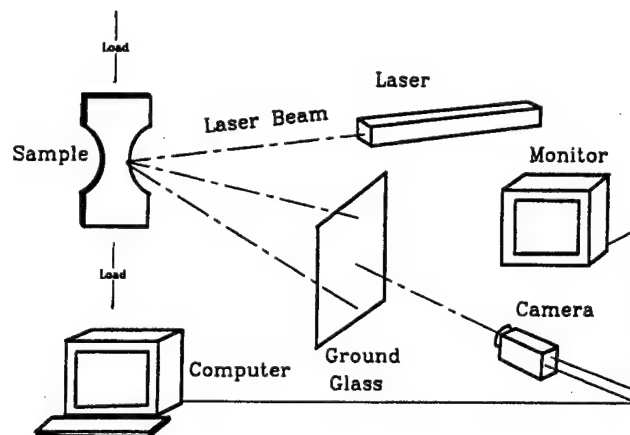


Figure 2.2 Schematic set-up of Laser Speckle Sensor technique.

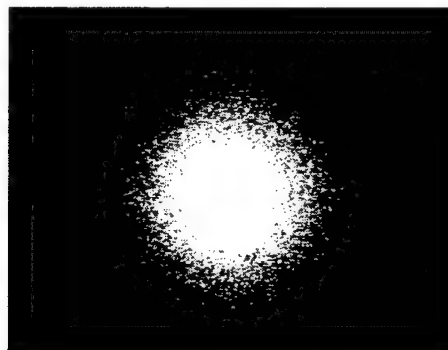


Figure 2.3 Laser speckle pattern of aluminum rough surface induced by fatigue

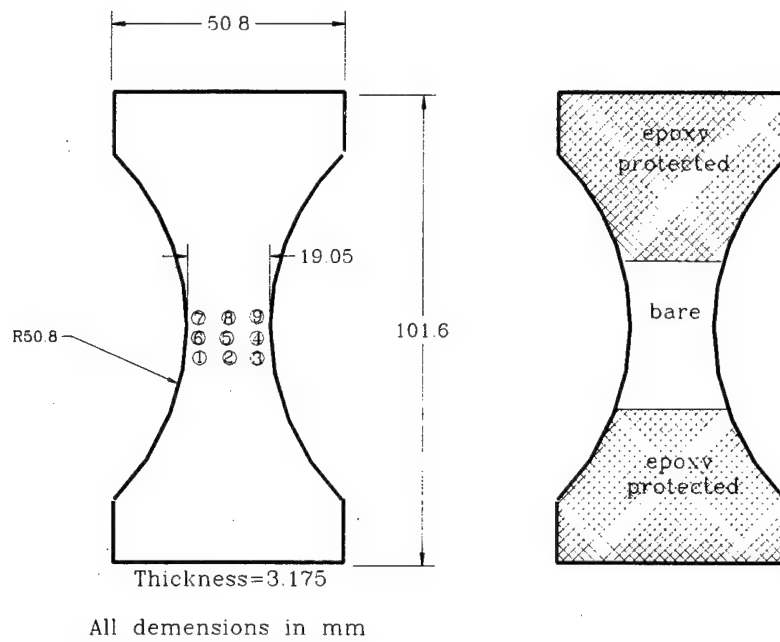


Figure 3.1 (a) Geometry of the specimens and laser beam scanning positions; (b) Epoxy coated sample. 3×3 matrix-like circle in the center of sample indicates the laser beam point position.

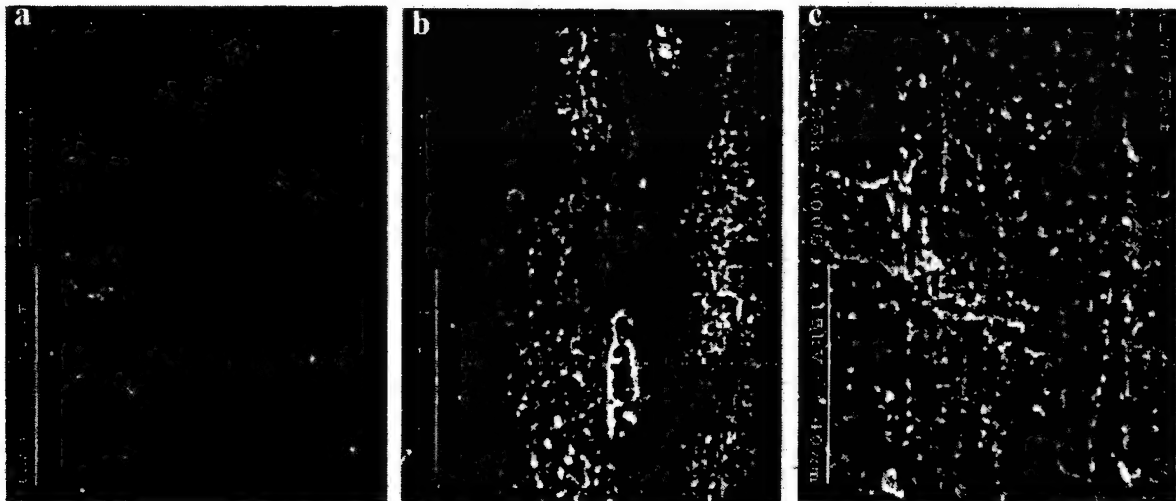


Figure 3.2 Typical SEM image showing the different surface feature of (a) as-received, (b) 24 hour corroded and (c) subsequent fatigue sample surface.

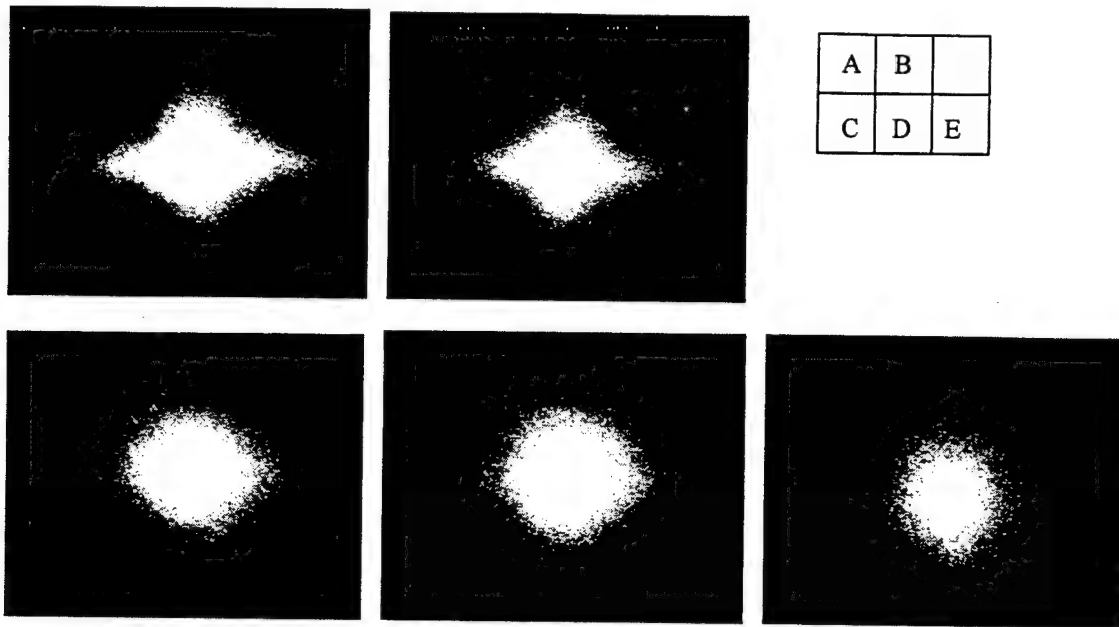


Figure 3.3 A series of speckle halos of (a) as-received surface, (b) corroded surface after 24 hours exposure in NaCl solution, (c) surface of 10 mm in front of a crack tip, (d) surface of 5 mm in front of a crack and (e) surface of 0 mm from a crack tip.

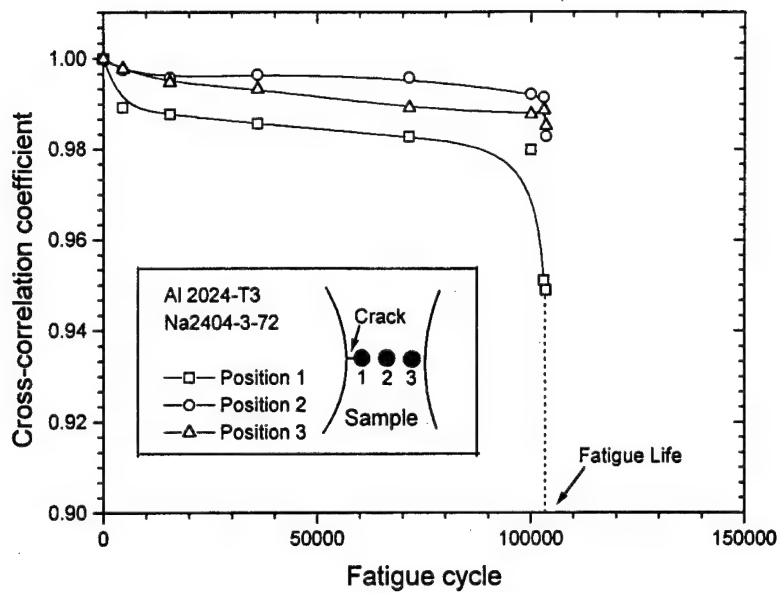


Figure 3.4 The cross-correlation coefficient as a function of number of fatigue cycles for a typical corroded Al sample.

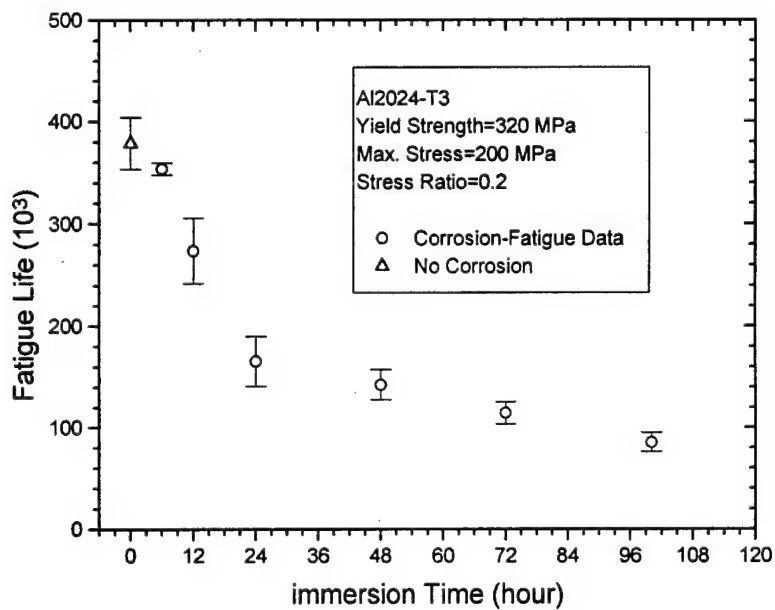


Figure 3.5 The effect of pre-existing corrosion on fatigue life of Al 2024-T3.

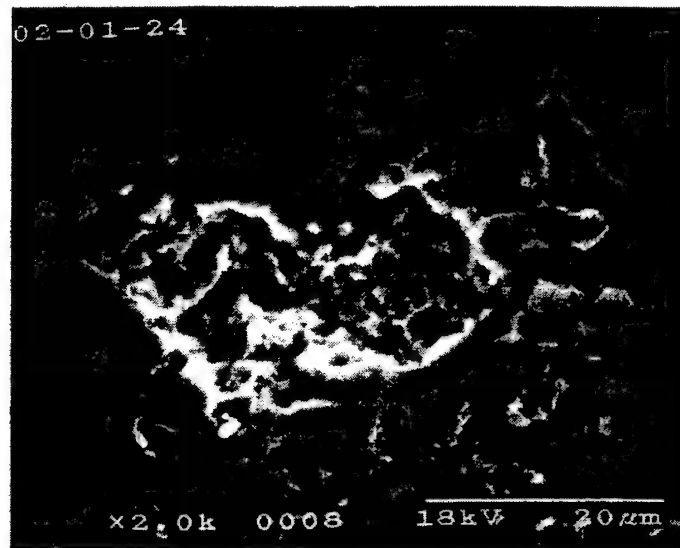


Figure 3.6 A crack initiates and propagates from the corner of pits.

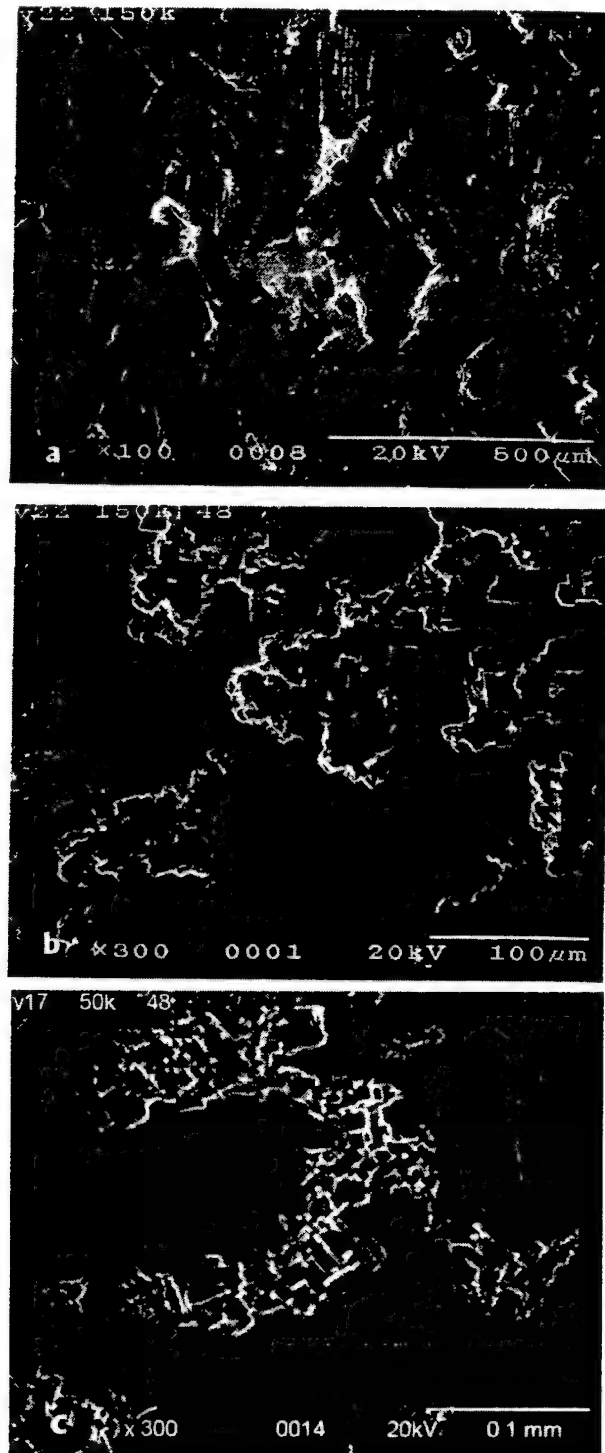


Figure 4.1 Micro-damages of Al 2024-T3 due to fatigue and corrosion. (a) after 150,000 loading cycles; (b) after 150,000 loading cycles and then 48 hours in 3.5 wt% NaCl solution; and (c) after 50,000 cycles and then 48 hours in 3.5wt% NaCl solution; vertical scratch made by mechanical profilometry.

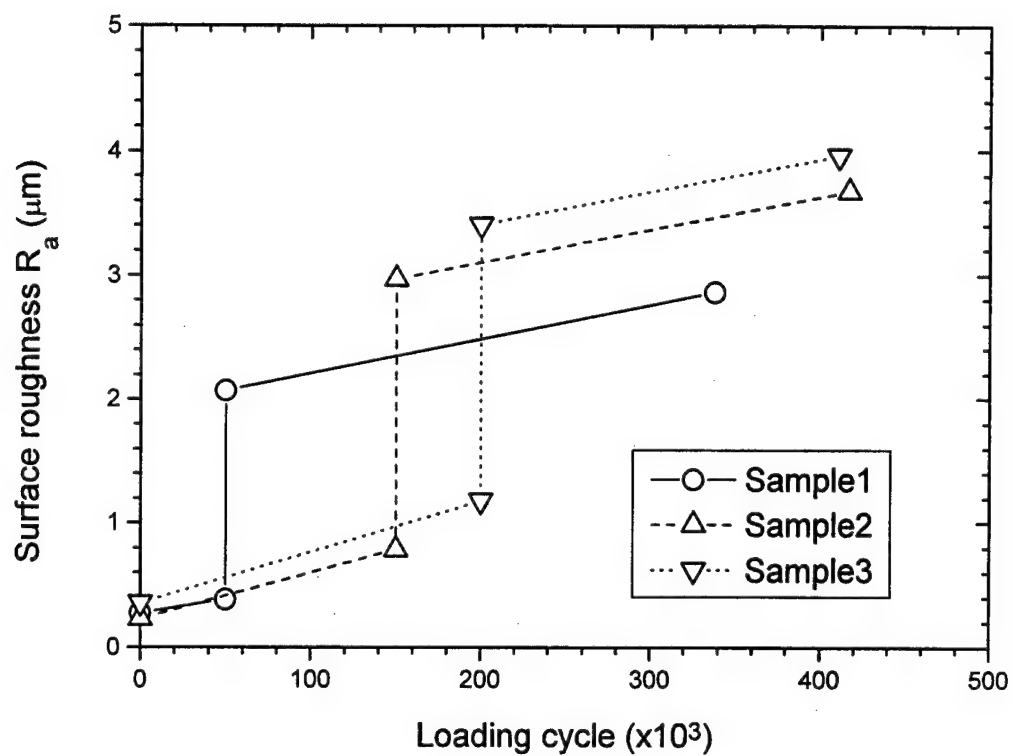


Figure 4.2 Surface roughness change (as measured by mechanical profilometer) due to fatigue, then corrosion and fatigue. Vertical jumps due to corrosion after immersion in a corrosive solution for 48 hours.

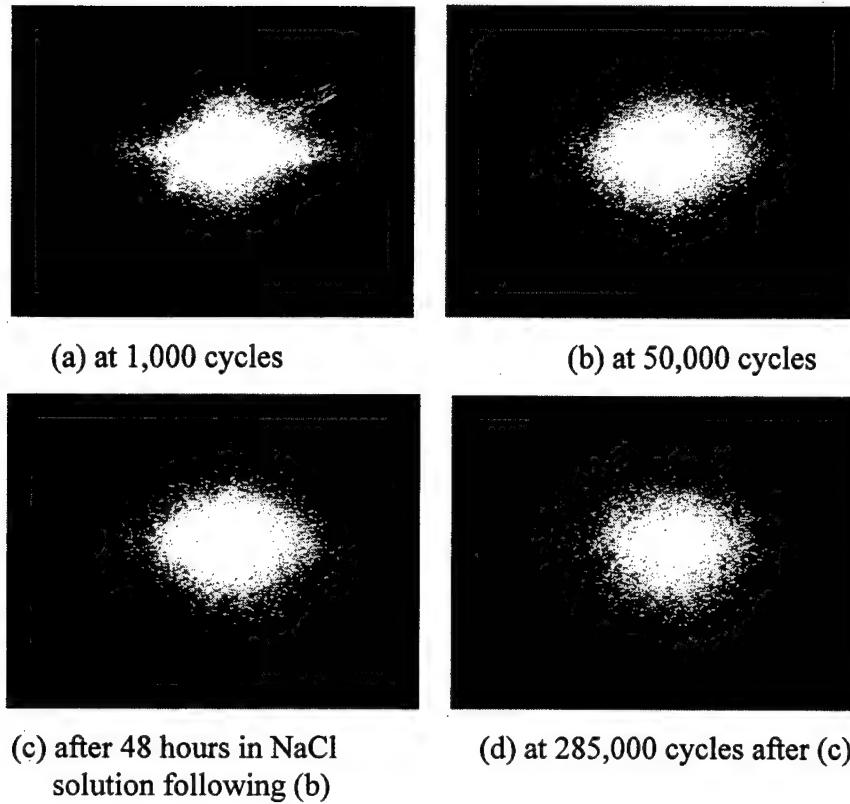


Figure 4.3 A typical series of speckle patterns from an Al2024-T3 specimen at different stage of fatigue-corrosion-fatigue test. (a) at 1,000 cycles; (b) at 50,000 cycles; (c) after 48 hours immersion in corrosive solution; (d) at 285,000 cycles after (c).

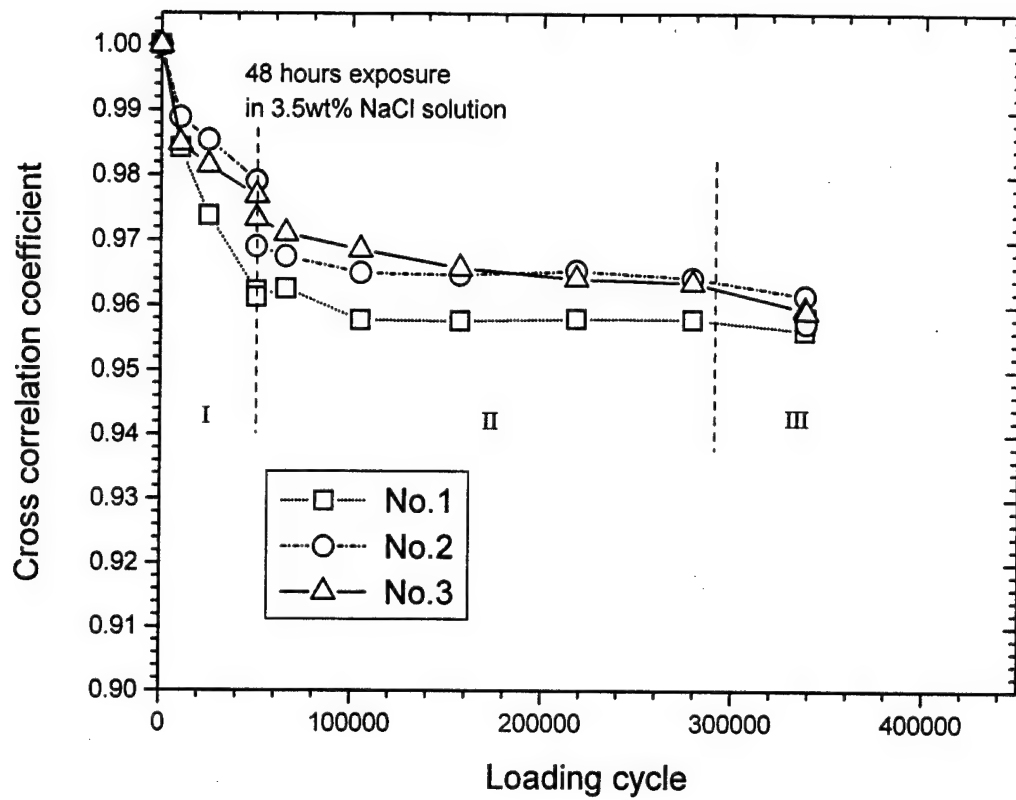


Figure 4.4 the cross-correlation coefficient of speckle patterns as a function of fatigue cycle for a typical fatigue, then fatigue and corrosion experiment test. No.1, 2 and 3 are the laser beam positions corresponding to Fig. 2(a).

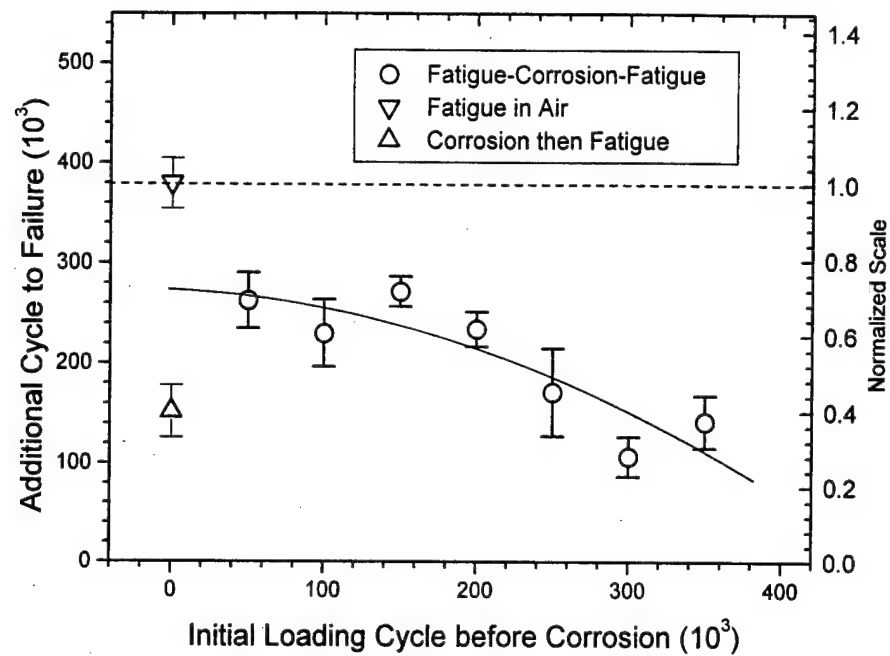


Figure 4.5 The additional cycles to failure as function of the initial loading cycles. The y-axis on the right is a scale normalized by 380,00 cycle, the fatigue life span without subject corrosion. All other samples were immersed in in 3.5wt% NaCl solution for 48 hours after the initial fatigue loading.

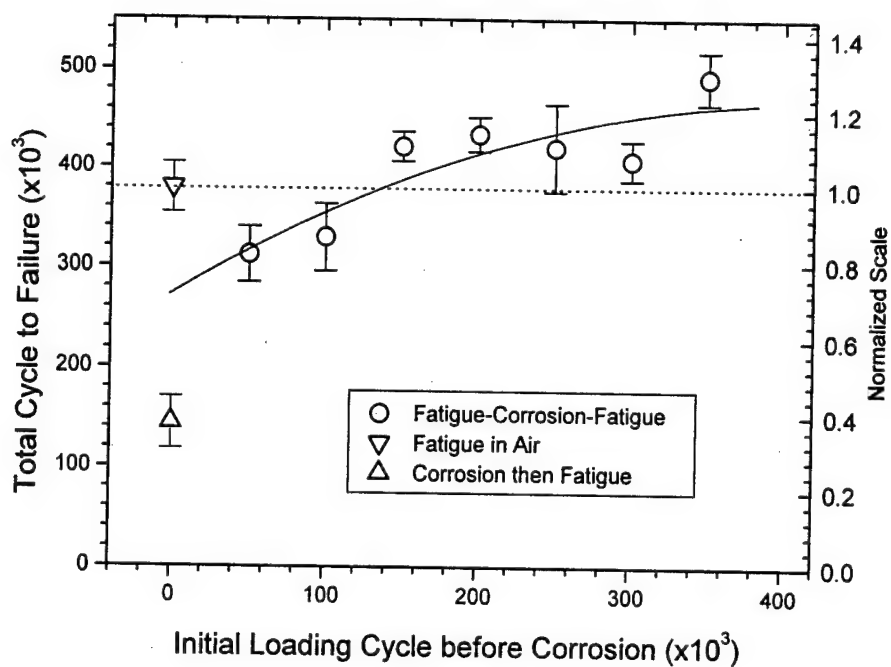


Figure 4.6 The total life of complete test as a function of the initial loading cycles. The Y-axis in the right is a scale normalized by 380,000 which is the life of fatigue without corrosion. The samples were immersed in 3.5wt% NaCl solution for 48 hours after initial fatigue loading.

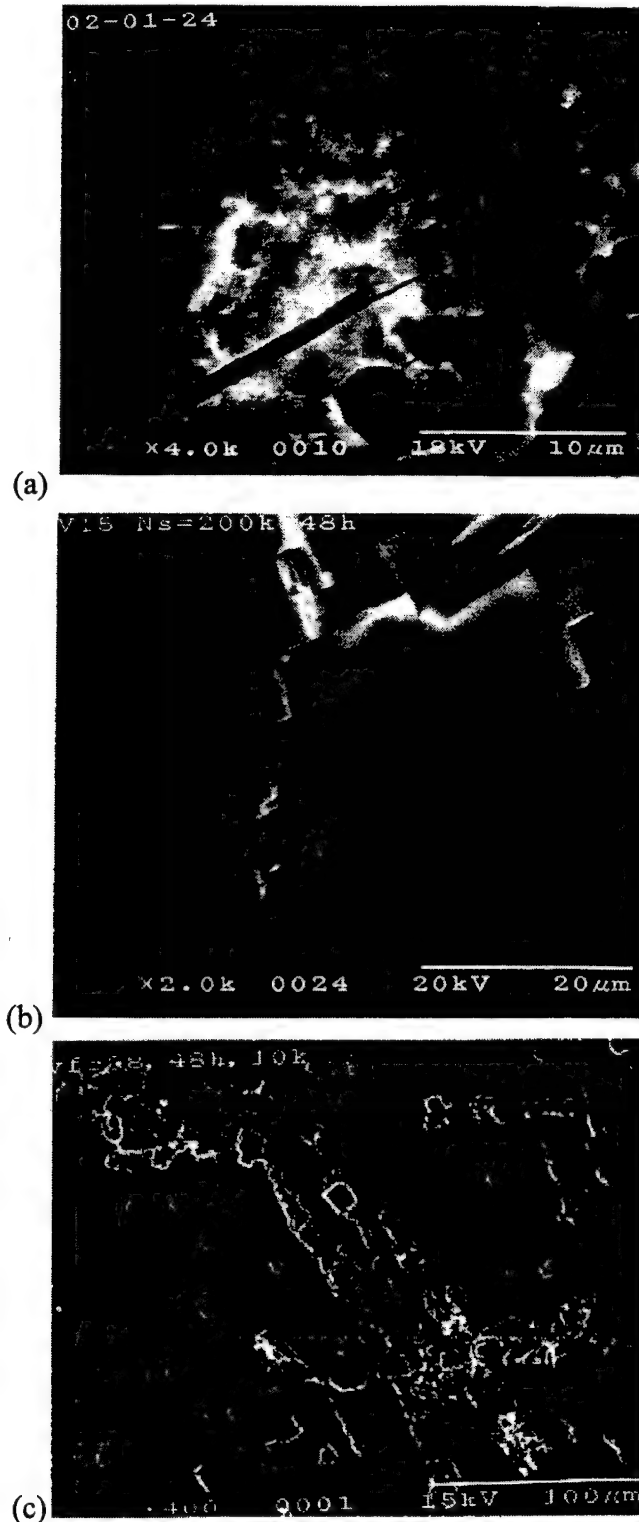


Figure 4.7 (a) a sharp micro-crack of fatigue. The picture was taken when a pre-corroded specimen was fatigued to 100,000 cycles; (b) a micro-crack blunted by pitting and (c) intrusion/extrusion removed by pitting. Pictures (b) and (c) were taken after fatigued material was exposed in the corrosive solution for 48 hours.

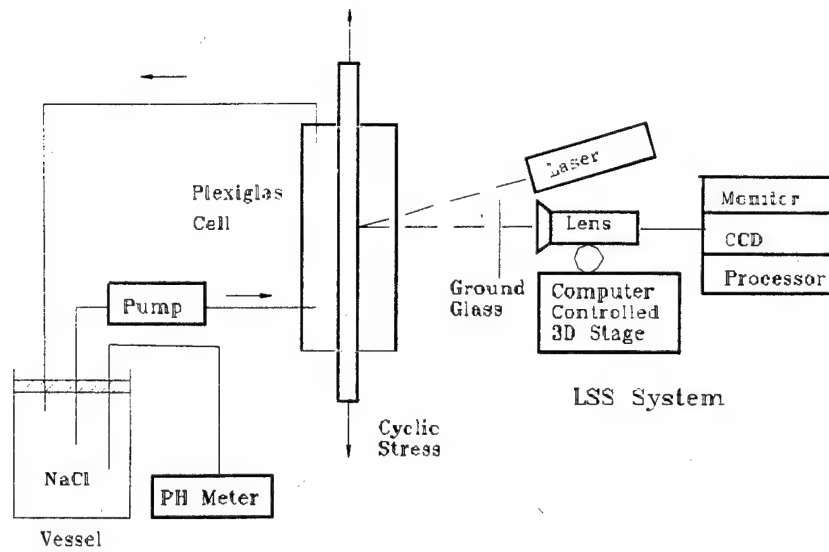


Figure 5.1 Schematic set up for corrosion fatigue in-situ monitoring

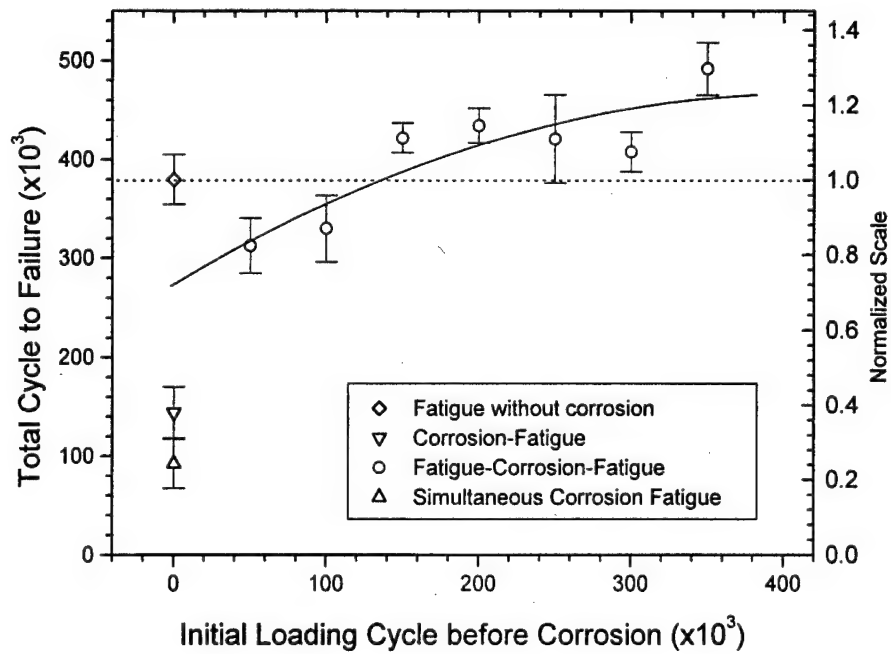


Figure 5.2 Fatigue life of simultaneous corrosion fatigue test is lower than that of any other test even though this test only lasts 6 hours.

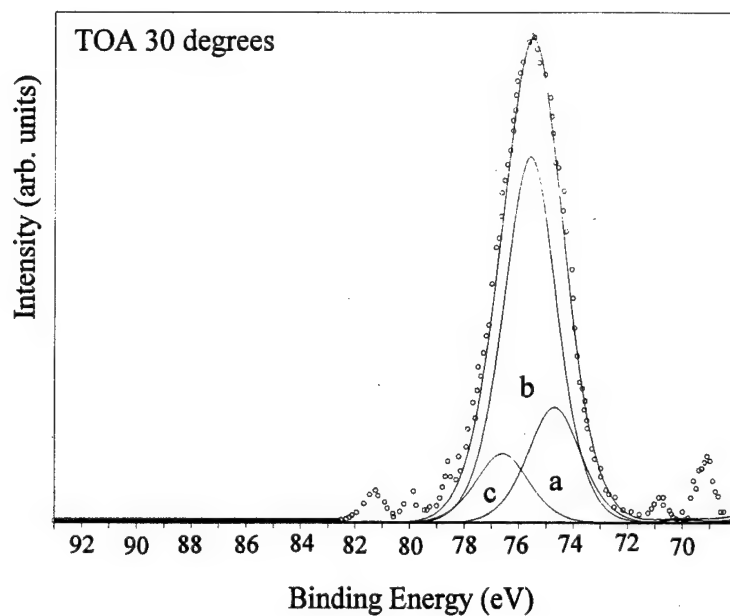


Figure 6.1 Al₂p photoelectron spectra from A1 2024-T3 exposed to acetone and isopropanol, and left in an ambient environment, and analyzed after 2.5 hours.

a = 74.6 eV, (Al₂O₃, gamma phase)

b = 75.5 eV, (Al(OH)₃)

c = 77.5 eV, (Al acetate)

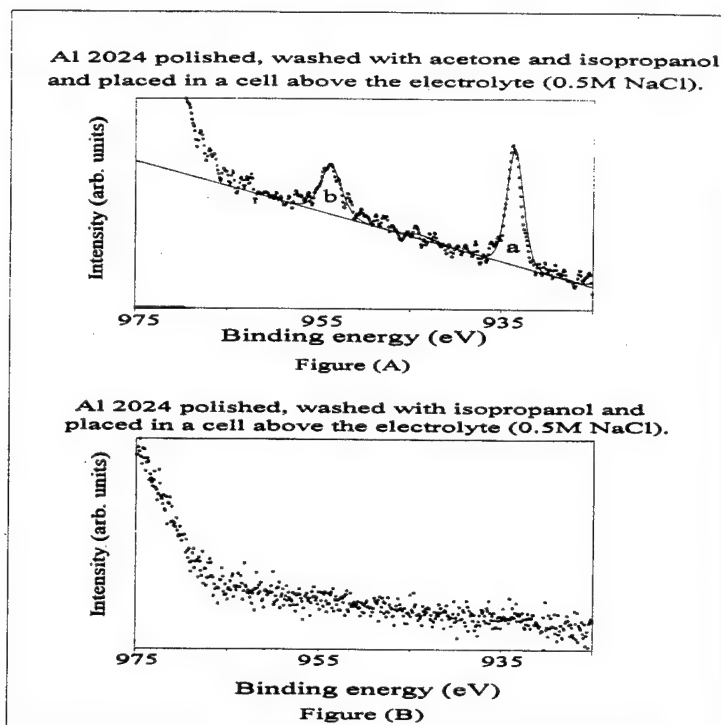


Figure 6.2 (A) & (B): Cu 2p spectra. (A): a = 933.5 eV, (CuCl)
 (B): There is no evidence of copper on the surface of the alloy.

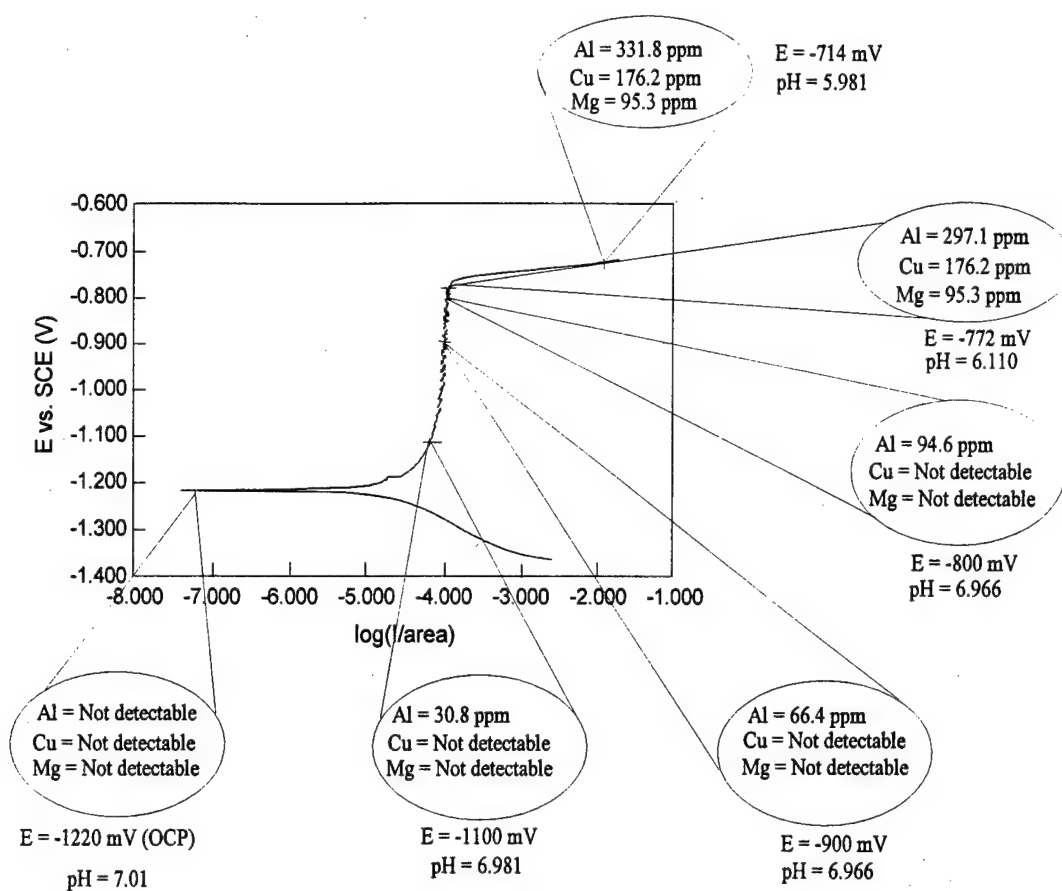


Figure 6.3 Polarization plot of Al 2024-T3 rinsed in just isopropanol showing potentials at which the electrolyte was drawn and the elemental composition obtained from ICP-AES analysis

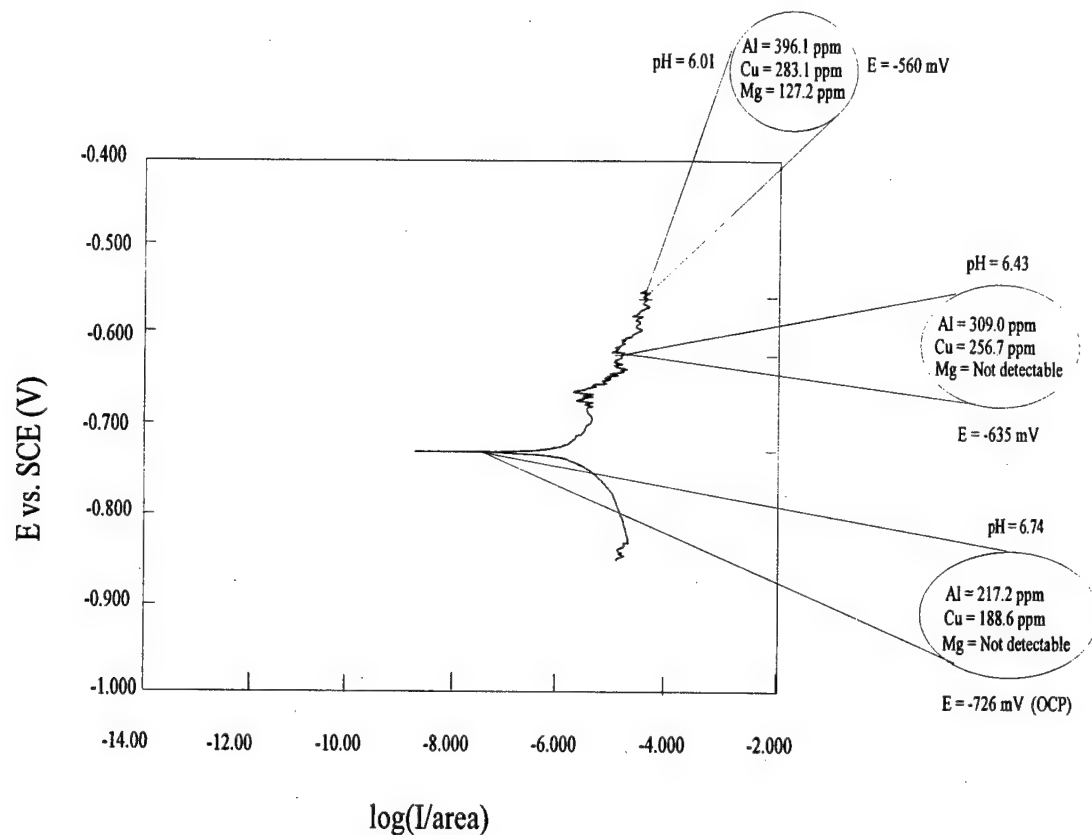


Figure 6.4 Polarization plot of Al 2024-T3 rinsed in acetone and isopropanol showing potentials at which the electrolyte was drawn and the elemental composition obtained from ICP-AES analysis.

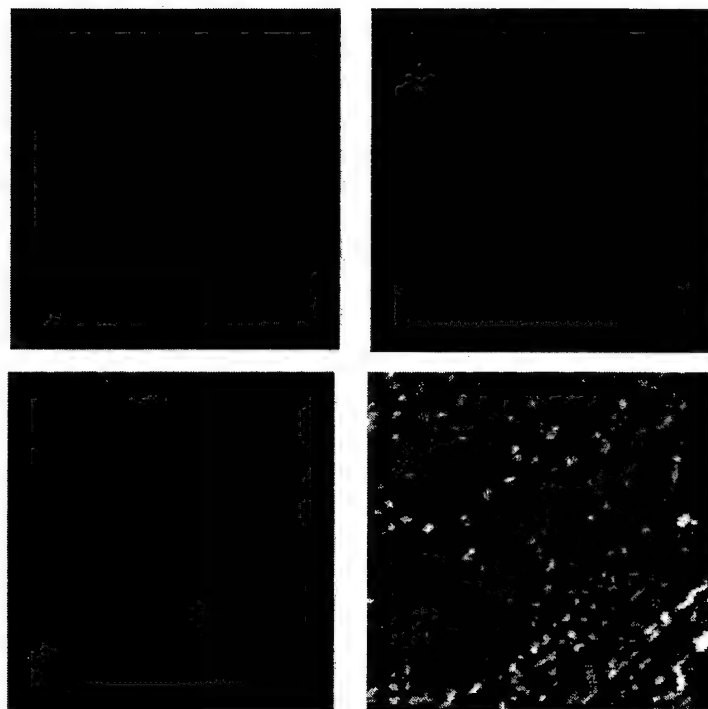


Figure 6.5 Optical micrographs of Al 2024-T3. (a) A polished coupon. (b) Rinsed in acetone and isopropanol and exposed to the mist for 90 minutes. (c) Rinsed in acetone and isopropanol and exposed to mist for 120 minutes. (d) Rinsed in acetone and isopropanol and exposed to the mist for 150 minutes.

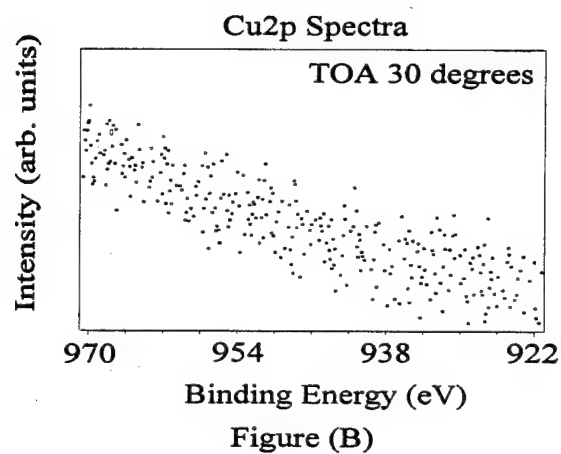
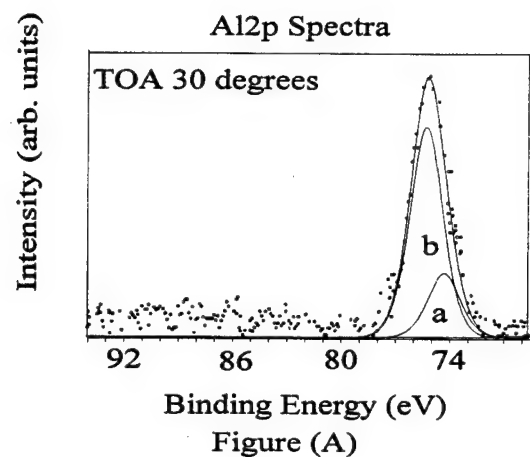


Figure 6.6 Photoelectron spectra from Al 2024-T3 exposed for 30 minutes to 0.5M NaCl. (A) Al 2p spectra: a = 74.6 eV (Al_2O_3 , gamma phase), b = 75.5 eV ($\text{Al}(\text{OH})_3$) (B) Cu2p spectra : No copper detected

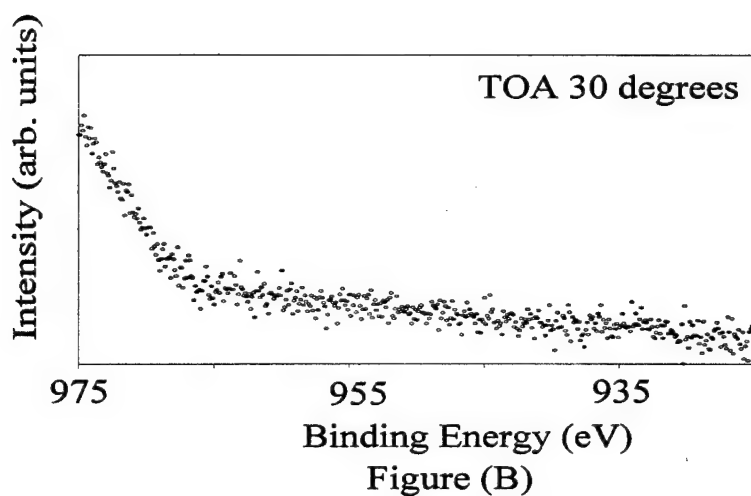
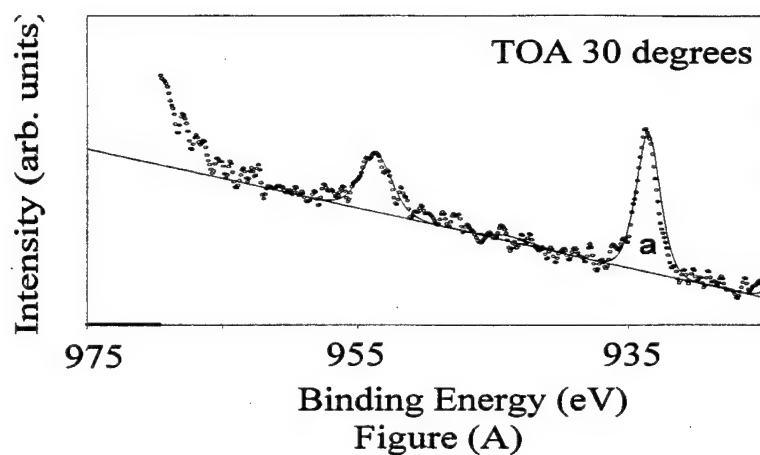


Figure 6.7 Cu₂p photoelectron spectra from Al 2024-T3. (A) Al 2024-T3 rinsed in acetone and isopropanol and held above the electrolyte (0.5M NaCl) in the Greene cell for 2.5 hours. a = 933.4 eV. (B) Al 2024-T3 rinsed in isopropanol and held above the electrolyte (0.5M NaCl) in the Greene cell for 2.5 hours. No copper was detected

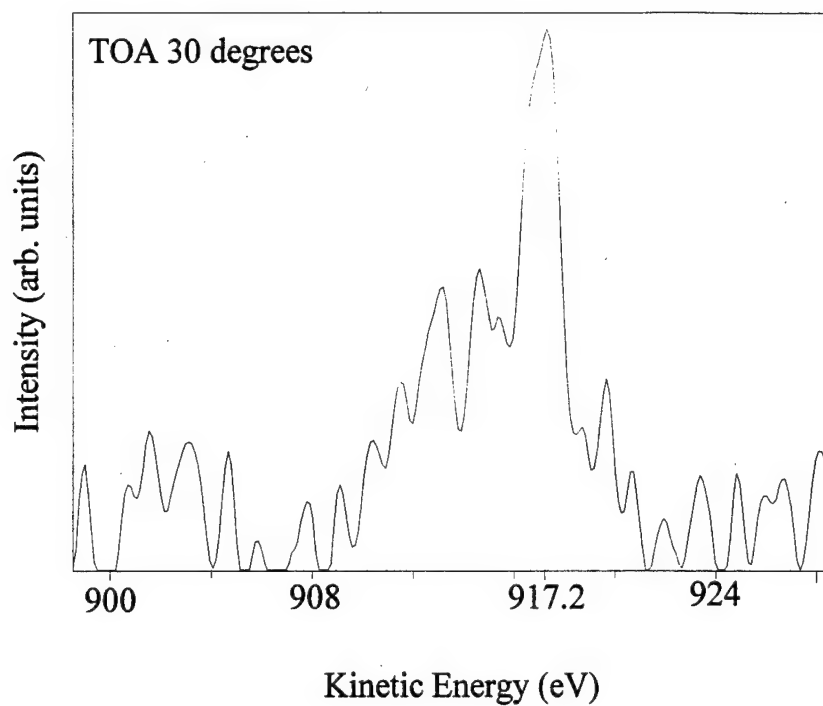


Figure 6.8 Cu LMM spectra from Al 2024-T3 rinsed in acetone and isopropanol and held above the electrolyte (0.5M NaCl) in the Greene cell for 2.5 hours. The chemical state of copper is identified as Cu(I) by the peak at 917.2 eV.

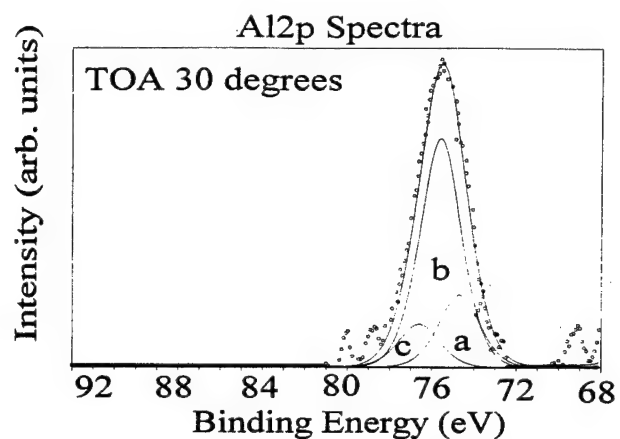


Figure (A)

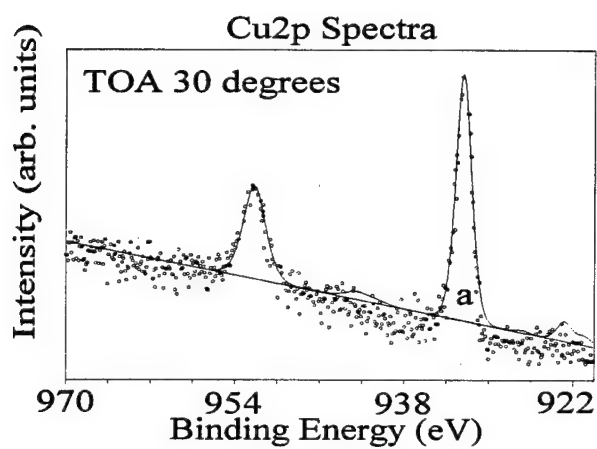


Figure (B)

Figure 6.9 Photoelectron spectra from Al 2024-T3 exposed for 120 minutes to 0.5 M NaCl. (A) Al₂p spectra : a = 74.6 eV (Al₂O₃, gamma phase). b = 75.5 eV (Al(OH)₃), c = 77.5 eV (Al-acetate). (B) Cu₂p spectra : a = 933.4 eV (CuCl)

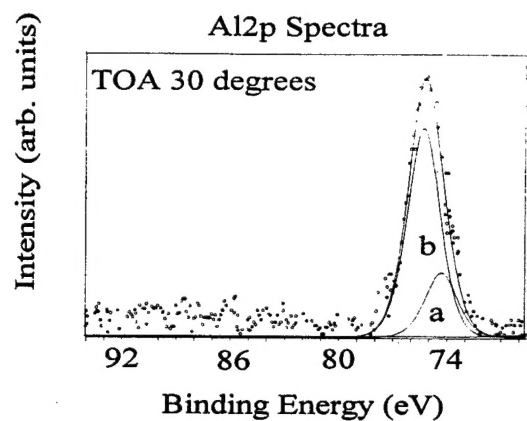


Figure (A)

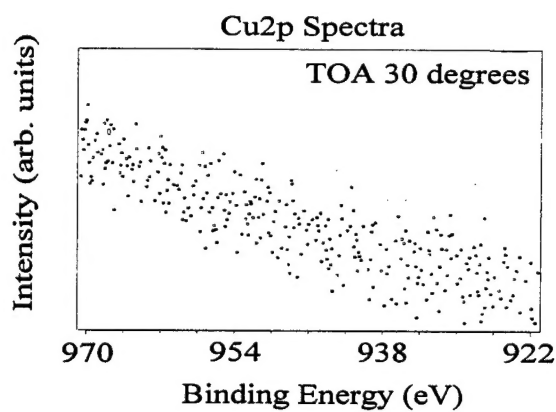


Figure (B)

Figure 6.10 Photoelectron spectra from Al 2024-T3 exposed for 30 minutes to 0.5M NaCl. (A) Al 2p spectra: a = 74.6 eV (Al_2O_3 , gamma phase), b = 75.5 eV ($\text{Al}(\text{OH})_3$). (B) Cu2p spectra : No copper detected.

Appendices

Appendix 1 List of Publications Resulting from this Project

1. F. Jin & F.P. Chiang, "ESPI and Digital Speckle Correlation Applied to Inspection of Crevice Corrosion on Aging Aircraft", *Research in NDE*, in press.
2. F. Jin & F.P. Chiang, "A New Technique Using Digital Speckle Correlation for Nondestructive Inspection of Corrosion", *Material Evaluation*, 55(7) 1997.
3. F. Jin, S.Y. Wu, and F.P. Chiang, "Quantitative Evaluation of Crevice Corrosion by TADS", The First Joint DoD/FAA/NASA Conference on Aging Aircraft, Ogden, Utah, July 8-10, 1997.
4. F. Jin, M.L. Du, and F.P. Chiang, "On Fractal Aspect of Corrosion/Fatigue", The First Joint DoD/FAA/NASA Conference on Aging Aircraft, Ogden, Utah, July 8-10, 1997.
5. F. Jin & F. P. Chiang, "Time-averaged Digital Specklegraphy (TADS) for NDE of Crevice Corrosion and Composite Debond", Proc. of SEM VIII International Congress on Experimental Mechanics, June 10-13, 1996, Nashville, Tennessee, pp.236-237.
6. F. Jin & F. P. Chiang, "NDE of Corrosion by Fractal Geometry", *Research in NDE*, Vol. 7, No. 4 (1996), pp.229-238.
7. F. Jin and F. P. Chiang, "Nondestructive Test of Crevice Corrosion by Time-averaged Digital Specklegraphy (TADS)," Proc. of 1996 ASNT Spring Conference, March 19-22, 1996, Norfolk, Virginia.
8. F. Jin & F. P. Chiang, "NDE of Crevice Corrosion Using Electronic Speckle Pattern Interferometry and Digital Speckle Correlation", Proc. of ASME Winter Annual Meeting, Sym. on Structural Integrity in Aging Aircraft, Nov. 12-17, 1995.
9. F. Jin and F. P. Chiang, "A Noncontact Nondestructive Inspection Technique of Pitting, Stress-corrosion Cracking & Crevice Corrosion Using Digital Speckle Correlation", Proc. CORROSION 95, The NACE Int. Annual Conference & Corrosion Show, Orlando, FL. Mar 26-31, 1995, pp535-1 to 535-10.
10. F. Jin and F. P. Chiang, "Detection of Crevice Corrosion Using Electronic Speckle Pattern Interferometry", Proc. CORROSION 95, The NACE Int. Annual Conference and Corrosion Show, Orlando, FL. Mar 26 - 31, 1995, pp. 534-1 to 534-10.
11. Du, M. L. and Chiang, F.P., (1998) The Effect of Static Tensile Strain on Cumulative Fatigue Damage, *International Journal of Fatigue*. (coming issue, in press)
12. Du, M.L., Chiang, F.P., Kagwade, S.V. and Clayton, C.R., (1997) Influence of Corrosion on the Fatigue Properties of Aluminum Alloy Al 7075, *Journal of Testing and Evaluation*. (May 1998 issue).
13. Du, M.L., Chiang, F.P., Kagwade, S.V. and Clayton, C.R., (1998) Interaction between Corrosion and Fatigue of Al 2024-T3 Alloy, *International Journal of Fatigue*. (Accepted).
14. Chiang, Fu-Pen, Du, M.L. and Li, S., (1995) Early Stages of Fatigue Damage of Fastener Holes Monitored by Laser Speckle. *Structural Integrity of Fasteners*, ASTM STP 1236, pp.143-154.

15. Du, M.L. and Chiang, F.P., (1997) Investigation of fatigue Crack Propagation Using Moire Method, Abstract Proceedings of the SEM Spring Conference on Experimental Mechanics, pp.224.
16. Du, M.L., Chiang, F.P., Kagwade, S.V. and Clayton, C.R., (1996) Interaction between Corrosion and Fatigue of Aluminum Alloy, VIII International Congress on Experimental and Applied Mechanics, Nashville, Tennessee, pp.427-428.
17. Kagwade, S.V., Clayton, C.R., Du, M.L. and Chiang, F.P., (1996) The Effect of Acetone on The Corrosion Characteristics of Al 2024-T3 in a Mist of 0.5M NaCl, 190th Meeting of the Electrochemical Society , Oct. 6-11, San Antonio, Texas.
18. Kagwade, S.V., Clayton, C.R., Du, M. L. and Chiang, F.P., (1995) A Surface and Optical Study of The Influence of Stress on The Corrosion of Aluminum Alloys. Corrosion 95. Orlando, Florida, Paper No. 533, pp.533/2-9.
19. Du, M.L., Chiang, F.P., Kagwade, S.V. and Clayton, C.R.,(1995)Effect of Corrosion on The Subsequent Fatigue Properties of Aluminum Alloy Sheet. 1995 SEM's Spring Conference. Grand Rapids, Michigan.
20. Du, M.L. ,Chiang, F.P., Kagwade, S.V. and Clayton, C.R.,(1995) Investigation of Environmental Fatigue of Al 2024-T3 Alloy. ASME Winter Annual Meeting, San Francisco, California.
21. Kagwade, S.V., Clayton, C.R., Du, M.L., and Chiang, F.P., (1997) The Effect of Acetone on the Corrosion Characteristics of AA 2024-T3 in a Mist of 0.5M NaCl at 24°C, Submitted to Electrochemical Society (ECS), Rapid Communications, 1997.

Appendix 2 List of Personnel Participated in the Project

Fu-Pen Chiang
Principal Investigator
Leading Professor and Chair
Dept. of Mechanical Engineering

Clive Clayton
Professor of Materials Science & Engineering
Director of SPIR (Strategic Partnership for Industrial Resurgence)
College of Engineering & Applied Science

Peison Huang
Assistant Professor
Dept. of Mechanical Engineering

Feng Jin & Ming Liang Du
Graduate Students
Dept. of Mechanical Engineering

Sanjay Kagawade
Graduate Student
Dept. of Materials Science and Engineering

Si Yi Wu
Visiting Scholar
Dept. of Mechanical Engineering